IMPRIMATUR POUR LA THÈSE

High Strain Rate Deformation, Slip Systems and Textures as a Function of Deformation Temperature in a B2 FeAl Alloy

de M. Pingshun Zhao

UNIVERSITÉ DE NEUCHÂTEL

FACULTÉ DES SCIENCES

La Faculté des sciences de l'Université de Neuchâtel sur le rapport des membres du jury,

Mme M. Morris et MM. D. Morris (directeur de thèse), G.Sauthoff (Düsseldorf) et B. Ilschner (EPF Lausanne)

autorise l'impression de la présente thèse.

Neuchâtel, le 1er septembre 1998

Le doyen:

F. Stoeckli

To My Family and My Friends

Preamble

Introduction and literature review

Contents

1. Preamble

Such well known advantages of iron aluminides as their excellent oxidation resistance, extremely high sulphidation resistance and carburization resistance, reasonable high temperature strength, high electrical resistivity, low cost, low density as well as reduced consumption of strategic elements etc. have made them increasingly attractive both in industrial production and in research for many years.

Close attention has been paid to the stress anomaly which appears at intermediate temperatures during deformation for both Fe_3Al and FeAl type alloys and the slip systems below and above the stress peak temperature have been extensively studied by various means such as slip trace observation, deformation texture examination and simulation as well as dislocation analysis by TEM. Identical conclusions have been reached to the deformation systems below the stress peak temperatures for both Fe_3Al and FeAl alloys by all the previous studies, indicating that the dominant slip systems are <111>{011} and <111>{112}. However, different results of deformation system at high temperatures (above stress peak temperature) were noted for the two types of alloys. Some studies confirmed that the slip direction at high temperature is still <111> while the others showed the <100> slip for Fe_3Al and FeAl. Recent studies on the deformation systems of FeAl alloy by slip trace and dislocation analysis (realised usually at relatively low or low strain rate) strongly supported the <100> slip system at high temperature, while some other investigations by deformation texture simulation and texture determination realised at high strain rate and by TEM examination concluded that the deformation of Fe_3Al at high temperatures is controlled by <111> slip system. Thus it is of great significance to shed light upon the deformation system of FeAl alloy at high temperature at high strain rate realised, for example, by forging which is widely used in industrial production to deform ingots into different product shapes and to break down the cast microstructures.

The present study focuses on the determination of slip system in FeAl during high strain rate deformation over a wide range of temperature by various means. The deformation at high strain rate ($\dot{\varepsilon} = 1\ s^{-1}$) was carried out by forging from 400 to 1000°C. True strain-true stress curves were obtained and work hardening rate at different forging temperatures was calculated to correlate the slip system and the mechanical behaviour. Microstructures were observed and the grain size and recrystallized proportion after deformation at various temperatures were evaluated using optical microscopy and SEM. The forging textures were investigated using X-ray diffraction and were evaluated by relative intensity of different reflections. A large quantity of dislocations was analysed by TEM with a view to the determination of Burgers vector, dislocation line direction, glide plane as well as Schmid factor. The statistical analysis of different types of dislocations was performed to make clear the slip system <uvw>{hkl}, dislocation activation and dislocation interactions during

deformation at various temperatures. The orientation of a large number of deformed sub-grains and recrystallized grains was examined by Kikuchi patterns and such orientation was correlated to the texture determination by x-ray diffraction.

Dynamic recrystallization took place at high temperatures after large strain forging and the variation of relative intensity of different reflections as a function of recrystallization fraction obtained at different forging temperatures confirmed that the ideal deformation textures at 400 to 1000°C are {111} caused by <111> slip system at low temperature and by <100> slip system at high temperature, as supported by the previous deformation texture simulation, while the ideal recrystallization textures are {200} type. The results of dislocation analysis showed <111> dislocation dominance at low and intermediate temperatures and <100> dislocation dominance at high temperatures, which are very well consistent with the deformation texture determination. The higher work hardening rate at low temperature and the lower work hardening rate at high temperatures also supported deformation controlled by complex superdislocations below the stress peak temperature and deformation controlled by simple or perfect dislocations above the stress peak temperature.

2. Introduction and literature review

2.1. Definition of intermetallic

An intermetallic compound is a phase which crystallises with a structure other than those of its components, and two types of intermetallic compounds are differentiated as follows:

(a) Intermetallic phases which possess a homogeneity range are called *Berthollides*. The sub-lattice occupation is not restricted to one atom type, e.g. a point position can be occupied by A as well as by B atoms.

(b) Intermetallic phase without any homogeneity range are called *Daltonides*. Each sub-lattice is occupied by one particular atom type[1].

The ordered intermetallics such as Fe-Al, Ni-Al and Ti-Al, etc. under investigation for their possible use as structural materials belong to berthollides.

2.2. The history of intermetallics

The use of intermetallics can be traced back to about 2500 B.C in Egypt and Britain where people used Cu_3Ag as a coating on bronze. Since then, many intermetallics have been employed for various purposes, for example, coin materials such as CuZn at the age of Rome, $Cu_{31}Sn_8$ for mirrors in China in the year zero, dental restorative materials such as Ag_2Hg_3+Sn_6Hg in China and Cu_4Hg_3 in Germany, $(Cu,Mn)_3Al$ as knife material in Germany in 1910, as well as magnetic materials such as Ni-Al-Fe-Co, $Fe_3(Si,Al)$, $SmCo_5$, superconductors such as Nb_3Sn, electric resistance materials such as Fe-Cr-Al, $MoSi_2$, etc.[2]. The scientific research of intermetallics began near the end of the last century with the development of physical metallurgy. It is in this century that intermetallics began to be widely used, primarily for applications as functional materials—magnetic materials, superconductors and shape memory alloys[3].

The lack of ductility and the difficulty of formability have made it difficult for intermetallics to be used as structural materials in the past. However, great attention has been paid to intermetallics as potential structural materials since the turn of the century. Extensive studies have been made, especially for the development of ordered intermetallics based on aluminides of transition metals such as nickel, iron, titanium, niobium and cobalt[4, 5]. One of the first hopes for applications of structural intermetallics was titanium aluminide Ti_3Al, with major research efforts starting in the 1970s. Extensive research on nickel aluminides such as Ni_3Al and NiAl have also been carried out since the 1980s and major hopes for success of commercial applications as structural materials have arisen because of the improvement of ductility by alloying, especially by additions of small amounts of B. Iron aluminides have attracted a great attention for a long time because of some of their outstanding advantages as structural materials, such as excellent oxidation and sulphidation resistances, reasonable high temperature strength, low cost and reduced consumption of strategic elements[4, 6-9]. Various applications of Fe-Al based alloys have been examined for a long time and both fundamental research as well as product development have a very good future.

2.3. Characteristics of Fe-Al Intermetallics

2.3.1. Binary phase diagram of Fe-Al system

The binary phase diagram of Fe-Al system is shown in fig. 2-1[10].In the region of 0-20 at.% Al, there is only α bcc phase, in which there is a small loop of γ fcc phase at high temperature. Most attention has been paid to those alloys with the compositions in the 20-50 at.% Al range. Two typical phases were observed in this region—Fe_3Al and FeAl types. Near the Fe_3Al region, the following phase fields are identified: i) a disordered solid solution α; ii) Fe_3Al with an imperfectly ordered B2 structure; iii) ordered Fe_3Al with DO_3 structure; iv) α and DO_3 region, and v) α+B2 area. In the region of about 36-50 at.% Al, the alloys exhibit uniquely the B2 structure from room temperature to about 1200-1300 °C (depending on the Al concentration). For the alloy used for the present study with 41% Al, the B2 structure remains stable until about 1230°C. The addition of a small quantity of the element Cr (e.g. 2 at. %) in the alloy used in the present study) leads to no significant change in the phases present, as confirmed by examining the ternary phase diagrams[11].

Two typical crystal structures B2 and DO_3 which are often found in Fe-Al alloys are shown in fig. 2-2 (a) and (b) respectively[12]. In fig. 2-2 (a), the atom sites have been divided into equal numbers of sublattices labelled I and II. In the state of perfect long range B2 order, all of the sites associated with one sublattice are occupied by either all A atoms or all B atoms, forming an AB

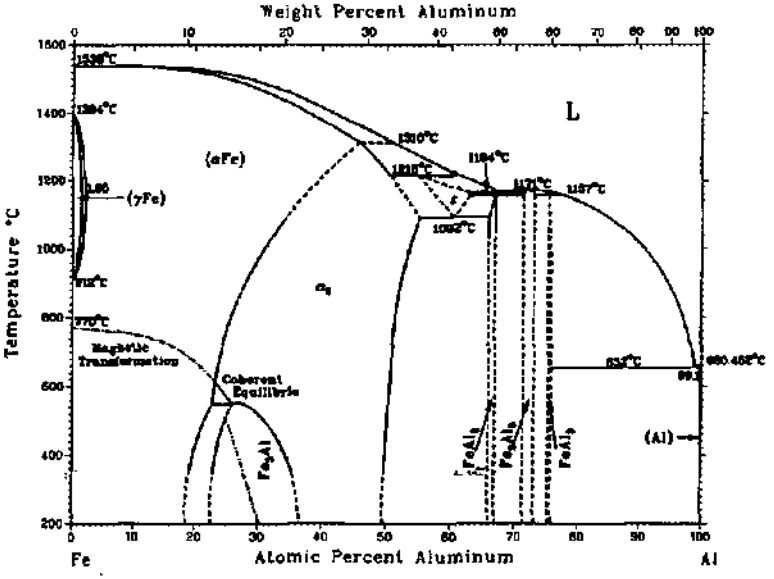

Fig. 2-1 Binary phase diagram of the Fe-Al system

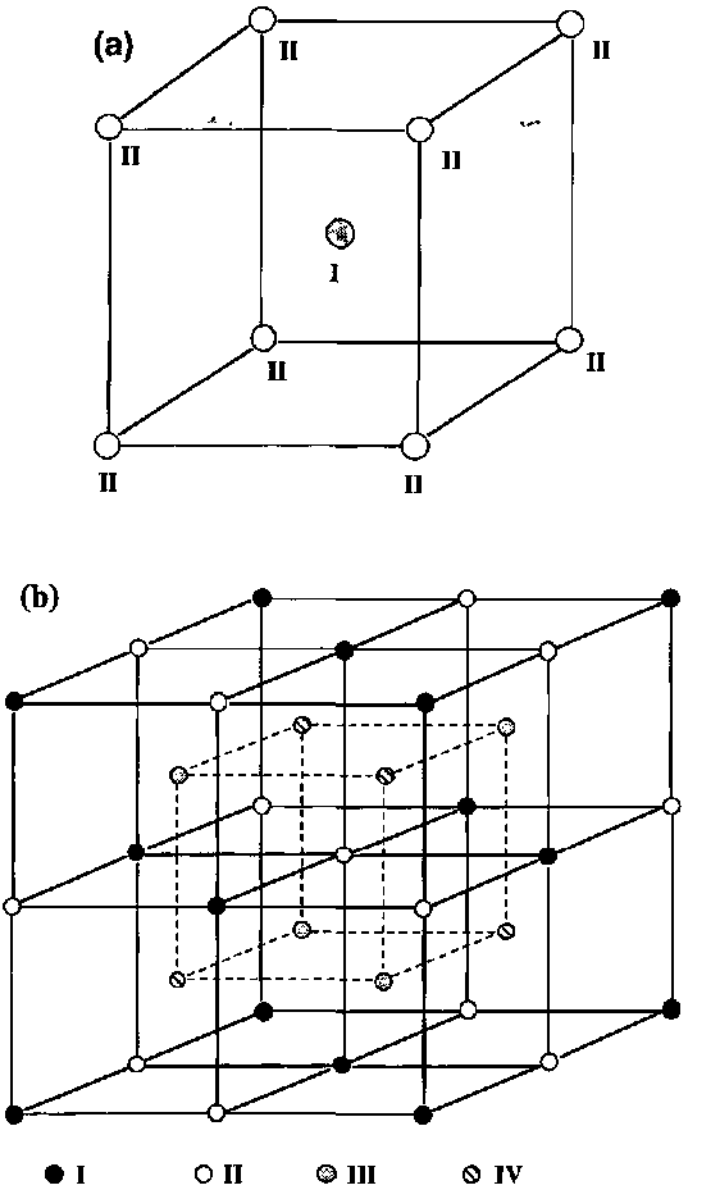

Fig. 2-2 Unit cell of B2 superlattice (a) and unit cell of DO_3 superlattice (b)

compound, specifically an FeAl compound in the Fe-Al system as the chemical composition is appropriate. Therefore, each B atom has for nearest neighbours all A atoms and vice versa. The lattice for DO_3 structure can be subdivided into four interpenetrating face-centred cubic sublattices as shown in fig. 2-2 (b), where the A atoms occupy atom sites on sublattices II, III and IV, while the remaining B atoms occupy type I sublattice sites, forming a A_3B compound, specifically Fe_3Al compound in Fe-Al system at a suitable composition. The transition to B2 order occurs as the site III and site IV become equivalent, that is the Al atoms will sit equally on III and IV sites, together with an equal number of Fe atoms[7], transforming to an FeAl compound.

2.3.2 Some specific aspects of Fe-Al intermetallics as potential structural materials

Close attention has been paid to the fundamental study and industrial application of Iron aluminides since the 1930's due to their outstanding high temperature oxidation resistance, exeellent sulphidation resistance, lower cost and lower density than stainless steels, reasonable strength and reduced consumption of strategic elements.[4, 7, 9, 13].

Studies on the mechanical properties of Fe-Al binary alloy as a function of Al content show that the yield point at room temperature increases as the Al content increases from 5 to 28 at.% and then decreases as Al content increases to 30 at.%, that is the binary alloy exhibits the highest yield strength at 28 at.% Al[14]. Therefore many Fe-28Al based alloys have been investigated. In the range of 30 to 43 at.% Al, the room temperature yield strength increases with the Al content and reaches a maximum at 40 at.% Al and then decreases with Al content[9]. Accordingly, many Fe-40Al based alloys have been studied. Yield strength of FeAl binary alloys remains relatively stable as the temperature increases from room temperature to 600°C but falls to a low value at 700°C. The room temperature ductility falls rapidly as Al content increases from 5 to 10 at.% [14] and reaches a very low value from 10 to 43 at.% Al [9, 14]. Elongation increases with temperature and reaches a high value at 700°C where the yield strength falls. Thus low strength at high temperatures and low ductility (believed to be due to ambient moisture) at low temperatures impeded the applications of Fe-Al alloys although they are intrinsically ductile[15]. Therefore the improvement of high temperature strength and low temperature ductility is extremely important for commercialising of Fe-Al alloys. Consequently, a lot of measures have been taken to resolve these problems.

First of all, the effect of alloying elements on microstructure and mechanical properties has been extensively investigated[16-24]. The alloying elements can be divided into two categories, i) precipitation hardening elements, such as C, B, Zr, Nb, Ta and ii) solid-solution strengthening elements, such as Cr, Ti, Mo, Mn, Si, V, Ni. The addition of these strengthening elements has improved generally both the high temperature and low temperature strength but unfortunately the

low temperature ductility has been deteriorated at the same time. Cr leads to little change of strength but can improve the room temperature ductility[4, 7] as shown in table 2-1[7].

Various heat treatments and thermomechanical processing methods have been conducted to improve the low temperature ductility and the strength[25-33]. These generally act through control of

Table 2-1 Strengthening by Solute Additions(MPa / % addition)

Element	Room temperature effect	High temperature (600°C) effect	Ductility, effect at room temperature
Mo: 1-5%	small	50-200MPa	depresses
Cr: 1-5%	small	50-100MPa	retains
Nb: 1-2%	100MPa	100-200MPa	depresses
Ti: 1-5%	100MPa	50-100MPa	depresses
Si: 1-2%	small	100-200MPa	embrittles

recovery and recrystallization of cold worked structures and it appears that it is the partially recovered/recrystallized state that gives the best properties. These methods have improved the room temperature ductility as well as enhancing the strength. A study of heat treatment on the mechanical properties of a thermomechanically processed Fe-28Al-5Cr based alloy showed both high yield strength and high room temperature elongation and a combination of high yield strength with high elongation (524 MPa with 19%, measured in air) was noted[25]. Such a good combination, however, was rarely seen in other investigations when the elongation was measured in air.

Another important factor determining the microstructure and mechanical properties is the fabrication[5, 8, 34-37]. Many processing methods, such as powder metallurgy[36, 37], reaction synthesis[8], directional solidification[34] have been tested. The investigation and development of these new processing methods have markedly enhanced the properties of Fe-Al alloys.

Significant difference between the oxidation resistance of Fe-Al alloys and that of traditional FeCrNi and FeCrAl alloys is shown in fig. 2-3[13]. The weight gain of Fe-35Al at 800°C for 170 hours is very small while serious oxidation takes place for Fe-25Cr-20Ni and Fe-18Cr-6Al alloys from the beginning of the experiment.

Environmental embrittlement is a specific characteristic of deformation behaviour of iron aluminides. Many studies have been devoted to understanding the nature of the embrittlement and

to propose effective ways of ameliorating the ductility in air[38-43]. The embrittlement in iron aluminides can be explained by the reaction[38, 39, 41]:

$$2Al + 3H_2O \rightarrow Al_2O_3 + 6H \qquad (2\text{-}1)$$

The hydrogen atoms are freed by the reaction between the Al atoms and the moisture in the air and they penetrate into crack tips and cause brittle cleavage crack propagation, possibly as a result of the reduction of cohesive strength across {100} cleavage planes. Fu and Painter have indicated using first-principles quantum-mechanical calculations that the electrons are drawn around the absorbed interstitial hydrogen atoms and bonding between iron and iron atoms is weakened[44].

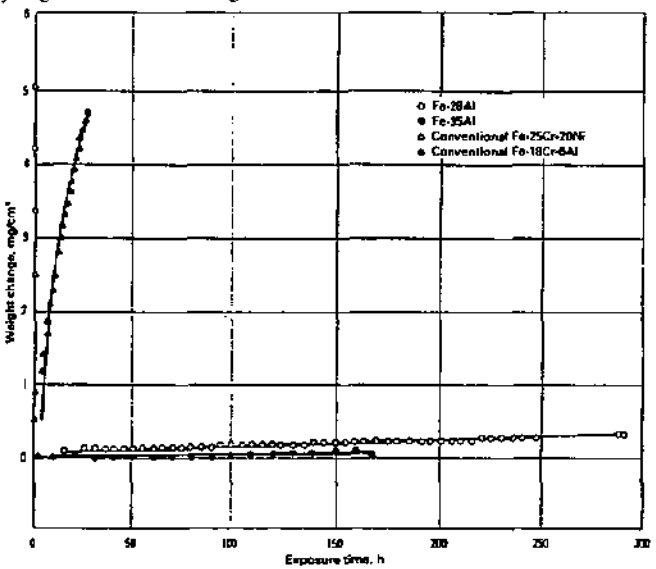

Fig. 2-3 Comparison of oxidation behaviour of iron aluminides with that of conventional iron-base alloys Fe-18Cr-6Al and Fe-25Cr-20Ni

2.4. Site preference of Cr element in the B2 unit cell

The addition of a third alloy element into Fe-Al intermetallics has been examined with a view to improving the mechanical properties, especially high temperature creep resistance, oxidation resistance and room temperature ductility. The site preference of the third alloy element influences the behaviour of dislocations by changing the energies of APBs[45]. The site occupied by the third element can be deduced from an analysis of the peak intensities in x-ray diffraction experiments. The site preference of third element in various intermetallics has been investigated by different methods[45-50]. Schneibel et al have discussed the site preference of Ti, Cr, Mn, Co, Ni, Cu etc.

as third element in Fe-45Al-X alloy (X-third element) assuming that the concentration of Al anti-site defects or vacancies are negligible[46]. The effective Al concentration is:

$$f^*_{Al}=f_{Al}+f_x \cdot p_{x'Al} \qquad (2\text{-}2)$$

where f_{Al} is the atomic fraction of Al (45%), f_x is the atomic fraction of ternary alloying addition X (5%), and $p_{x'Al}$ is the fraction of element X occupying the 'Al' sublattice. The calculated result is shown in table 2-2. $p_{x'Al}$ for Cr element is 74±1.2, which means that the Cr atom prefers to sit on the Al sublattice in the B2 ordered Fe-45Al-X alloy. The above investigations suggest that the Al sublattice is the favourable site for Cr element in FeAl ordered alloy.

Table 2-2 Site occupation parameters in Fe-45Al-5X alloys

X	Fraction $p_{x'Al}$ of element X occupying 'Al' sublattice	Fraction of 'Al' sublattice occupied by Fe (%)	Effective Al concentration, f^*_{Al}
Ti	85.2±2.3	1.5	49.3
Cr	74.0±1.2	2.6	48.7
Mn	26.3±1.1	7.4	46.3
Fe	9.1	10.0	45.0
Co	0.9±1.7	9.9	45.0
Ni	0.6±1.0	9.9	45.0
Cu	-0.3±0.7	10.0	45.0

2.5. Possible slip systems in the B2 ordered FeAl

Fig.2-4 shows the possible slip vectors in B2 structure[51]. Three type of dislocations, namely <100>, <110> and <111> have been observed in B2 alloys, depending on the composition and deformation temperature. Fe-41Al-2Cr exhibits the B2 structure throughout the entire temperature range below the melting point, thus the possible gliding directions for this alloy are those mentioned above. For the B2 ordered structure, <111> super-dislocations dissociate into a/2<111> partials coupled by an APB shown in fig. 2-5[12]. The two partials are retained together by the surface tension of the APB at an equilibrium separation r.

The slip planes for <100> dislocations are principally {001}and {011}, although they can glide theoretically on any {0kl}. <111> dislocations glide mainly on {110} or {112} planes. Since <111> dislocations dissociate into a/2<111> partials as shown in fig. 2-5, cross-slip depends greatly on the APB energy. The separation between two partials is very large when the APB energy is low and thus the partials can cross-slip independently, while for a high APB energy the separation is so small that they can recombine and cross-slip easily. For intermediate values of APB energy, the intermediate partial separations confine the <111> dislocations to their slip planes to a greater or lesser extent.

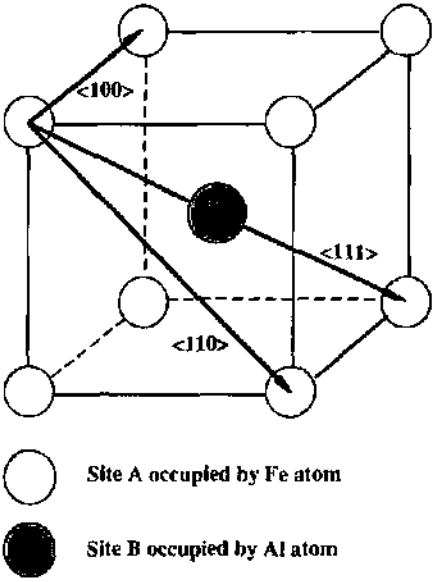

Fig. 2-4 Slip systems in B2 ordered structure

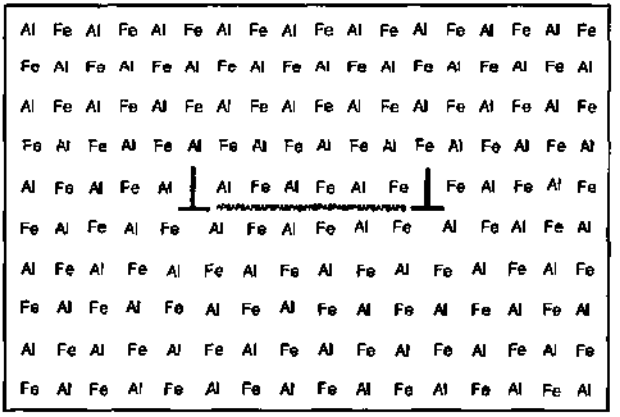

Fig. 2-5 Schematic illustration of two partials of <111> dislocations separated by an APB in B2 ordered material

2.6. Background of the deformation mechanism and texture in Fe-Al based alloys

Both Fe_3Al and FeAl alloys exhibit the stress anomaly: the flow stress decreases with decreasing temperature at low temperatures but increases with increasing temperature at intermediate temperatures and decreases again at high temperatures. Extensive studies have been devoted to such anomalous increase of stress at intermediate temperature and to the deformation systems below and above the stress peak temperature of Fe-Al intermetallics during the last two decades. The nature of the stress anomaly and the slip systems have been investigated by various means such as slip trace observations, deformation texture examination and dislocation analysis. The influence of chemical composition and experimental condition such as deformation temperature, strain rate and crystallographic orientation etc. on mechanical behaviour and the slip systems has been examined.

2.6.1. Description of anomalous stress peak

The positive stress dependence on deformation temperature at intermediate temperature has long been found both in Fe_3Al type alloys [52-56] and in FeAl type alloys[16, 18, 20, 57-67]. A similar stress anomaly is also noted in many other ordered alloys, for example, Ni_3Al, β-brass[68, 69, 70-73]. The stress anomaly is illustrated in fig. 2-6 where the yield stress decreases from room temperature to a certain temperature (stage I), namely 300°C, for FeAl alloys and then increases

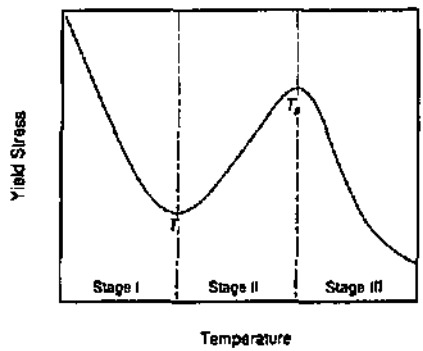

Fig. 2-6 Schematic illustration showing three stages of stress variation as a function of deformation temperature

with increasing the temperature to about 500-600°C (stage II), where the stress peak appears, and finally decreases again (stage III) at higher temperature. However, the shape of such curves obtained by different studies varies greatly depending on the chemical composition of the material tested and the experimental conditions (crystallographic orientation, strain rate, etc.). The discovery of the stress anomaly is of great significance to the material since the strength at intermediate to high temperatures retains a relatively high value as required for some applications. Thus the potential

service temperature of such materials is shifted to a reasonably higher regime. The anomalous stress increase and the presence of the stress peak at about 500–600°C in Fe-Al and other alloys have drawn a great deal of attention to attempting to explain the stress anomaly. Significant efforts have been made to investigate the relationship between mechanical behaviour and deformation systems, dislocation structures, variation of degree of order, as well as vacancy hardening for the purpose of elucidating the nature of the stress anomaly.

2.6.2. Stress anomaly and slip systems in Fe_3Al type alloys

The stress anomaly has been examined in detail at low, at intermediate as well as at high temperatures by many researchers. An early study on high temperature deformation characteristics of Fe_3Al type single crystal was carried out with changes of chemical composition (Fe-24.8Al and Fe-25.8Al) and crystallographic orientation with respect to the compression axis [52]. In the Fe-24.8Al alloy, the yield stresses for various sample orientations increased above 600K and exhibited stress peaks at about 720-770K, below Tc(critical ordering temperature of $D0_3$–B2) depending on the crystal orientation. The stress peaks below Tc temperature were explained in terms of cross slip of <111> dislocations from {110} to {112} planes and the part on the {112} planes acted as a dragging point for the motion of the screw dislocation on {110} planes. On the contrary, the Fe-25.8Al alloy exhibited the stress peaks above Tc temperature instead of below Tc irrespective of the crystal orientation. The lack of stress peak below Tc temperature may be related to the steep decrease of long range order S at Tc since the APB energy in the $D0_3$ structure is the lowest on the {110} planes and the slip system is always the <111> {110} which can be more easily activated than the {112}<111> system below Tc. The stress peak above Tc in Fe-25.8Al alloy was related to the ease of cross slip of B2 superdislocations.

Schröer et al [54] have obtained a similar conclusion by examining the stress anomaly and the ductility of Fe-30Al single crystals with different orientations over a wide temperature range by means of slip trace examination, TEM observation and the strain rate sensitivity upon changing the strain rate. The Schmid factor ratio was used to correlate the extent of cross-slip with the change of the yield stress from room temperature to 900K. For all orientations tested, the yield stress decreased from room temperature to a minimum at intermediate temperature and then increased to the peak value at about 750K and decreased rapidly with further increase of temperature. At the same temperature, the higher the Schmid factor ratio of $m_{(\bar{2}11)[111]}/m_{(\bar{1}01)[111]}$, the higher the stress. This indicates that $(\bar{2}11)[111]$ slip happens when there is higher shear stress on this system and this leads to overall hardening of the crystal. On the other hand, the increase of the stress at higher temperature was well consistent with the decreased $D0_3$ order leading to a decline of the energy barrier for cross slip. The dislocation configuration is a decoupled B2 type dislocation pair both at room temperature and at high temperatures just below stress peak temperature, while it is a double pair $D0_3$ dislocations at temperatures near the minimum of the stress. They believed that

thermal activation plays a critical role for the appearance of the stress anomaly. In a fully ordered lattice, cross slip is impeded by an energy barrier depending on the APB energies of possible primary and cross slip planes and on the interaction energy between the leading and the trailing B2 dislocation pairs. At room temperature, the Peierls stress for the movement of screw dislocations is supposed to be much higher than the stress necessary to overcome the energy barrier for (101) slip, thus the dislocation can easily cross slip and result in the B2-single paired dislocations gliding on the neighbouring parallels slip planes. At intermediate temperatures, the stress necessary for cross slip becomes higher than the flow stress (which is lowered by the thermal activation) and this results in the movement of complete DO_3 superdislocations, leading to the stress minimum. With further increase of temperature, the leading B2 pair is allowed by thermal activation to cross slip from a {110} plane to a {112} plane and thereby decoupled DO_3 dislocations appear once again.

The studies listed above have closely related the stress anomaly to the $DO_3 \rightarrow B2$ transition. This explanation was proved to be less convincing by subsequent studies, where the stress peak was also found at high temperature in a B2 type alloy in which there was no $DO_3 \rightarrow B2$ transition over the entire temperature range, which will be discussed in 2.4.3. Nevertheless the later study by Schröer and co-workers[55] on the plasticity of DO_3 ordered Fe-28Al and Fe-20Al-5Si single crystals showed that the anomalous yield stress of the alloys depends greatly on the crystal orientation and the anomalous dependence of yield stress on temperature is caused by the influence of thermally activated processes on the dislocation mobility rather than by a decrease of the DO_3 long-range order with changing the temperature. This proposition was well explained by the results shown in fig. 2-7, showing the disordering of the two alloys with increase of temperature. The main decrease of long-range order takes place at 790K for Fe-28Al alloy and the stress peak appeared at temperatures 800-850K depending on the crystallographic orientation. Accordingly, the

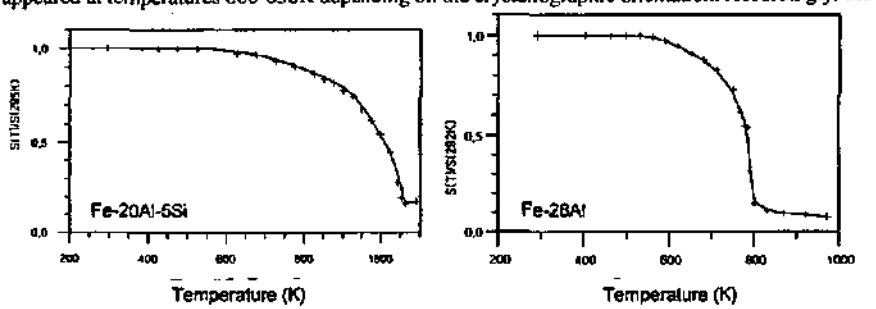

Fig. 2-7 Relative degree of the DO_3 long-range order of Fe-28Al and Fe-20Al-5Si single crystals as a function of temperature

stress peak temperature corresponds to the onset of the decrease in order. In contrast, the onset of the decrease in order of Fe-20Al-5Si (1000K) does not coincide with the stress peak temperature (near 790K).

The preceding studies confirmed one important point that the slip direction below and above the stress peak was always <111>. At low temperatures, the deformation is controlled by four-fold DO_3 superdislocations and at high temperatures the deformation is controlled by B2-paired superdislocations.

A slip trace analysis of an Fe_3Al with DO_3 order deformed in compression from room temperature to 870K by Brinck and co-workers confirmed these same slip directions[74]. The glide planes were {011} at low temperature, where the deformation bands were homogeneous, and also {011} at intermediate temperatures where the deformation bands were inhomogeneous, indicating the occurrence of cross-slip. At the stress peak temperature (820K) three types of glide planes were noted, i.e. {011}, {211} and {312} and frequent cross-slip occurred. Above the peak temperature, homogeneous slip on {211} was seen. Investigations of crystallographic slip in polycrystal Fe_3Al using slip trace measurement and microtexture determination[75] and using texture examination and simulation[76] by Raabe and co-workers indicate that <111> slip is responsible for deformation by warm rolling at 830-860K (near stress peak temperature) to 20% thickness reduction. The <111>{011} and <111>{112} slip systems were identified to correspond to the straight slip traces while the <111>{123} slip systems produced wavy slip traces and <111>{123} slip can probably be explained by combined <111>{011} and <111>{112} slip. According to these texture simulations it is not likely that considerable amounts of slip occur on <100>{001}, <100>{011} or <111>{123} systems during rolling above the $DO_3 \rightarrow B2$ transition temperature.

A detailed study on the deformation texture in Fe_3Al alloy deformed at high temperature (925K-1325K) combined with texture simulation demonstrated that deformation at high temperature is dominated by <111> slip systems[77]. The forging textures simulated based on different slip systems are shown in fig. 2-8. Cube slip on {100} planes resulted in no significant grain rotations and was not responsible for any evolution of textures as shown by the (a), (b) and (c) pole figures. The pole figures (d), (e) and (f) are the computational results based on cube slip on {011} planes, showing a strong {111} deformation texture. Similarly, the simulated forging texture based on <111>{011}+<111>{112} slip systems shown in pole figures (g), (h) and (i) is also characterised by a very strong {111} texture. However, it is very interesting to note that there is a subtle difference between the last two cases. A very strong {111} texture and a nearly zero {110} texture were confirmed in both cases, while the pole figure (g) shows a weak {100} texture caused by <111>{011}+<111>{112} deformation and the pole figure (d) shows no {100} texture at all. This is the major difference between the simulated results based on <100>{011} and <111>{011}+

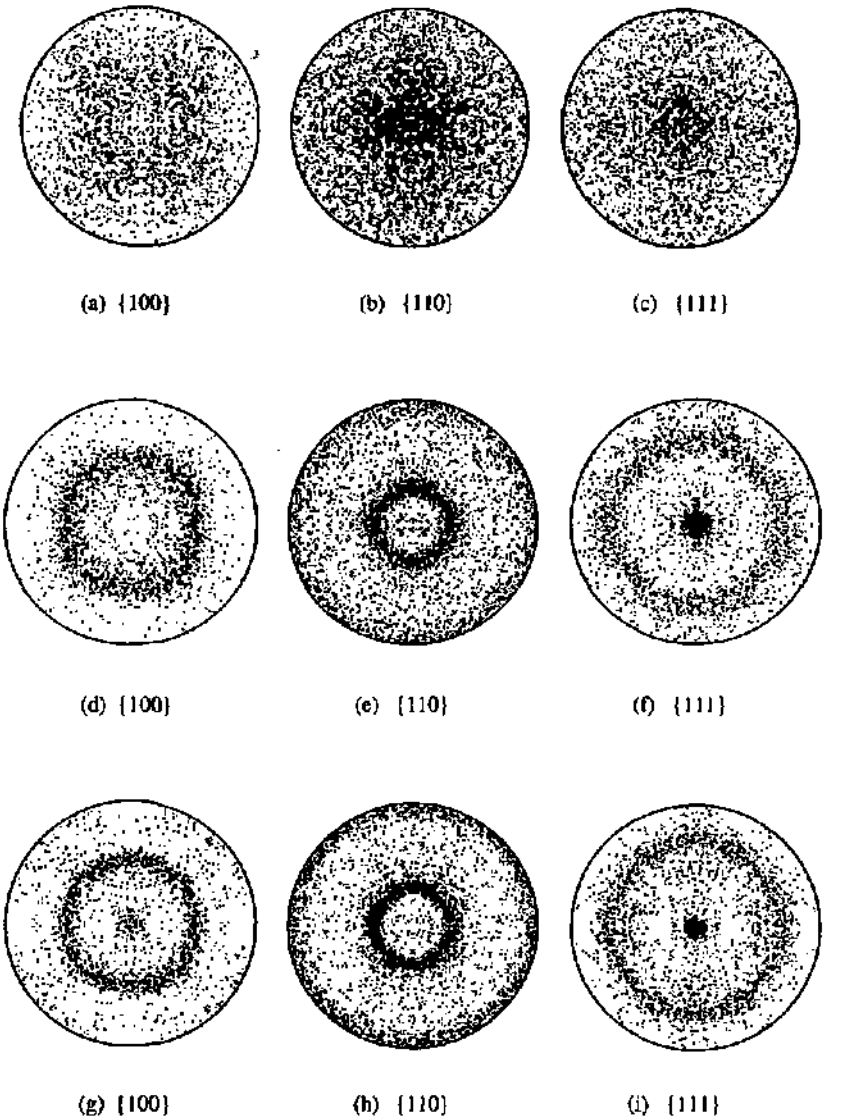

Fig. 2-8 Pole figures showing the forging texture simulations based on slip by the systems <100>{001}-(a), (b) and (c); <100>{011}-(d), (e) and (f); and <111>{011}+<111>{112}-(g), (h) and (i), respectively

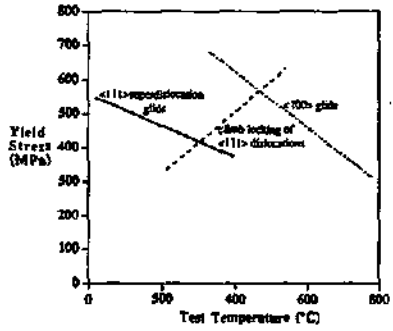

Fig. 2-9 Schematic illustration of flow stress-temperature variation for Fe_3Al alloys and proposed controlling dislocation mechanisms

<111>{112} and such difference will help analysis of the forging textures obtained in the present study. TEM observations of Fe_3Al single crystal deformed at low temperature, namely below stress peak temperature, showed the deformation by DO_3 four-fold <111> superdislocations[78, 79]. The dislocation examination of Fe_3Al polycrystal deformed at 1075K showed also generally <111> dislocations with a limited number of <100> dislocations that were mainly associated with <111> dislocation segment reactions[80]. It was also argued in this work that that the cube dislocations are rapidly exhausted at low strain and at large strain deformations are accomplished by <111> dislocations.

Recent studies of the stress anomaly in Fe_3Al alloy by dislocation analysis have suggested an alternative explanation of the peak anomaly. This study indicates that deformation at low temperature (below the peak temperature) is controlled by <111> slip but at high temperature (above the peak temperature) is controlled by <100> slip[56, 81]. It is confirmed that in the low temperature range, the deformation occurs by the movement of imperfect 1/2<111> dislocations which are dissociated in two 1/4<111> partials separated by an APB and gliding on {011} planes. In the temperature range where the yield stress increases, the <111> dislocations become progressively locked by a local-climb process and the dislocation partials climb out of their glide plane, normal to their Burgers vector. At higher temperatures, dislocations with <100> Burgers vectors are generated and the easy glide of these dislocations leads to the stress drop[56]. Accordingly, a model explaining the positive temperature dependence of the flow stress in Fe_3Al alloy in the intermediate temperature range was proposed and the dislocation mechanisms over the entire temperature range are shown in fig. 2-9[81].

In summary of the slip systems in Fe_3Al alloys discussed above, <111> slip systems are confirmed by all the studies conducted by different means mentioned above at low temperature, namely below stress peak temperature. Nevertheless, the slip systems deduced at high temperature in different works are not consistent and both <111> and <100> slip systems have been proposed.

2.6.3. Slip systems and stress anomaly in FeAl type alloys

Extensive studies have been carried out on the positive temperature dependence of yield stress on deformation temperature in FeAl type alloys and the deformation systems have been investigated by means of slip trace measurement, dislocation analysis as well as deformation texture determination. However, early studies emphasised slip directions and no stress anomaly was remarked[82-85]. TEM examination showed that dislocations in Fe-35Al deformed at room temperature are <111> superdislocations and the APB energy was estimated as being about 0.105 J/m^2 based on the separation of the two partials[82]. Yamagata and Yoshida investigated the slip systems of a FeAl alloy deformed in compression at 77K, 300 and 473K by slip trace observation and the result showed that the slip mode and yield stress were strongly dependent on crystal orientation and deformation temperature. Slip occurred on a $\{111\}\langle\bar{2}11\rangle$ system at low temperature, but at high temperatures $\{111\}\langle\bar{1}01\rangle$ slip became more favourable for orientations with maximum shear stress on the $[111]\langle\bar{2}11\rangle$ or $[111]\langle\bar{1}01\rangle$ systems.

Slip transition from <111> to <100> as a function of deformation orientation and temperature in a near stoichiometric FeAl alloy (Fe-47.2Al) single crystal has been investigated by Umakoshi and Yamaguchi by slip trace analysis and dislocation examination[84]. The deformation of single crystals with various orientations demonstrated that the transition occurred at 670K(=0.44 T_m) and <100> slip was observed around the transition temperature when the crystal was deformed along the <111> direction. This suggested that <100> slip is easier when the crystal orients to the <111> direction. At higher temperature, the range of orientations showing <100> type slip on the surface of deformed samples becomes larger. At even higher temperature(773K), the observed slip planes for <100> slip were found to vary with the orientation of crystal. The region showing <100>{001} slip is about twice as wide as that showing <100>{011} slip. <100> slip in FeAl occurs in fact on one of the $(\bar{1}10)[001]$ and $(001)[010]$ or on both systems simultaneously. Two important features of <100> slip are: i) the slip tends to occur along the [010] direction instead of the most favourable [001] direction; ii) there is a tendency for a {001} type plane to be preferred rather than a {011} type plane as the glide plane for <100> slip. This means that slip on {001}<010> systems is somewhat fundamental to deformation of CsCl structure compounds at high temperature. Slip trace examination and dislocation analysis showed that cross-slip was seen to occur more frequently in crystals deformed by (001)[010] slip than in those deformed by $(\bar{1}10)[001]$ slip. The temperature and orientation dependence of the operative slip direction is shown in fig. 2-10.

The transition of slip directions from <111> to <100> depending on the Al concentration was investigated [85, 86] in a series of FeAl alloys and different results were obtained. Umakoshi and Yamaguchi have investigated the transition temperature as a function of Al content in single crystals having three composition—Fe-42.8, Fe-48.1 and Fe-49.7 and the results showed that a transition in slip direction occurs from <111> at low temperature to <100> at high temperature and the transition temperature decreases with decrease of Al content. In contrast, a study on a series of FeAl alloys with the Al content ranging from 35 at.% to 50 at.% showed that the transition temperature increases with decreasing Al content because the solute atoms interact with the <111> superdislocation elastically and the strength of this interaction is critically dependent on the separation distance between the components of the superdislocations[85]. The smaller the distance, the greater the strength of interaction, giving rise to a thermally activated transition from <111> to <100> slip at a lower temperature. It is well known that the separation distance decreases with increasing the Al content, thus the transition temperature is shifted to lower temperature at higher Al concentration.

A stress anomaly was not noted in the early studies, for example those mentioned above, and this led early researchers to consider that the stress anomaly in Fe_3Al was related to the D03 to B2 disordering transition occurring near 550°C[65]. The studies on FeAl alloys afterwards also showed a positive stress dependence on deformation temperature followed by a stress peak and such a peak was closely related to the transition of slip systems.

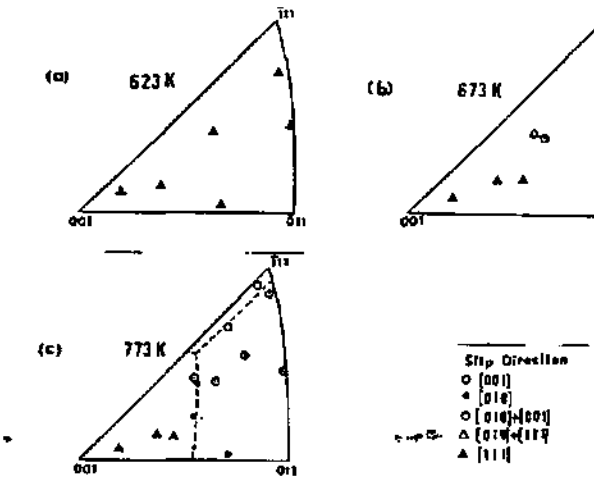

Fig. 2-10 Operative slip directions as a function of deformation temperature and crystallographic orientation

A stress anomaly in Fe-38Al based alloy was noted by Guo and co-workers [58] when deformed at the strain rate of 1.3×10^{-3} s^{-1} and the stress peak was found to occur at 620°C. Dislocation examination demonstrated that at 500°C the dislocations were <111> type and at 620°C most of them were <100> dislocations.

For an alloy with a slightly higher Al concentration (Fe-40Al, large grained alloy), tensile experiments were carried out from room temperature to 900K at $\dot{\varepsilon}=1\times10^{-4}$ s^{-1} in vacuum to investigate deformation characteristics [59]. The stress peak was observed at about 675K(402°C), which is lower than that in the preceding work and is again associated with the transition from <111> to <100> slip.

Klein and Baker have studied the Boron effect on the temperature dependence of the flow and fracture of Fe-45Al alloy[16]. The experiment was carried out in vacuum to avoid any environmental effect on the ductility. The flow stress of Fe-45Al and Fe-45Al-0.05B over the temperature range from room temperature to 1000°C was compared to reveal the difference of behaviour of unalloyed and B doped alloys. The result showed that the addition of 0.05 at.% B raised the peak temperature from 675K to 800K and the yield stress was retained at relatively high levels until 900K by this addition.

Recent studies on B2 Fe-40Al alloys have investigated the stress anomaly and the slip systems in detail by both slip trace analysis and TEM observations[61-64, 87]. The slip directions were identified to be dominantly <111> at low temperatures (below the stress peak temperature) and *<100> at high temperatures by slip trace observation[61, 63]. Stress peak temperatures* were estimated as being between 823 to 873K for most crystal orientations. Some interesting features were noted in the study: i) the slip systems at low temperature were not uniquely <111>, and <100> slip was also observed; ii) below the peak temperature, even as low as room temperature, the yield stress hardly depends on the applied strain rate, indicating that the motion of <111> dislocations has very small strain rate sensitivity in this temperature range. On the other hand, there is a strong strain rate dependence at the peak temperature and above, indicating that the motion of <100> dislocations is strongly rate sensitive; iii) the stress peak temperature corresponds to non-<111> slip systems. Dislocation examination on the same alloy shows that the dislocation structure is characterised by long straight screw dislocations and dislocation dipoles with wavy, irregular shapes and non-screw components at low temperatures. In the temperature regime where the stress begins to increase, <111> dislocations moving on the $(\bar{1}01)$ plane stray to other planes non-conservatively by climbing. Near stress peak temperatures, bundles of tangled [010] dislocations were identified lying along [100] direction. A detailed dislocation analysis of a B2-type Fe-40Al single crystal compressed along a direction near [001] shows that the deformation by <111> superdislocations at low temperature is made more difficult near the stress peak (525°C) as the

dislocations react to produce short, essentially immobile <100> segments and as edge superdislocations decompose to <100> and <110> dislocations, poorly mobile at such temperatures[64]. At temperatures immediately above the stress peak <100> and <110> dislocations move, while at higher temperatures <100> dislocations alone ensure deformation. The thermal activation of glide and the limited possibilities for dislocation pinning through interactions and reactions as deformation occurs by <100> dislocations are responsible for the flow stress fall. The predominance of <100> dislocations at high temperatures was confirmed by an analysis of a large number of dislocations in a B2 ordered Fe-41Al-2Cr alloy deformed at 800°C and 1000°C[87].

Different results of dislocation examination have been noted in a few studies[80, 88]. Feng and Sadananda examined the dislocation configuration in an Fe-47.5Al alloy extruded at 1500K[88]. The <111>{011} dislocations and three types of <100> dislocations–<100>{001}, <100>{011} and zigzagged <100> dislocations helical segments were observed. The emission of <111> dislocations from Fe-Al-Ti precipitates was examined. One possibility of the source of <100> dislocations is the <111> decomposition: a[111]→a[100]+a[010]+a[001]. They proposed that the formation of <100> helical dislocations is due to the excess of vacancies and climb of dislocations at high temperature with also a certain amount of glide. The dislocations with <100> Burgers vector are unlikely to glide on {001} planes because of the necessary splitting of the cores along <111> directions which are out of this slip plane. On the other hand, <100> dislocations can easily glide on {011} planes since the splitting along <111> is in this plane. The splitting is: a[100]→ a/2[111]+a/2[111] which is not favourable on the basis of the b^2 criteria, but should still occur in B2 alloy, at least in the core region, in order to accommodate the atomic displacement and the antiphase boundary energy. The dislocation examination in a recent study on a FeAl type alloy deformed at 925K demonstrates that all the dislocations are <111> type[80].

Many of the slip trace observations and dislocation analyses confirmed that below the stress peak temperature, {112} glide planes of <111> dislocations are preferred at lower temperatures but not so as the temperature increases, where {110} planes are preferred. This is supported by a study on the slip system of a B2 FeAl alloy on the basis of the anisotropic elastic coupling effect of non-glide stresses, showing that the active slip plane in FeAl at low temperature is $\{11\bar{2}\}$ type [89].

In summary of the stress anomaly and slip systems in B2 ordered FeAl alloys, the operation of <111>{110} and <111>{112} slip systems at low temperature has been confirmed by all the studies by both slip trace analysis and dislocation examination. Most studies have confirmed that the slip systems operating at high temperature are <100>{001} and<100>{011}. Such a slip transition correlates with the stress increase and the stress peak. A few investigations, however, have shown <111> with no transition of slip direction at the high temperatures.

In addition, a positive temperature dependence of yield stress was also noted in some other ordered materials such as Ni_3Al, β-brass, etc. and the causes responsible for such stress increase were investigated[60, 68, 69, 90]. A model for the stress anomaly in these alloy was proposed and will be discussed in section 2.6.5.

2.6.4. Influence of strain rate on flow stress of Fe-Al alloys

Stress anomaly, especially the stress peak temperature[91] and magnitude [61, 67], are closely related to the strain rate applied. Li and Baker[67] have investigated the strain rate effect on the yield stress anomaly in Fe-40Al alloy by compression testing carried out at strain rates of 1×10^{-6} s^{-1} to 1×10^{-4} s^{-1} and showed that both the peak temperature and the peak stress were shifted to higher values at higher strain rates. Similar results were also noted in a Fe-39.5Al alloy compressed at strain rate of about 10^{-5} s^{-1} to 10^{-3} s^{-1}. The stress peak temperature rose from 820 to 870K and the peak stress value increased from 275 to 380MPa when the strain rate changed from the low to the high value. On the other hand, a study of the influence of strain rate on the yield stress and stress anomaly in an alloy based on Fe_3Al shows that the stress peak shifted to higher temperatures, while the peak stress magnitude stayed nearly unchanged as the strain rate increases[91].

2.6.5. A review of proposed mechanisms for the stress anomaly

Various mechanisms for the stress anomaly in different alloys were proposed by many researchers and summarised in some review papers[65, 92]. What is essential to these mechanisms is explaining the stress increase before the stress peak followed by the stress fall. Some proposed mechanisms are highlighted as follows:

i) Cross-slip pinning model[72]: <111> superdislocations are supposed to cross-slip from the {110} to the {112} planes and the cross-slipped segments act as dragging points for the motion of the screw dislocations. Since cross-slip is a thermally activated process, the density of such cross-slipped segments presumably increases with increasing temperature, leading then to the stress increase.

ii) Dislocation transition from low to high temperatures[70, 93]: It is believed that the lower strength at low temperature is associated with the easy glide of superdislocations and at high temperatures, associated with easy glide of single dislocations in the disordered state, while at a certain intermediate state, deformation will be difficult. This model can be related to the stress anomaly in Fe_3Al alloy, where four-fold superdislocations exist in the well-ordered DO_3 state at low temperature and 2-partial dislocations in B2 or poorly-ordered DO_3 state at high temperature, and the stress peak is present at temperatures near 550°C where the DO_3 to B2 transition takes place.

iii) Climb locking of superdislocations[54, 81, 94-97]: Stress anomaly in Fe_3Al has been well explained by climb locking of <111> superdislocations[56, 81] proposed initially by Saka and co-workers to explain the stress anomaly in β-brass. At low temperatures, the yield stress decreases with the increase of deformation temperature due to the easy glide of <111> dislocations and the decreasing Peierls force with temperature. In the intermediate temperature range where the yield stress begins to increase climbing of 1/2<111> partials occurs, leading to dislocation segments lying in the climbed sessile configuration. Since the climbing is controlled by diffusion, raising the temperature is expected to accelerate the climbing process, thus more segments lying in climb locking configurations can be expected. This theory is supported by the study on the influence of strain rate on the stress anomaly in Fe-Al alloys, where both the stress anomaly and the stress peak were shifted to higher temperature at high strain rate. Since diffusion is a thermally activated process, climb locking doesn't have enough time to occur at high strain rate and thus a higher temperature is needed for the stress anomaly and stress peak to appear. Above the peak temperatures, <100> perfect dislocations will lead to easy deformation, resulting in a stress fall.

iv) Decomposition of <111> superdislocation to <100> and <011> [59, 61] : This theory is based on the fact that the onset of the stress anomaly corresponds to the appearance of <100> dislocations in Fe-Al alloys, which were thought to result from the decomposition of <111> dislocations. Such resultant <100> and <011> dislocation segments act as pinning points against further <111> slip. The frequency of appearance of these pinning points is assumed to increase with temperature since decomposition becomes more likely at higher temperature, leading to an increase in strength with increasing temperature.

v) Core structure of dislocations[60]: The stress anomaly in some B2 ordered materials was associated with the asymmetric, non-compact core structure of <100> dislocations. It was suggested that the core configuration of the <100> dislocation becomes sessile with the help of temperature and applied stress, and thereby results in the increased flow stress and the orientation anisotropy at intermediate temperatures. However, the stress fall above the stress peak temperature was not explained by this theory.

vi) Vacancy hardening[20, 92]: The basic idea behind this theory, proposed recently by Carleton and corroborated by George and Baker, is that the strength anomaly is observed only in well annealed Fe-Al alloys in which the vacancy concentration is previously minimised by annealing at low temperature for a long time. New thermal vacancies are generated due to the new thermal equilibrium prior to testing the well annealed materials at elevated temperatures and the concentration of these newly generated vacancies is expected to increase with increasing the deformation temperature. Thus the strength in the intermediate temperature range (higher vacancy concentration) is expected to be higher than at low temperature (low vacancy concentration) if the

vacancies are considered to be the pinning points of mobile dislocations, by a solid-solution hardening mechanism. The vacancy hardening proposed recently by George and Baker is

$$\Delta\sigma=[C'_0 \exp(-E_f/kT)]^{1/2} \qquad (2\text{-}3)$$

where $\Delta\sigma$ is the stress increase due to vacancy hardening, C'_0 is the modified pre-exponential factor, E_f is the formation enthalpy of a vacancy. However, some aspects remain that require further examination, e.g. the stress fall at elevated temperature where a high concentration of vacancies is expected[65].

2.7. *Idea, approaches and methods of investigation in the present study*

The results of all the previous studies about the slip systems in both Fe_3Al and FeAl type alloys deformed at low temperatures were consistent, showing <111> slip directions: confirmed by slip trace observation, dislocation analysis, texture examination and deformation texture simulation. However, the inconsistency in the slip systems at high temperatures in Fe_3Al and FeAl was noted in different studies. Particularly for B2 ordered FeAl, <111> slip at low temperature and <100> at high temperature during deformation were confirmed by nearly all the previous literatures except a few recent investigations by texture simulation and dislocation observation, indicating that deformation is controlled by <111> slip at both low and at high temperatures.

The previous studies on the stress anomaly and slip systems in FeAl alloy were conducted using either slip trace examination, or dislocation analysis, or deformation texture deformation together with the measurement of mechanical properties. If a study was carried out using as many methods as possible for a certain alloy, more information could be available and the correlation of the results obtained by different ways would make the results and analysis more convincing.

The intention here is to examine the slip systems operating over the anomalous stress peak in a B2 ordered FeAl alloy by combined studies of microdeformation by dislocation analyses and macrodeformation by texture analysis. Based on the above outline, the following considerations are necessary to ensure more convincing results: i) deformation over a wide temperature range where the presumed stress anomaly takes place; ii) fairly large deformation to ensure the development of deformation textures for the convenience of x-ray diffraction but not too large to render TEM observation excessively difficult; iii) high strain rate is of practical relevance with respect to the commercial fabrication of final products by forging, rolling etc.(these procedures are usually conducted at high strain rate[34]). In addition, the high strain rate enables deformation to be performed in a very short time so that there is little time for recovery or recrystallization (thermally activated process) to modify dislocation structures during deformation; iv) rapid cooling after deformation to retain the deformed microstructure to room temperature, because the rearrangement

of the dislocations takes place very quickly at high temperature[98, 99]; v) measurement of mechanical properties which will be associated with the dislocation process.

In the present study, forging experiments were conducted from 400°C to 1000°C at a strain rate of about $1\ s^{-1}$. The deformation strain was designed to be 45% height reduction to ensure the development of textures at high temperatures, while it was 25% for forging at low temperatures because of the relatively low ductility of the materials at high strain rates. The mechanical behaviour during forging at various temperatures was monitored and the mechanical properties such as yield stress, maximum stress as well as work hardening rate were obtained and were correlated to the deformation mechanisms.

Deformed microstructures were examined by both optical microscopy and SEM to evaluate the extent of recovery and recystallization as well as grain refinement of the materials forged at different temperatures and after heat treatment. Further, the fraction of recrystallized area was correlated to the forging texture obtained by x-ray diffraction examination to distinguish deformation texture and recrystallization texture, and hence, to help explain the deformation systems.

The areas examined by TEM are usually limited to the order of 1μm or less in diameter such that the TEM analysis of only a few areas is only poorly representative of a deformed specimen. Therefore several thin foils were prepared here and numerous fields were analysed for each condition so that the results are more representative. In addition, a large number of dislocations in each field was analysed such that the typical behaviour of this large quantity of dislocations is truly representative of each forged condition. The Schmid factor of each dislocation and slip system was analysed to assess the likely mobility of each type of dislocation and its importance during deformation[63, 100].

Experimental details

3. Experimental details

3.1. Experimental material

The alloy employed in this work had the composition Fe-41Al-2Cr (atomic percent). The material was supplied as a cast and forged pancake about 20mm thick and 10cm in diameter. This alloy exhibits B2 structure over all the temperature range as indicated in the preceding chapter.

The spark discharge method was used to cut the originally forged ingot into small pieces which were then annealed at 1000°C/1h+700°C/1h+600°C/1h+500°C/24h followed by furnace cooling to room temperature in an Argon protected furnace as shown in figure 3-1. This annealing procedure was used to remove any mechanical damage due to cutting or prior deformation, and to ensure the removal of most of the high temperature vacancies.

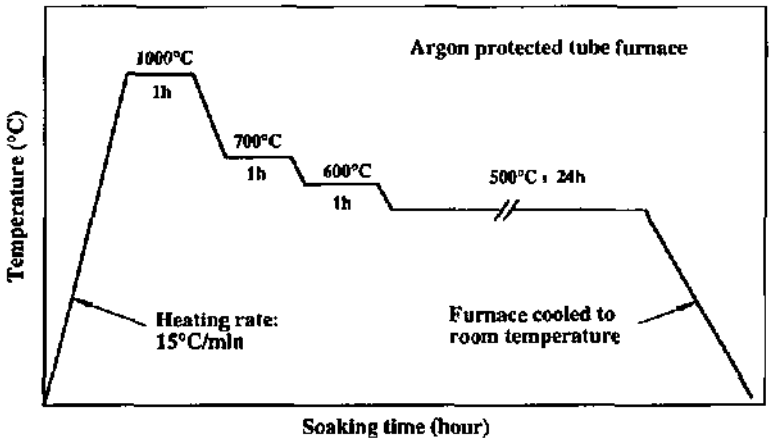

Fig. 3-1 Heat treatment scheme of blanks for forging samples

In this case, the annealed specimen contains very few defects such as dislocations or vacancies. Finally the cylinders were machined to 15mm in height and 10 mm in diameter and the sample ends were mechanically polished flat and perpendicular to the cylinder axis.

3.2. Forging experiments

The following aspects are important for forging experiments: i) deformation carried out over a wide temperature range to examine the role of changing deformation mechanism during this temperature range; ii) sufficient deformation to ensure a well developed forging texture; iii) at lower temperatures, the deformation should not be so large that it will result in cracks during forging; iv) it is necessary to control the loading rate for forging so that the strain rate is the same for forging at

the various temperatures (at elevated temperature, the deformation resistance is lower than that at lower temperature, and the strain rate is not constant for the forging machine used when the deformation resistance varies greatly); v) the forged samples should be quenched as fast as possible to minimise the effect of recovery and recrystallization on the change of dislocation configuration, thus the microstructure and the dislocations examined are really those present at high temperature.

For the observation of dislocations, a large deformation makes analysis difficult in view of the extremely high dislocation density and it is not possible to distinguish individual dislocations in different photos obtained using various diffraction vectors after tilting. Therefore, a small strain of 5% was performed when forging at 400°C and 500°C.

Based on the above viewpoints, the following forging schedule was designed, as shown in table 3-1.

Table 3-1 Forging schedule and post heat treatment

No	Forging temperature, °C	Deformation %	Cooling condition	Post forging heat treatment
1	400Q-1*	5	rapid quenched	
2	400Q-2	25	rapid quenched	
3	500Q-1	5	rapid quenched	
4	500Q-2	25	rapid quenched	
5	500Q-2+A			annealed
6	600Q	25	rapid quenched	
7	600Q+A			annealed
8	700Q	45	rapid quenched	
9	800Q	45	rapid quenched	
10	800Q+A			annealed
11	900Q-1	25	rapid quenched	
12	900Q-2	45	rapid quenched	
13	900Q-3	70	rapid quenched	
14	900SQ	45	slow quenched	
15	900SQ+A			anoealed
16	1000Q	45	rapid quenched	

* Note: Q-rapid quenched, SQ-slow quenched, A-anneal

As discussed in the preceding chapter, the stress anomaly appears in the temperature range of about 0.4-0.45 T_m for this alloy, say 500-700°C depending on the strain rate, so the forging experiments were carried out at 400°C, 500°C, 600°C, 700°C, 800°C, 900°C and 1000°C to ensure covering the

temperature range of the stress anomaly. It is evident that the ductility decreases with decreasing temperature, such that deformation at 400°C, 500°C and 600°C was limited to 25% at which the samples did not crack after forging and the deformation texture was sufficiently developed. Different deformations (25%, 45% and 75%) were designed for the forging at 900°C to examine the effect of deformation on the final structure and forging textures. A specimen forged at 900°C was held for about 5 seconds before quenching to assess the kinetics of structural changes after deformation and to investigate the effect of this time interval on the change of deformation texture.

The post-forging heat treatment was given to the samples forged at 800°C and 900°C to examine the difference between forged state and annealed state, i.e. the difference between actual deformation texture and recrystallization texture, which is extremely important to help explain the real deformation texture and , hence, the slip system at different temperatures. The annealing parameter is as follows:

800°C / 10min + quenching

realised using an Argon protected vertical tube quenching furnace.

It is important to note that the rapid cooling following forging is of great importance to keep the deformed microstructure unchanged from high temperature to room temperature. For Fe-Al alloys, the recovery and recrystallization take place rapidly at elevated temperatures[98, 99] after deformation if a forged piece is not cooled as quickly as possible, such that it is very difficult to obtain information of the real structure at high temperature. As such the results of texture studies and the analyses of the dislocations may not correspond to the deformed condition. On the other hand, the temperature of the pre-heated forging cylinder decreases when it is taken out of the heating furnace before forging. It is necessary to take measures to limit this temperature fall. For these purposes, a forging system was designed as shown in figure 3-2.

In the present experiments, two blocks A1 and A2 made of WC smeared with solid lubricant were preheated to the forging temperature. The two ends of the forging sample were also smeared with lubricant and then the sample was preheated in another Argon protected tube furnace. The size of these two blocks is so large that the temperature fall in the short time between furnace and the forging press can be neglected. A water tank was prepared close to the lower cross-head of the machine so that the forged piece can be quenched very rapidly after forging.

The process of forging was as follows: The first block A1 was taken out and put onto the lower cross-head of the forging equipment. The preheated specimen, in another furnace, was taken out and was put onto block A1. The steel ring (to control the amount of deformation) was put onto the first block A1 and then the second block A2 was taken out and put quickly over the specimen, followed by the compression of upper cross-head of the forging machine until the designed deformation. As soon as the deformation was finished, the upper-cross head was raised, block 2

was moved away and the forged specimen was quickly quenched in the water tank. The forging and quenching procedure can, on the one hand, reduce friction forces and limit the extent of barreling, while on the other hand, the forged specimen did not lose much heat before forging; in addition the deformed structure at high temperature was maintained to room temperature by the fast quench. It is estimated that the time between the end of forging and quenching was about one second.

The strain rate of forging was evaluated to be about 1 s^{-1} which is much higher than that used for tensile or compression experiments in typical studies investigating deformation mechanisms and mechanical behaviour.

Another important aspect is to examine the mechanical behaviour of the alloy at different temperatures during deformation. Firstly, the collection of mechanical data can demonstrate the stress anomaly, and secondly, it is the only way to show whether there is dynamic recrystallization or not.

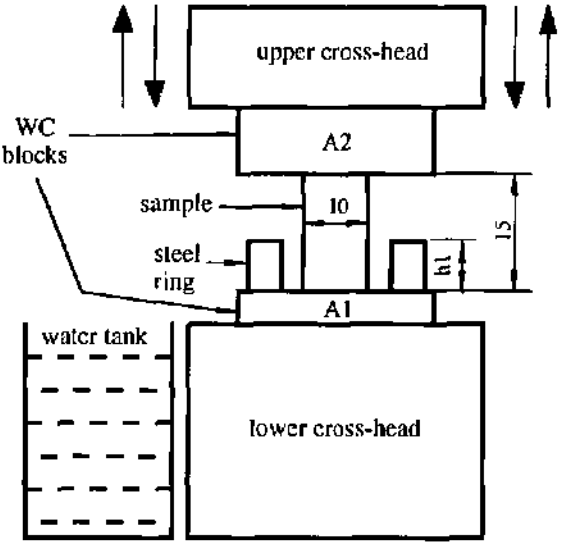

Fig. 3-2 Schematic illustration of forging experiments

The mechanical data collection was conducted using a Lab VIEW data collection system. The force and displacement of forging were transformed into voltage and then recorded by a computer. True

strain-true stress curves were obtained by using various processing soft wares based on the constant volume principle. These curves were fitted to the Hollomon equation:

$$\sigma=k\varepsilon^{n} \qquad (3\text{-}1)$$

where σ and ε are true stress and true strain respectively, k is the work hardening coefficient and n is the work hardening index. This relation was derived based on the principle of uniform deformation stage before necking in the tensile experiment. For compression testing, the equation applies well when the strain is not very large (here, the range 0.05-0.1 true strain was chosen for curve fitting). Thus values of k and n were obtained to characterise the deformation behaviour at various temperatures.

At the same time, the work hardening rate (slope of selected section of deformation curve) was calculated using the method shown in figure 3-3.

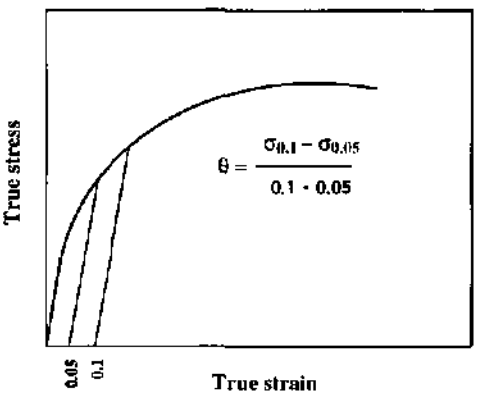

Fig. 3-3 Description of calculation of work hardening rate

Such mechanical data as true strain-true stress relation, work hardening coefficient, work hardening index as well as work hardening rate will be analysed and discussed as characterising the deformation mechanism .

2.3. Optical observation and SEM examination

The specimen for optical microscopy and for SEM was prepared shown as in figure 3-4. The cylinders are slightly barrel shaped after deformation because of friction between the specimen and two blocks in spite of the use of solid lubricant. The deformed specimens were cut mid-way perpendicular to the forging direction. The interior surfaces were employed for microscopy

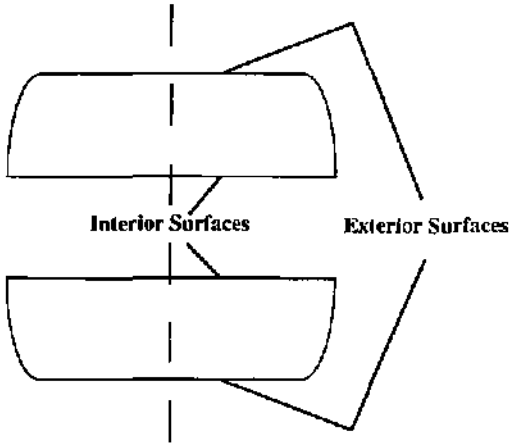

Fig. 3-4 Forged specimen cut midway for OM and SEM observation

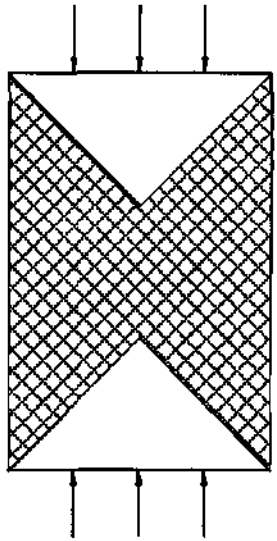

Fig. 3-5 The cylinder showing the deformed (shaded area) and less deformed (open area) regions

observation and X-ray examination because the exterior surfaces were less deformed during forging shown in figure 3-5. Two ends of the cylinder were less deformed while the interior part (cross-hatched part) was deformed uniformly so that this part can represent the real deformed condition.

The interior surfaces were mechanically polished and then etched in a solution of 12ml HCl, 6ml HNO_3, 7 ml HF, 80ml H_2O for optical microscopy. The samples for SEM and X-ray diffraction were mechanically polished followed by electrolytic polishing in a solution: 33% HNO_3, 67% methanol, operated at 5°C, 15V, 4×1s. Optical microscopy was carried out on a POLYVAR instrument equipped with a video on which the analysis of original grain size before forging and the recrystallised grain size as well as the recrystallization fraction were performed for comparison with subsequent SEM observation carried out in a Cambridge Stereoscan 360 instrument in the back-scattered electron mode.

3.4. Texture examination by x-ray diffraction

The x-ray diffraction samples were the same as those used for SEM. Deformation textures experiments were carried out using a Philips MPD 1800 diffractometer operated in the standard $\theta/2\theta$ scanning mode using monochromatic CuKα radiation. The step scanning diffractometer mode was employed instead of the traditional pole figure method since this was not available for use with the large number of samples studied. Scanning parameters such as slit divergence and step time were optimised in order to limit the data fluctuation. Scanning was carried out over a sufficiently wide angular range that the 110, 200 and 211 fundamental reflections, as well as the 111 superlattice reflection, were measured. The fundamental 222 reflection could not be detected because it occures at too high a Bragg angle for the instrument used. In this study, only these four major planes, namely, 110, 111, 200 and 211 were examined.

The specimen was installed in the sample holder, taken out after x-ray diffraction, and then put again in the sample holder and measured for second time. Each forged cylinder was cut to two pieces and both of them were examined twice, thus four groups of data were obtained and finally, the average of these four measurements was used as the diffraction intensity values. Actually, the values of these four measurements were very close to one another.

In order to evaluate the evolution of the textures from the relative intensity of each peak, it is necessary, first of all, to have powder diffraction intensity values, i.e. correponding to the non-textured condition of the material used based on the diffraction intensity calculation[101]:

$$I = |F|^2 \cdot P \cdot \left(\frac{1 + \cos^2 2\theta}{\sin^2 \theta \cdot \cos \theta} \right) \cdot e^{-2M} \qquad (3\text{-}2)$$

where I: diffraction intensity

F: structural factor
P: multiplicity factor
θ: diffraction angle
M: temperature factor.

In this study, the alloy was considered to be in a completely B2 ordered structure. The chemical composition is 57%Fe, 41%Al, 2%Cr (at. %). In B2 structure, two types of the atom sites A and B are occupied by these three kinds of atoms as shown in figure 3-6, based on the discussion of site preference of third element in chapter I:

$$\begin{cases} \text{site A is occupied by Fe atom (50\%Fe)} \\ \text{site B is occupied by Al,Cr,Fe atoms (41\%Al, 2\%Cr, 7\%Fe)} \end{cases}$$

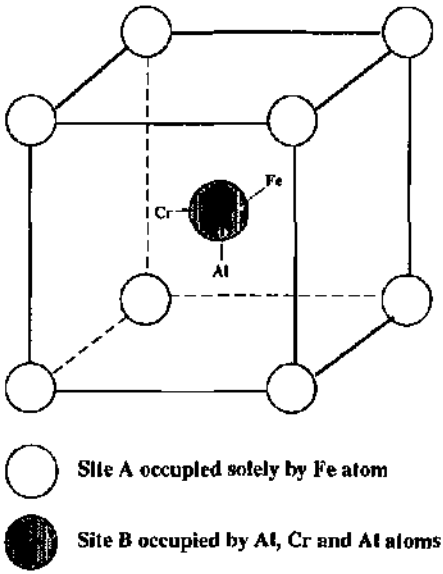

Fig. 3-6 Atom distribution in a B2 unit cell of studied alloy

so the calculations for F in equation 3-2 is as follows:

$F=f_{Fe}-0.82f_{Al}-0.04f_{Cr}-0.14f_{Fe}$ odd numbered plane (111)

$F=f_{Fe}+0.82f_{Al}+0.04f_{Cr}+0.14f_{Fe}$ even numbered plane (110, 200, 211)

The calculated intensities of the major planes are:

Table 3-2 Calculated diffraction intensities of Fe-41Al-2Cr

I_{110}	I_{111}	I_{200}	I_{211}
100	2.25	15.3	30

Compared with the powder diffraction data of AlFe alloy[102]:

Table 3-3 Powder diffraction values of FeAl

I_{110}	I_{111}	I_{200}	I_{211}
100	3	14	25

the calculated intensities of these four major planes of Fe-41Al-2Cr alloy change very slightly compared with that of FeAl standard data (due to the composition difference). The calculated results were taken as the reference of powder diffraction data or standard data, for the present alloy, that is to say, the calculated results represent the polycrystalline diffraction results when each plane has the same probability to diffract , in other words, the fraction of area of each plane on the examined surface is the same. Thus the values calculated based on the atom distribution in the B2 unit cell shown in figure 3-6 will be used as the reference of randomly distributed polycrystalline.

In deformed samples of the studied alloy, textures are developed and consequently the diffraction intensities of these planes change with respect to the standard values shown in table 3-2. For this purpose, the relative intensity $f_{\{hkl\}}$ was proposed to evaluate deformed textures:

$$f_{\{hkl\}} = \frac{I'\{hkl\}/I\{hkl\}}{\sum I'\{hkl\}/I\{hkl\}} \qquad (3\text{-}3)$$

where $I_{\{hkl\}}$ is standard diffraction intensities of {hkl} planes as shown in table 3-2, while $I'_{\{hkl\}}$ is the diffraction intensity of {hkl} planes in a given forged specimen. Dividing this ratio by the sum of all the relative intensity ratios (the $\sum$ term) ensures that textures are described as the proportion of each plane present. For example, the observed diffraction intensities of 110, 111, 200 and 211 after forging at 1000°C are as follows:

I_{110}	I_{111}	I_{200}	I_{211}
100	14	24	51

then, the relative intensity of 111 diffraction after forging can be expressed as:

$$f_{\{111\}}=\frac{I'_{\{111\}}/I_{\{111\}}}{I'_{\{100\}}/I_{\{110\}}+I'_{\{111\}}/I_{\{111\}}+I'_{\{200\}}/I_{\{200\}}+I'_{\{221\}}/I_{\{221\}}}$$

$$=\frac{14/2.25}{100/100+14/2.25+24/15.3+51/30}=0.6 \qquad (3\text{-}4)$$

$f_{\{110\}}$, $f_{\{200\}}$ and $f_{\{211\}}$ can be obtained in the same way and the values are 0.1, 0.15 and 0.16 respectively. In fact, the sum of $f_{\{111\}}+f_{\{110\}}+f_{\{200\}}+f_{\{211\}}= 1$. The meaning of relative intensity $f_{\{hkl\}}$ is the fraction of {hkl} plane on the surface of scanned sample, here, the sample forged at 1000°C, $f_{\{110\}}$, $f_{\{111\}}$, $f_{\{200\}}$and $f_{\{211\}}$ are 10, 60, 15 and 16 respectively when they are expressed as percentage as will be done in the following chapter. Here, an important point to note is that only {110} {111}, {200} and {211} were studied while the other planes e.g. {100}, {210} etc. were not taken into account for the comparison of these reflections. This method provided quantitative information about the proportion of each type of plane to be found in the few degrees around the forged cylinder axis. Thus, the texture of annealed sample before forging and of the samples forged at various temperatures will be evaluated by this relative intensity $f_{\{hkl\}}$.

3.5. TEM observation and dislocation analysis

3.5.1. Thin foil preparation

Small cylinders, 3 mm in diameter were obtained by spark erosion using a AGIE ELOX MONDO 1 equipment and the thin slices were cut perpendicular to the forging axis by a diamond blade as shown in figure 3-7 .

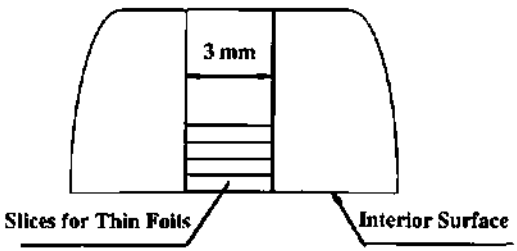

Fig. 3-7 Slices for thin foils preparation

The small slices have not been ground mechanically in order to avoid deformation introduced dislocations during grinding but directly twin jet polished using a twin-jet equipment operated at -10°C, 9V, 175mA, with a solution of 33% HNO_3 and 67% methanol For each deformed cylinder, numerous thin foils were prepared so that different areas in various grains with different characteristics (crystalline orientation, variety of dislocations, crystallised or non-crystallised

grains, etc.) in these thin foils were examined, thus, reasonably good statistical data on dislocation analysis were obtained.

3.5.2. Analysis of dislocations

TEM examination and dislocation analysis were carried out using a Philips CM200 instrument operated at 200kV equipped with a double-tilt system which allowed tilting over ±45° and ±60° about two orthogonal axes, thus it was possible to examine several major zone axes for a given area investigated, ensuring that several independent imaging g vectors were used and stereographic analysis was carried out over a wide angular range, so the direction of dislocation line and consequently the glide plane of the dislocation were determined. Bright field and weak beam photos were taken for the analysis of Burgers vector, line direction, glide planes as well as Schmid factor of dislocation. The Burgers vector was determined based on the principle of invisibility and according to $\mathbf{g}\cdot\mathbf{b}=0$ or $\mathbf{g}\cdot\mathbf{b}\neq 0$ when the diffraction vector changes [103] and the glide plane was determined from the dislocation direction and the Burgers vector. In fact, there exist residual contrast for <100> dislocations even when $\mathbf{g}\cdot\mathbf{h}=0$ due to strong $\mathbf{g}\cdot\mathbf{b}\wedge\mathbf{U}\neq 0$ or due to anisotropic elasticity effects[64]. The determination of glide plane was not possible when straight screw dislocations were examined.

3.5.3. Orientation of analysed grain (subgrain) and Schmid factor of dislocation with respect to compression axis

The orientation of analysed grain was determined using diffraction pattens and Kikuchi lines. Diffraction pattens were identified when the double tilt angles A and B were near zero and then slight tilting was performed in order to place the Kikuchi lines corresponding to the given zone axis symmetrically about the transmission spot and the angles of double tilt A and B recorded. The diffraction patterns (zones) observed were usually (111), (001), (110), (112), (212), (331) and occasionally (515) and the double tilt angles A and B were small (typically below 3°). Thus these zone axes were considered to be the forging axis of the observed area. As soon as the Burgers vector, glide plane and orientation of analysed grain (subgrain) were determined, the Schmid factor of each dislocation was calculated based on[103]:

$$m=\cos\alpha\cdot\cos\beta=\frac{u_1u_2+v_1v_2+w_1w_2}{\sqrt{u_1^2+v_1^2+w_1^2}\sqrt{u_2^2+v_2^2+w_2^2}}\cdot\frac{u_1h+v_1k+w_1l}{\sqrt{u_1^2+v_1^2+w_1^2}\sqrt{h^2+k^2+l^2}} \qquad (3\text{-}5)$$

where α: the angle between the orientation of analysed grain and the Burgers vector

β: the angle between the orientation of analysed grain and the normal of glide plane

$[u_1\ v_1\ w_1]$: orientation of analysed grain

$[u_2\ v_2\ w_2]$: index of Burgers vector

$(h\ k\ l)$: index of glide plane

A high value of Schmid factor m indicates that the combination of Burgers vector, glide plane and crystalline orientation is favourable to the movement of the dislocation in the given condition while a low m is not favourable to glide. In the present study, the $m \leq 0.15$ are considered low Schmid factor, the $m=0.15$-0.32 are considered intermediate Schmid factor and the $m \geq 0.33$ are considered high Schmid factor (the cube slip on {001} planes has a value of Schmid factor $m=0.33$ when the crystallographic orientation of analysed grain or deformed subgrain is near [111] direction). Statistical analysis of three types of dislocations <100>, <110> and <111> was conducted to determine their relative frequency, mobility according to the m value, and the glide plane, in order to examine the dominant slip systems.

In the present investigation, a large number of dislocations was analysed for 400°C, 500°C, 800°C and 1000°C forged samples, in reference to previous studies which suggested that the transition temperature of Burgers from <100> to <111> is about 500-600°C. For each forged sample, several thin foils were prepared and examined by TEM and for each thin foil, different areas were studied. Thus, for each forging condition, a large number of dislocations in different thin foils and at different areas with grains or subgrains in various orientations was analysed, ensuring that a good description of the deformed state was obtained.

Experimental results

4. Experimental results

The experimental results of the present work include: i) mechanical behaviour at high strain rate, large deformation and at various forging temperatures; ii) global microstructural examination; iii) deformation texture and recrystallization texture and vi) dislocation analysis.

4.1. Mechanical behaviour during forging

The true stress-true strain curves were obtained based on

$$\varepsilon=\ln(1+e) \qquad (4\text{-}1)$$

where ε is the true strain and e is the engineering strain.

At the same time, average strain rate was calculated based on:

$$\dot{\varepsilon}=2v/(h_i+h_f) \qquad (4\text{-}2)$$

where v is the upper cross-head speed of the forging equipment, h_i and h_f are initial height and final height of the cylinder before and after forging.

The true strain-true stress curves forged at 400°C, 500°C, 600°C, 700°C, 800°C, 900°C and 1000°C are shown in fig. 4-1 – fig. 4-8 respectively. Average strain rate is indicated in these figures. The strain rate was well controlled to be 1 s^{-1} except that for forging at 900°C (25% reduction in height) and at 1000°C because of lower deformation resistance (fig. 4-6, fig. 4-8) and that for forging at 900°C (70% in height reduction) in fig. 4-7 for both the lower deformation resistance and larger strain, hence, smaller h_f (final height of deformed cylinder) indicated in equation 4-2.

These figures show a typical polycrystalline strain-stress response, while the forms change as a function of deformation temperature. The true strain-true stress curve obtained from forging at 400°C (fig. 4-1) shows a low yield stress (here the stress was measured at 0.2% plastic strain) but a very high maximum strength and a very large work hardening section in which the true stress *spans from about 260MPa to about 1500MPa in the range of true strain 0.002-0.33*. The deformation behaviour at 500°C (fig. 4-2) is similar to that of 400°C but it exhibits a lower maximum stress and a slightly higher yield point, besides, the work hardening section is reduced to a scope of 300-1200 MPa in true stress and 0.002-0.21 in true strain. For the strain-stress curve obtained by forging at 600°C shown in fig. 4-3, an obvious change compared with that of forging at 400° and 500°C is the increase of $\sigma_{0.2}$, which is about 450 MPa, and at the same time, the maximum strength also decreases to about 995 MPa and the work hardening range is narrowed to 0.002-0.21 in true strain. The true strain-true stress curve for the forging at 700°C is similar to that of forging at 600°C, but the maximum strength reduced to 726MPa at 0.21 in true strain as shown in fig. 4-4.

The distinct changes in true strain-true stress curve were noted in the forging experiments at 800°C and at 900°C for both 25% and 75% deformations shown in fig. 4-5–4-7 respectively. The

important feature of these three figures is the increased yield stresses, low maximum stresses, and narrowed work hardening ranges (0.002-0.17 in true strain for 800°C forging, 0.002-0.13 in true strain for 900°C forging) and in true stress ranges (556-620MPa for 800°C forging, 550-570MPa for 900°C forging). The slope of the hardening stage is rather low. Another pronounced feature of these three curves is the evident softening phenomenon after maximum strength, suggesting recovery and recrystallization at such a high deformation temperature and large strain. This is especially true in fig. 4-7, where large deformation of 75% (about 1.4 in true strain) resulted in dynamic recovery and dynamic recrystallization followed by a drop of stress.

True strain-true stress curve of forging at 1000°C (fig. 4-8) was obtained using only a X-Y recorder to measure force and displacement and true stress and true strain calculated manually based on the constant volume principle and the Hollomon equation $\sigma=k\varepsilon^n$ (the Lab View system failed to collect force-displacement data during this forging). The present curve can represent the deformation behaviour at 1000°C forging and it is characterised by a low yield point (below about 320 MPa) and again a narrowed work hardening range (0.002-0.14 in true strain, 325-368MPa in true stress). For this test, the imprecisions inherent in the X-Y recording system mean that the elastic strain region and the yield stress value are not well defined. Both the yield point and the maximum stress are much lower than that of the materials forged at 800°C and 900°C. An evident drop of true stress after maximum stress indicates also dynamic recovery and dynamic recrystallization at such a high temperature.

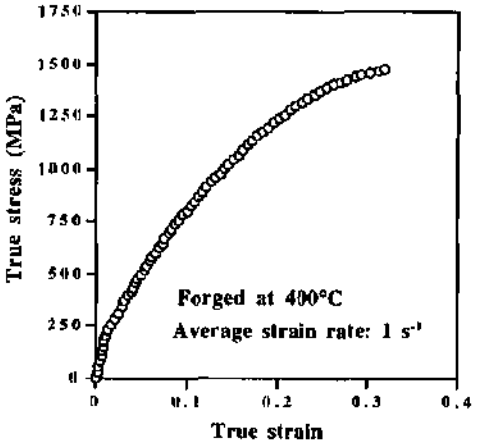

Fig. 4-1 True strain-true stress curve of forging at 400°C showing a low yield point, a high maximum stress and a large range of work hardening

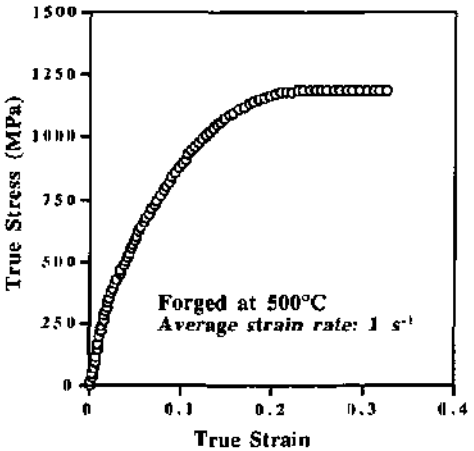

Fig. 4 -2 True strain-true stress curve of forging at 500°C showing a low yield point, a high maximum stress and a large range of work hardening

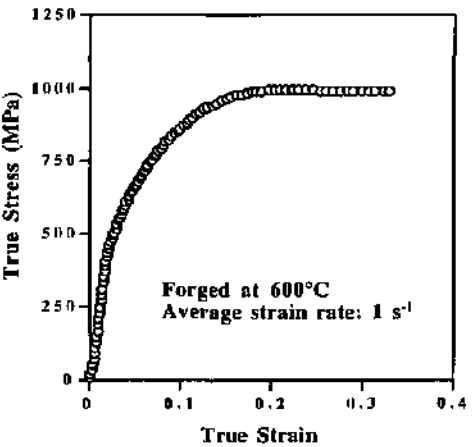

Fig. 4-3 True strain-true stress curve of forging at 600°C showing an increased yield point, lower maximum stress and an intermediate range of work hardening

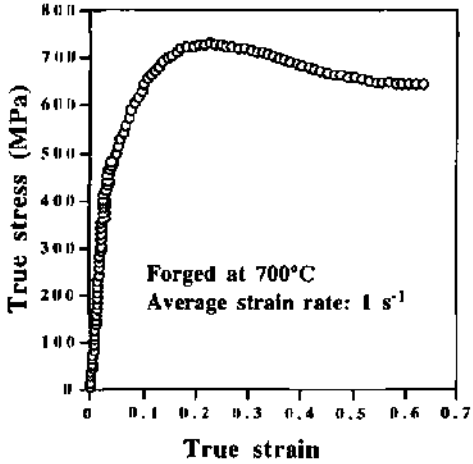

Fig. 4-4 True stress-true strain relation upon forging at 700°C showing higher yield point, lower maximum stress and smaller range of work hardening

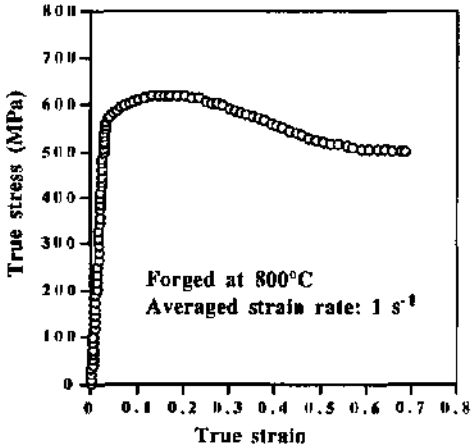

Fig. 4-5 True strain-true stress of 800°C forged material showing a high yield point, a low maximum stress and a small range of work hardening

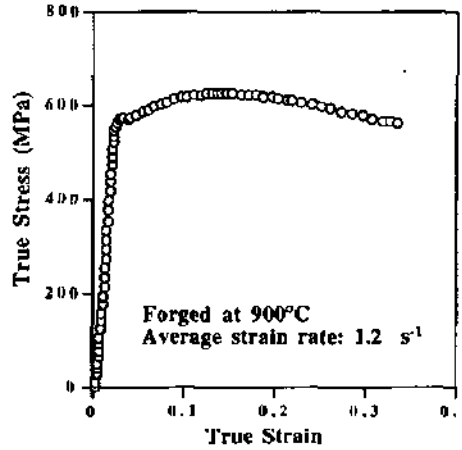

Fig. 4-6 True strain-true stress curve forged at 900°C with the deformation of 25% showing a high yield point, a low maximum stress and a small range of work hardening

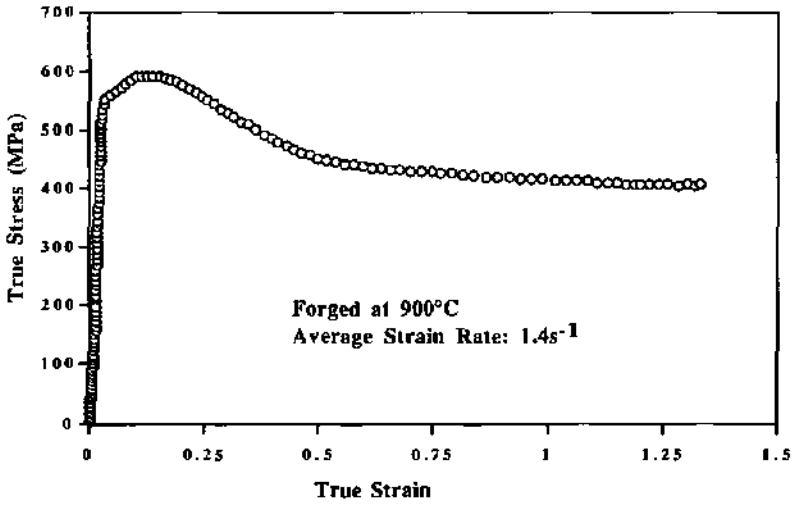

Fig. 4-7 True strain-true stress curve forged at 900°C with the deformation of 75% showing a high yield point, a high maximum stress and a small range of work hardening

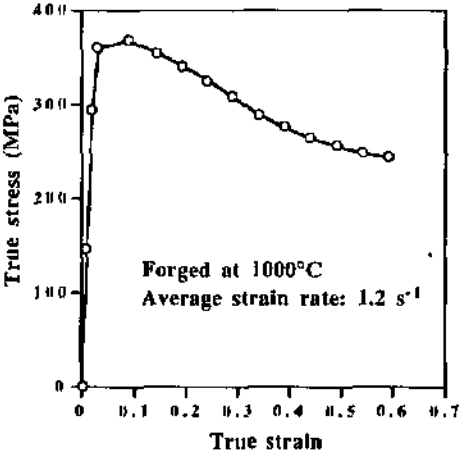

Fig. 4-8 True strain-true stress curve of forging at 1000°C showing a low yield point, a low maximum stress and almost no work hardening

In order to examine the change of flow stress as a function of forging temperature, the yield values and the maximum stress were measured for the curves shown above and listed in table 4-1. A $\sigma_{0.2}$ –temperature curve was drawn and shown in fig. 4-9 together with a comparison with the compression results obtained at low strain rate (4×10^{-4} s^{-1}, provided by D.G.Morris) for the purpose of examining the effect of strain rate on the flow stress and on the shift of anomalous stress peak temperature. Since forging experiments were very difficult at low temperature for the present alloy at high strain rate due to the poor ductility, the forging data below 400°C were not available and are indicated by a dashed line in the forging results curve.

Table 4-1 Yield stress and ultimate stress at various forging temperatures

Forging temperature (°C)	Yield stress (MPa)	Maximum (MPa)
400	264	1460
500	323	1185
600	428	980
700	445	726
800	556	620
900	524	607
1000	-----	360

A yield stress peak appears in both curves as expected. The compression results at low strain rate show that the flow stress peak occurs at about 500°C with the stress dropping suddenly to a low value equivalent to that at room temperature when the temperature rises to 550°C. In addition, the flow stress at 400°C is comparable to that of 550°C. It is clear that the stress peak is confined in a narrow temperature range, namely, 100°C. Forging results show some different features compared with the compression curve in view of stress peak temperature and the temperature span of this stress peak. High strain rate has shifted the peak stress temperature to about 800°C and the slope of this curve from 400°C to 800°C is more gentle than that of the slow compression curve. The values of the anomalous peak stress are nearly the same for these two case (560MPa for compression at 500°C and 550MPa for forging at 800°C). The peak stress at high strain rate does not exceed that at low strain rate in divergence, to some extent, with the results in the literature.

The dependence of maximum stress on temperature is shown in fig. 4-10, indicating that the maximum stress decreases monotonically with increasing temperature over the whole temperature range.

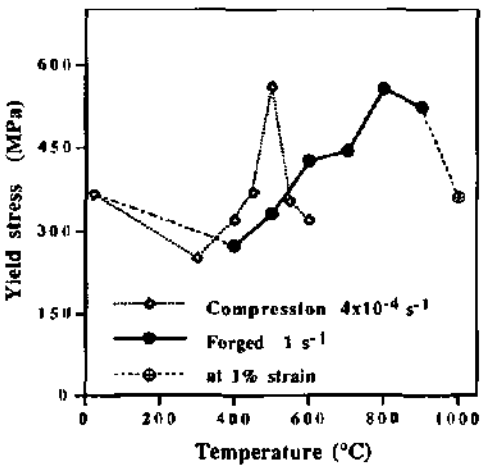

Fig. 4-9 Flow stress as function of deformation temperature at high and at low strain rate (the datum for forging at 1000°C was measured at 1% strain in absence of precise data at 0.2% plastic strain)

Curve fitting to true stress-true strain curve based on $\sigma=k\varepsilon^{n}$ (Hollomon equation) was conducted and the work hardening index and work hardening coefficient were obtained in order to define the work hardening characteristics of forging at various temperatures. At the same time, the work

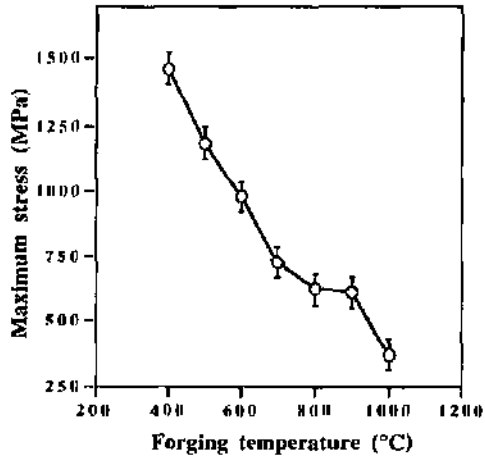

Fig. 4-10 Maximum stress as function of forging temperature

hardening rate was also calculated. An example of such a fitted curve is shown in fig. 4-11. The Hollomon expression fits very well to present true strain-true stress curves as indicated by r values in the selected strain regime. The n and k obtained by such a regression method are shown in fig. 4-12 as a function of forging temperature. Work hardening rate θ calculated in the range of 0.05-0.1 true strain is shown in fig. 4-13.

It is obvious that n, k and θ have a similar trend with change of forging temperature. They exhibit very high values at 400°C where strong work hardening occurred, where an n value as high as 0.66 was determined and θ reaches 5900 MPa per unit strain. In addition, this work hardening took place over a wide range of strain, see fig. 4-1. At 500°C, these three parameters decrease but not too much and the work hardening range in true strain also diminished. If we consider these work hardening parameters at 600°C, the drop is evident especially the value of k and θ. At temperature as high as 900°C, n, k and also θ fall so much that they are one order lower in magnitude than that of 400°C.

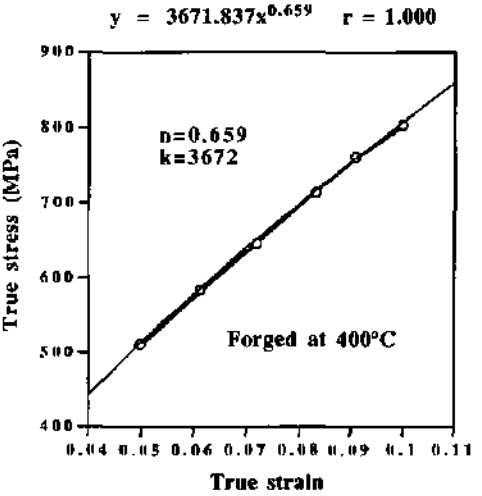

Fig. 4-11 Curve fitting on the basis of $\sigma=k\varepsilon^{n}$ to obtain n and k values for forging at 400°C

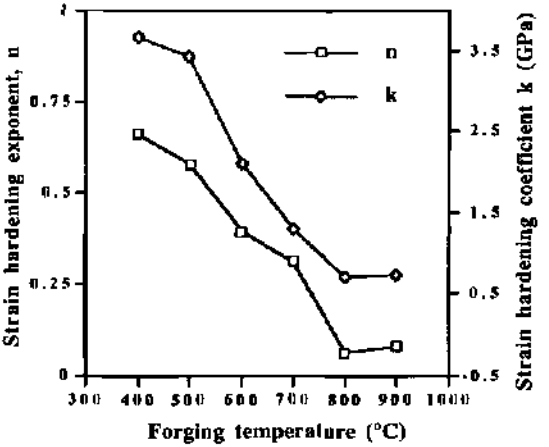

Fig. 4-12 Work hardening index and work hardening coefficient as a function of forging temperature

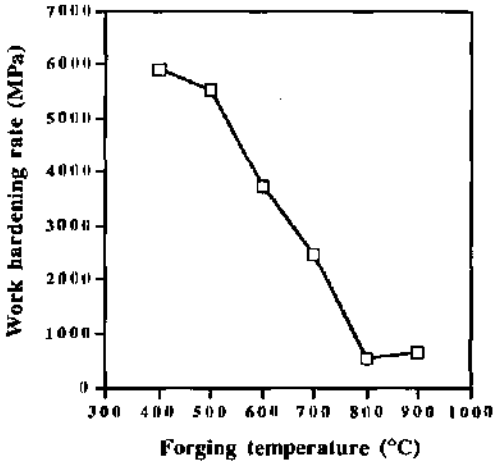

Fig. 4-13 Relationship between work hardening rate (θ) and forging temperature

4.2. Optical observation and SEM examination

In this section, the original state of the material tested was observed and the grain size, deformation structure as well as recrystallization fraction of forged samples and forged+annealed structures of different samples were examined.

The annealed microstructure of initial material before deformation was examined by optical microscopy and is shown in fig. 4-14. Annealing treatment resulted in a single phase, equi-axed and uniform polycrystalline structure with grain size of the order of 0.5-1 mm on which there are many small chemical attack pits.

The deformation structure after forging at 500°C followed by rapid quench is shown in fig. 4-15 (a) and (b). Some cracks were observed, indicating that the material does not exhibit very high ductility upon forging at such a high strain rate and relatively low temperature. Both intergranular and transgranular cracks were seen. The forging axis is normal to the viewing plane, so the microstructures did not appear seriously elongated or pancake shaped. The deformation took place but not uniformly in all the original grains as shown in fig. 4-15 (a). Severe deformation occurred in some grains, for instance, in A and B due to their favourable orientation with respect to the loading axis and a large number of deformation bands are distributed throughout the entire grain. In contrast, other grains were less deformed. The deformation bands in grain B are shown more clearly in fig. 4-15 (b) with a higher magnification. These deformation bands are nearly parallel and uniformly dispersed, which suggests the operation of the same slip systems.

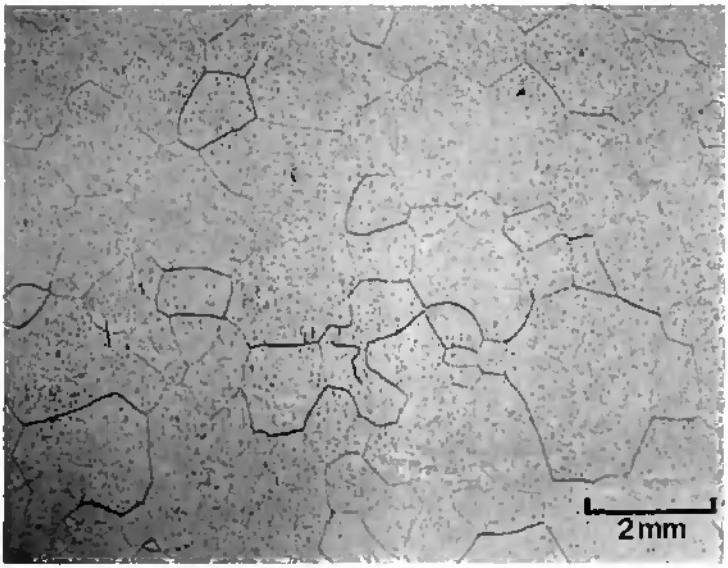

Fig. 4-14 Equi-axed polycrystalline structure of testing material after anneal

Annealed microstructure of forged sample at 500°C is shown in figure 4-16 (a) and (b) for the purpose of investigating the effect of annealing treatment on the evolution of deformed structure. The deformed grains and the deformation bands in these grains shown in fig. 4-16 retain similar features to those of the non annealed condition considering the microstructure in fig. 4-15. In any case, subtle changes can be found if the deformation bands in fig. 4-15 (b) are examined in detail. The boundaries of the bands in fig. 4-16 (b) are zigzagged and not as straight as those in fig. 4-15 (b) and the outer edges are less distinct (as marked by arrows). This indicates that recovery occurred to a certain extent. Furthermore, occasional recrystallized grains with a clear grain boundary were observed, as in fig. 4-16 (b) marked G, situated between two deformation bands. A detailed examination of fig. 4-16 (a) also shows a few recrystallized grains at the lower right corner. The extent of recrystallization is so slight, however, that it can be neglected. In fact, the annealing at 800°C for 10 minutes did not change the deformed microstructure substantially, which is attributed to the relatively low reheating temperature for annealing and to the small amount of deformation.

The deformed microstructures upon forging at 400°C and at 600°C had the same characteristics, being composed of some heavily deformed grains, in which a larger number of deformation bands

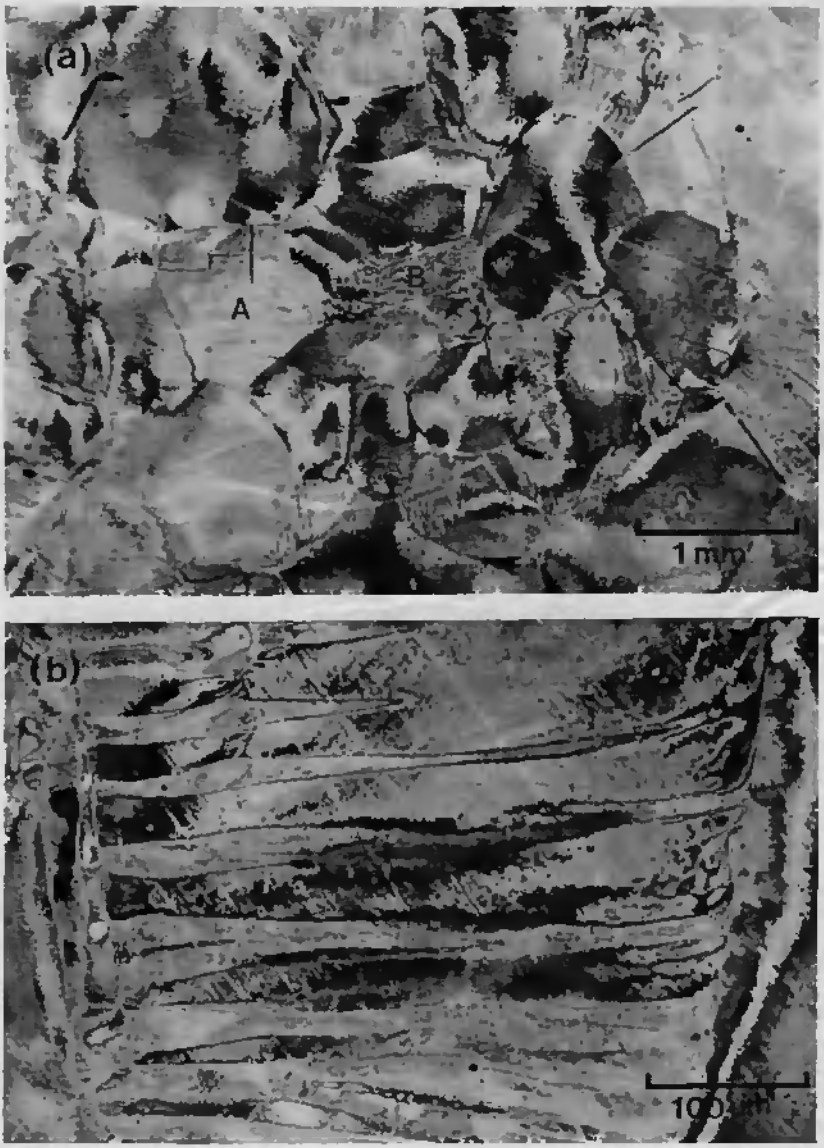

Fig. 4-15 Deformed microstructure upon forging at 500°C

were observed, and some less deformed grains. Annealing at 800°C for 10 minutes did not change the general features of the microstructure except for some subtle changes caused by recovery. The

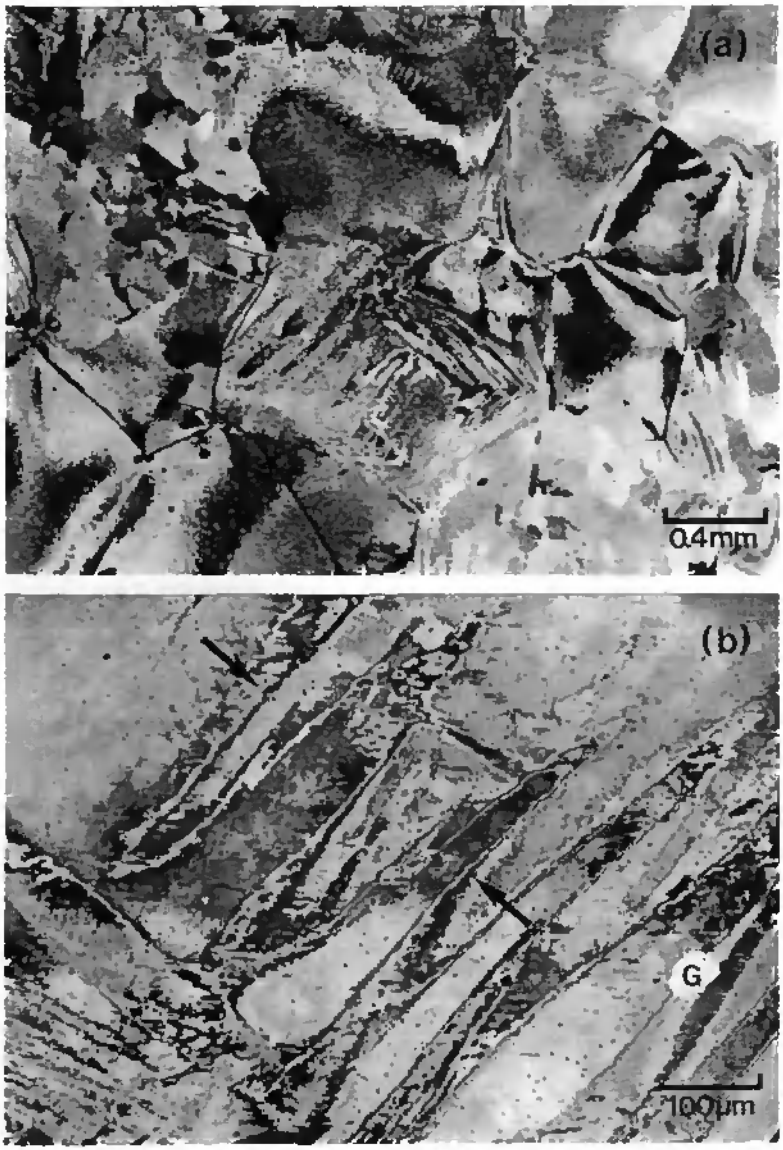

Fig. 4-16 Deformed microstructure of forging at 500°C
followed by anneal at 800°C, 10min

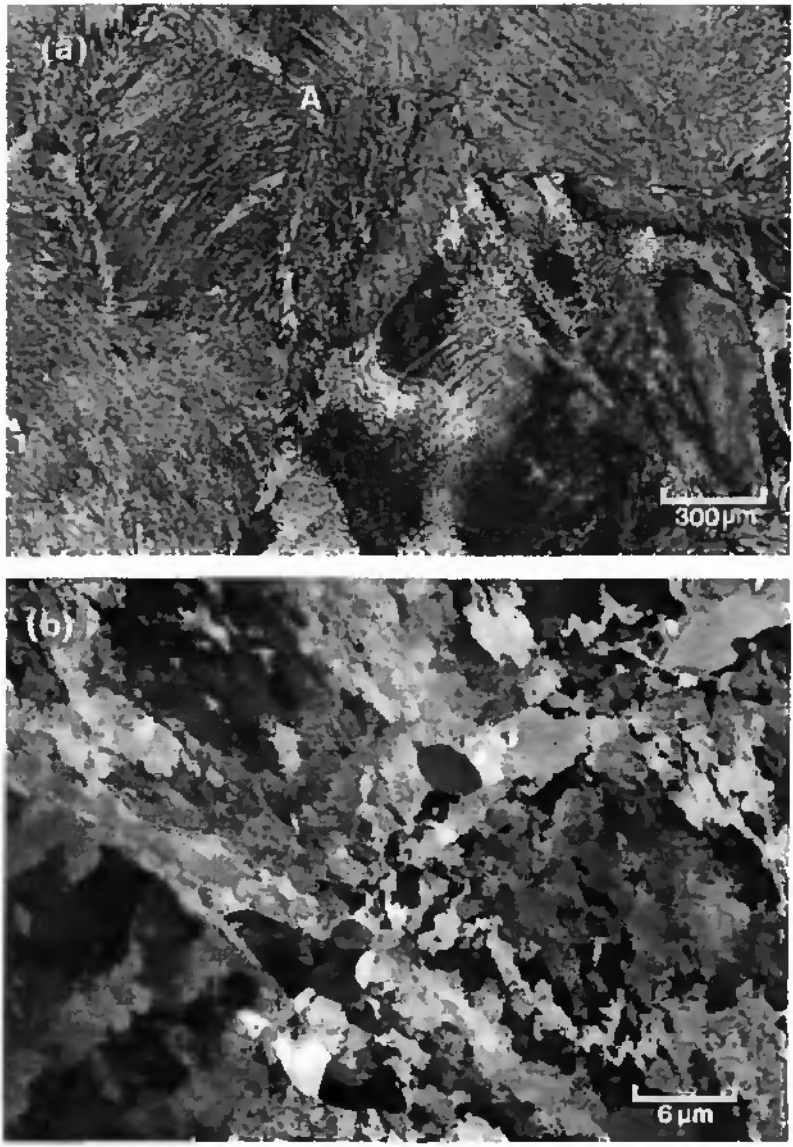

Fig. 4-17 Heavily deformed structure upon forging at 800°C showing elongated subgrains and small amount of equiaxed fine grains

heavily deformed microstructure produced by forging at 800°C (45% height reduction) followed by rapid quenching is shown in fig. 4-17 (a). A large quantity of deformation bands was observed in all the grains. Fig. 4-17 (b),shows in detail the A area (a triple point of three original grain boundaries) in fig. 4-17 (a). The mixed structure of elongated cells or subgrains and fine, equiaxed grains and subgrains several microns in size demonstrate the high deformation and occurrence of recovery as well as recrystallization. The structures varied from place to place due probably to the orientation of original grains. The subgrains or fine equiaxed grains were usually found at regions within initial grains or along the boundaries and triple points of three boundaries.

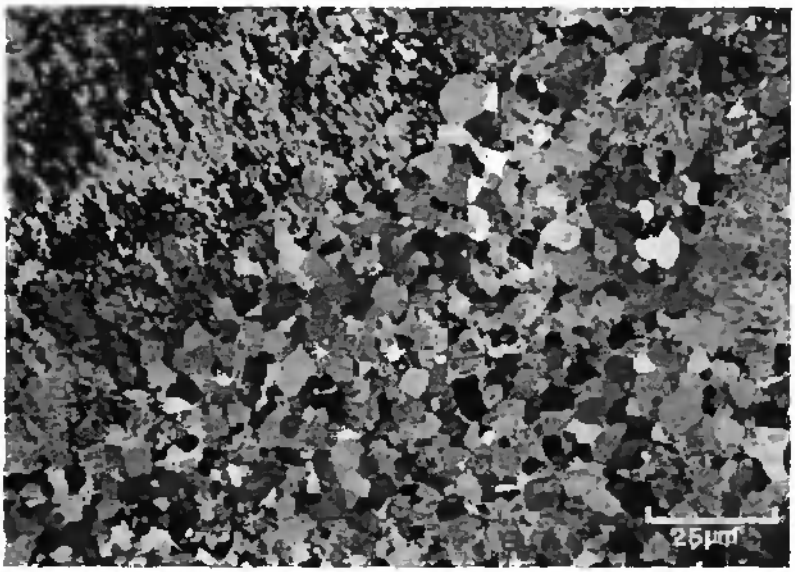

Fig. 4-18 Mixed microstructure of deformed region and equiaxed grains region in the same sample as fig. 4-17

Another area in the same specimen as that of fig. 4-17 was examined and a deformed region at left-upper side and a recrystallized region at right-low side were observed shown in fig. 4-18. In this area, fine, equiaxed grains coexist with the very fine elongated and oriented subgrains. The large fraction of recrystallization suggests that this region is a more heavily deformed original grain. The unrecrystallized subgrains keep the deformed orientation even though recovery occurred while the recrystallized grains have completely different orientations compared to the subgrains as will be discussed in section 4.4.

Several specimens forged at 800°C were examined and the average size and area fraction of equiaxed grains were measured and estimated as being about 5μm and 15% respectively.

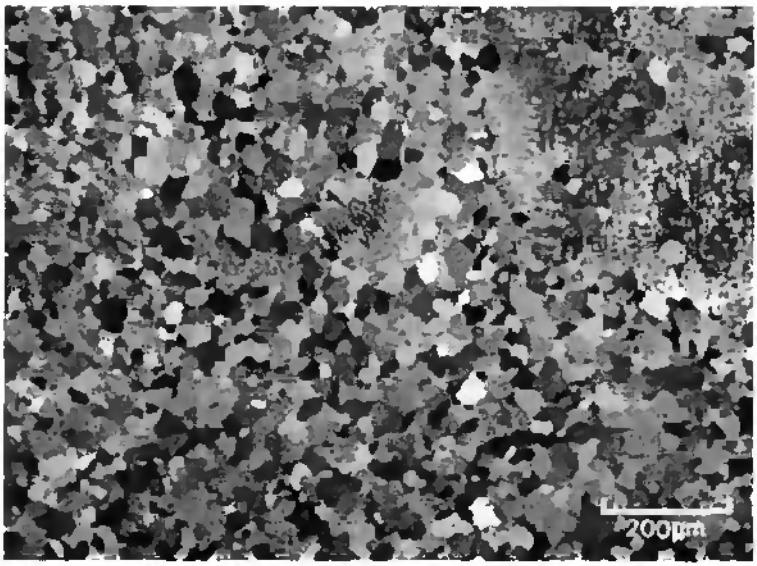

Fig. 4-19 Equiaxed grains of 800°C forged sample followed by anneal

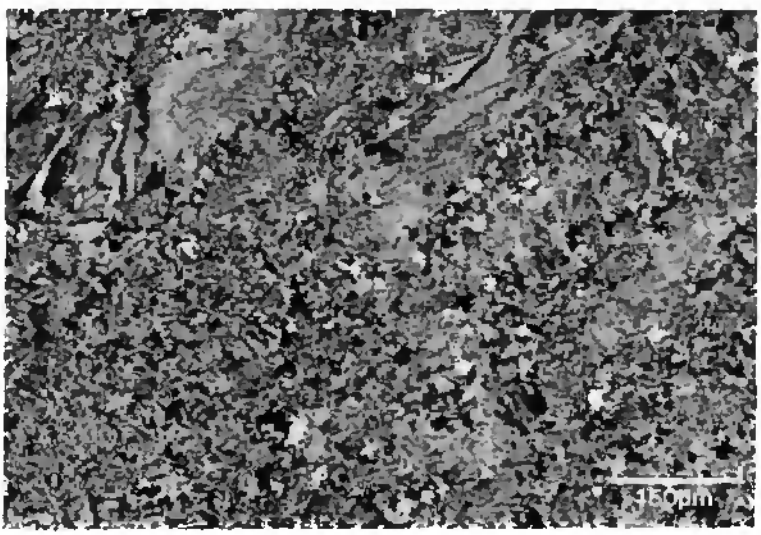

Fig. 4-20 Forged at 900°C and rapid quenched microstructure

The annealed microstructure of the 800°C forged sample is shown in fig. 4-19 and the annealing treatment leads to enormous change from the highly deformed structure. The fraction of equiaxed area was about 90% with grain size about 20μm, which are much larger than the deformed, non-annealed ones in fig. 4-18. At the right-up side is a less deformed initial grain in which deformation bands, subgrains and some equiaxed grains coexist.

The deformed structure upon forging at 900°C (45% deformation) and rapid quenching is shown in fig. 4-20. The higher forging temperature leads to gradually larger amounts of equiaxed recrystallized fraction, with the grain size also being larger. Beside the recrystallized part, recovery happened evidently within the unrecrystallized regions. The grain size and equiaxed fraction in this area were estimated as being 8 μm and 35% respectively.

Fig. 4-21 900°C Forged and slow quenched microstructure
(about 5 seconds after forging before quenching)

In order to consider the effect of delay (after forging before quenching) on the evolution of the highly deformed structure at high temperature, forging at 900°C (45% deformation) and delayed quenching (a 5 second interval before water quenching) was conducted and the final structure is shown in fig. 4-21. Such a short interval resulted in a distinct change compared with that of forged and rapid quenched condition. Recrystallization fraction is as high as 70% and the equiaxed grain size reached about 10μm. In addition, these recrystallized grains are not uniform in size from place

to place, which indicates that such a short time can not make the recrystallized structure homogeneous. Annealing at 800°C for 10 minutes was carried out for the forged at 900°C and slow quenched specimen to investigate the effect of this anneal on the variation of structure shown in fig. 4-21. Such an anneal leads to great change of deformed structure namely a further increment in the recrystallized fraction, to about 90%, and homogeneously sized, larger grains of size 15μm, as shown in fig. 4 -22.

Two specimens were forged at 900°C to 25% and 70% deformation, respectively, followed by rapid quenching in order to examine the influence of deformation on the microstructure after forging. Very limited recrystallization (less than 5%) along the original grain boundaries was noted after forging at 900°C to 25% deformation. Anneal at 800°C for 10 minutes was also applied to such forged sample and the microstructure did not change evidently after annealing, which is similar to the condition of forging at 500°C to 25% deformation with the same anneal, suggesting that the recrystallization caused by such anneal was not significant for the material forged to lower deformation at both 500°C and 900°C. However, such small amount of recrystallization together with the recovery have softened the deformed structure to a certain extent as shown by the flow stress in fig. 4-6.

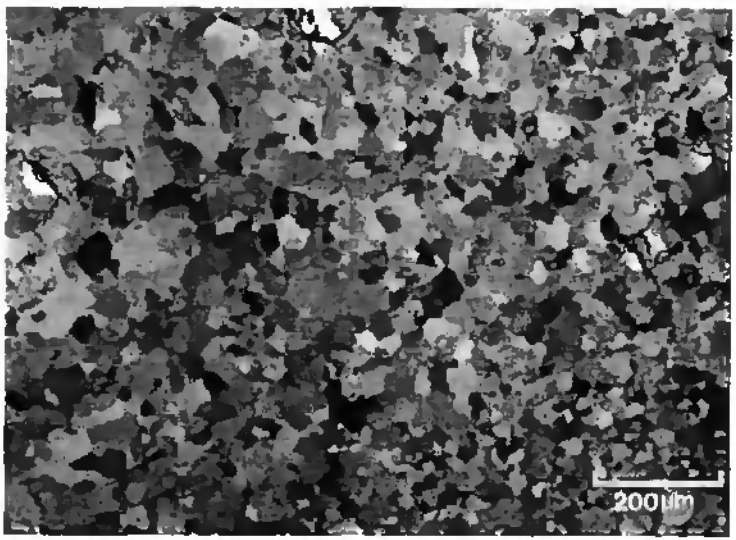

Fig. 4-22 The change of deformed structure forged at 900°C followed by slow quenching upon anneal at 800°C for 10min

The forging to 70% deformation at 900°C followed by rapid quenching caused enormous recrystallization (about 80%), indicating that the higher deformation favours very much the dynamic recrystallization during high strain rate deformation at high temperature, leading to significant softening shown by the drop of the flow stress in fig. 4-7.

The microstructures deformed at 1000°C are similar to that of the sample deformed at 800°C and that of 900°C. The major difference is that the recrystallized grain fraction increased and the recrystallized grain size is larger (about 50% and 15μm respectively).

In summary of the deformed microstructures at various temperatures, both the recrystallized grain size and the recrystallization fraction increase with the increment of forging temperature. The change of recrystallized fraction as well as the grain size as a function of forging temperature and heat treatment is shown in table 4-2 and the data are plotted graphically in fig. 4-23. At lower temperatures and smaller deformation strains (below 600°C and 25% in height reduction), recovery and recrystallization were rarely seen. Larger deformation at higher temperature (forging at 900°C for 75% in height reduction) leads to significant recrystallization . A very short holding time (about 5 seconds) after forging at high temperature (900°C) resulted in a much higher recrystallization fraction than for the rapidly quenched sample. It can be seen that the proportion of recrystallization is even higher than that of the sample forged at 1000°C and the recrystallized grain size is as large as that of the sample forged at 1000°C. 10 minutes anneal at 800°C largely enhanced the extent of recrystallization and the grain growth, and consequently promoted homogenisation of the deformed structure.

Table 4-2 Recrystallized grain size and recrystallized fraction under different forging (45% deformation) and heat treatment conditions

Material state	Recrystallized grain size (μm)	Recrystallized fraction (%)
800Q	5	15
800Q+A	20	90
900Q	8	35
900SQ	12	70
900SQ+A	15	90
1000Q	15	50

Note: Q-rapid quenched, SQ-slow quenched, A-anneal at 800°C for 10 minutes

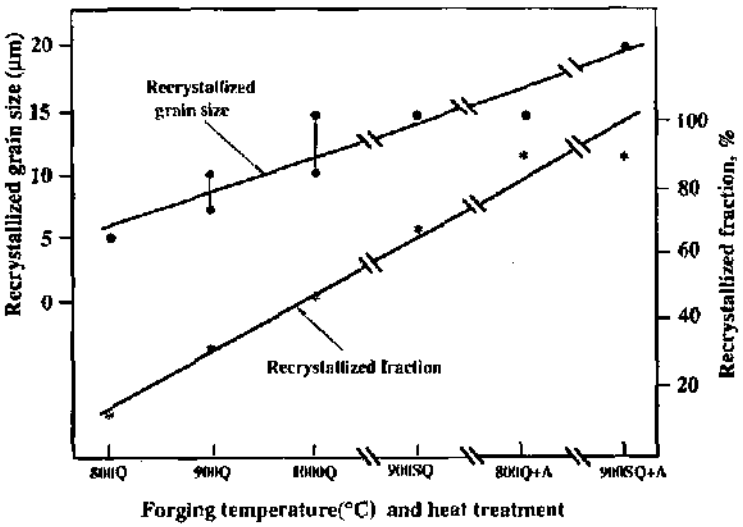

Fig. 4-23 The change of recrystallized fraction and grain size with variation of forging temperature and heat treatment

4.3. Deformation texture and recrystallization texture

The Deformation texture and recrystallization texture will be examined qualitatively based on x-ray spectra and quantitatively based on the relative peak intensities as discussed in chapter 3. X-ray diffraction spectra were obtained on transverse section perpendicular to forging axis, scanning over the angular range (2θ) of 25 to 100° where some major peaks were detected, including some superlattice reflections due to B2 ordered state.

X-ray spectra of several forged and annealed samples will be presented below. A summary of the texture data is provided later in table 4-3 and fig. 4-28. The spectra of annealed sample before forging and the sample forged at 400°C are shown in fig. 4-24 (a) and (b). In fig. 4-24 (a), 110 peak displays a very strong intensity while the other peaks have weak intensities especially that of 111. The relative intensity of 110, 111, 200 as well as 211 reflections were calculated based on the intensity of the peaks using the method described in the preceding chapter, thus representing the percentage of each of these four groups of plane parallel to the surface. Theoretically, they should have the same percentage (25%) but here, they exhibit some difference due to inhomogeneity of structure (texture) caused by the casting, forging and annealing history, thus the relative intensities of these four reflections are not the same from the powder diffraction results. Thus, 111 and 200 have nearly the expected values and only 110 has a larger value and 211 has a smaller value.

Hereafter, these four relative intensities will be considered to be non-textured values for the sake of comparison of textures between homogeneous, undeformed original state and that of forged or

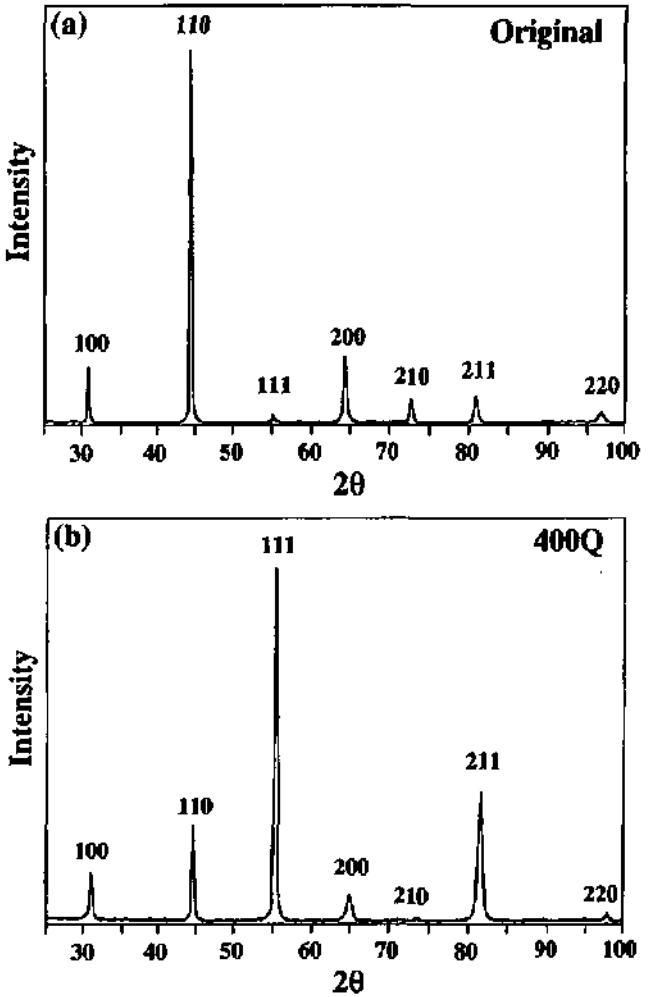

Fig. 4-24 X-ray diffraction spectra of original state (a) and 400°C forged rapid quenched state (b)

heat treated samples. The sample forged at 400°C in fig. 4-24 (b) is characterised by a very strong 111 superlattice peak, a 211 reflection of the expected intensity, a weak 110 reflection and very weak 200 reflection. The pronounced change caused by forging compared with that of the

undeformed state is the very weak 111 reflection becoming a very strong one. The ratio of relative intensities 110/111/200/211 is 1/82/11/7 and suggests an extremely large fraction of planes parallel to the surface of 111 type, a very small amount of 110 type and a reasonable amount of 200 and 211, indicating a strongly enhanced 111 texture, a weakened 200 and 211 and greatly weakened 110 planes.

X-ray spectra of 500°C deformed and of 500°C forged and annealed samples are shown in fig. 4-25 (a) and (b) respectively. The spectrum of the forged state exhibits very strong 111 reflection and, thus, a very high fraction of planes parallel to 111 types, which are similar to that of 400°C forged state. The forging at 400°C and 500°C leads to a same type of deformation texture characterised by very strong 111 relative intensity and very weak 110 one. The investigation of the effect of anneal at 800°C for 10 minutes was carried out and the x-ray spectrum is shown in fig. 4-25 (b). It is evident that such an anneal did not result in a change neither in the intensities of reflections examined nor in the relative intensities calculated after this relatively small deformation (25% height reduction) and low temperature, short time annealing. Subtle changes such as the breadth at half maximum intensity d of the peaks before and after anneal were seen. The d value before annealing is larger than that after annealing, indicating the residual stress in the forged state (peaks of larger breadth) and stress relaxed condition after anneal (peaks of smaller breadth).

Forging at 600°C resulted in similar x-ray spectra and similar texture (represented by relative intensities) to that of forging at 400°C and 500°C, exhibiting a very strong 111 reflection, a very weak 110 reflection and relatively weak 200 and 211 reflections. The intensities of the diffraction peaks and the relative intensities stayed unchanged after anneal.

Forging at higher temperatures and forging followed by annealing led to some variation of x-ray spectra and relative intensities compared with that of forging at lower temperature (400°C, 500°C, 600°C). Fig. 4-26 (a) shows the intensities of various reflections and relative intensities of the four major plane types of the 800°C forged sample, featuring very a strong 111 reflection, a strong 110 reflection, weak 211 and very weak 200 reflections, while the relative intensities demonstrate uniquely a very strong 111 fraction, with the other three fractions remaining very weak (including that of the 110 plane type) and are expressed by the proportion of $f_{\{110\}}/f_{\{111\}}/f_{\{200\}}/f_{\{211\}}$, here 2/89/5/5. Annealing of the sample forged at 800°C gives rise to major changes in both the x-ray spectra and the relative intensities as shown in fig. 4-26 (b), featuring strong 110 and 200 reflections with weak 211 and very weak 111 reflections. Thus the planar fractions parallel to the section are then largely 200 planes, with small and nearly equal amounts of the other three types of planes, indicated by the relative intensities of these four planes. Even here a strong 110 peak did not necessarily mean a large fraction of 110 planes parallel to the section surface due to the changes occurring during the conversion from peak intensity to relative intensity normalised against the

textureless powder spectrum. Thus the strong 110 reflection is translated to a low relative intensity, and hence a small planar fraction on the section surface based on the relative intensity calculation.

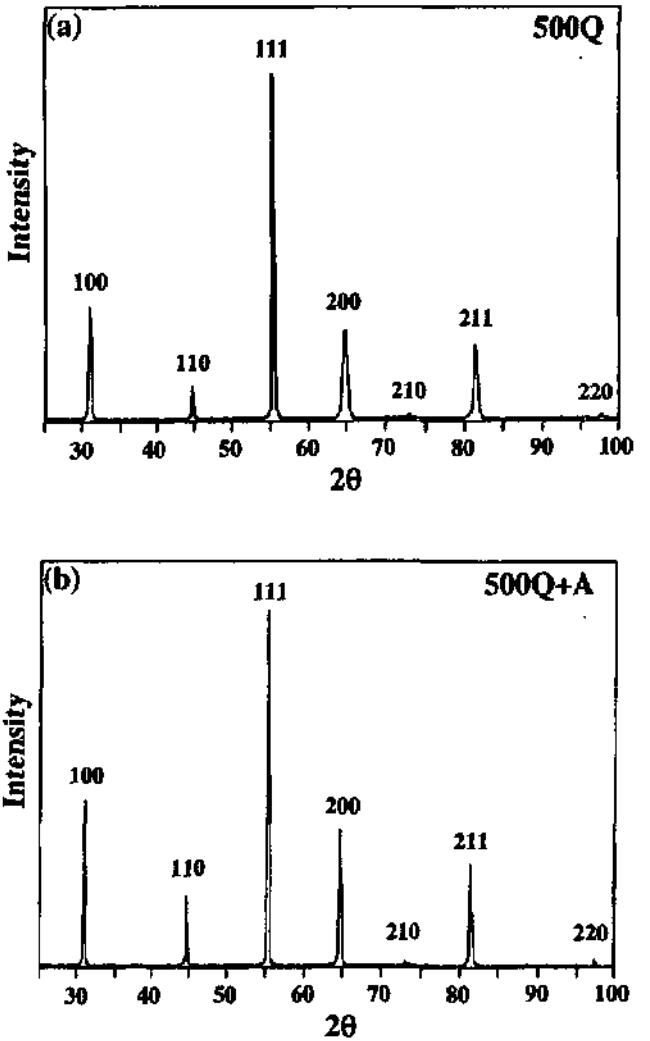

Fig. 4-25 X-ray diffraction spectra and relative intensities showing 500°C forged state (a) and that of forged and annealed state (b)

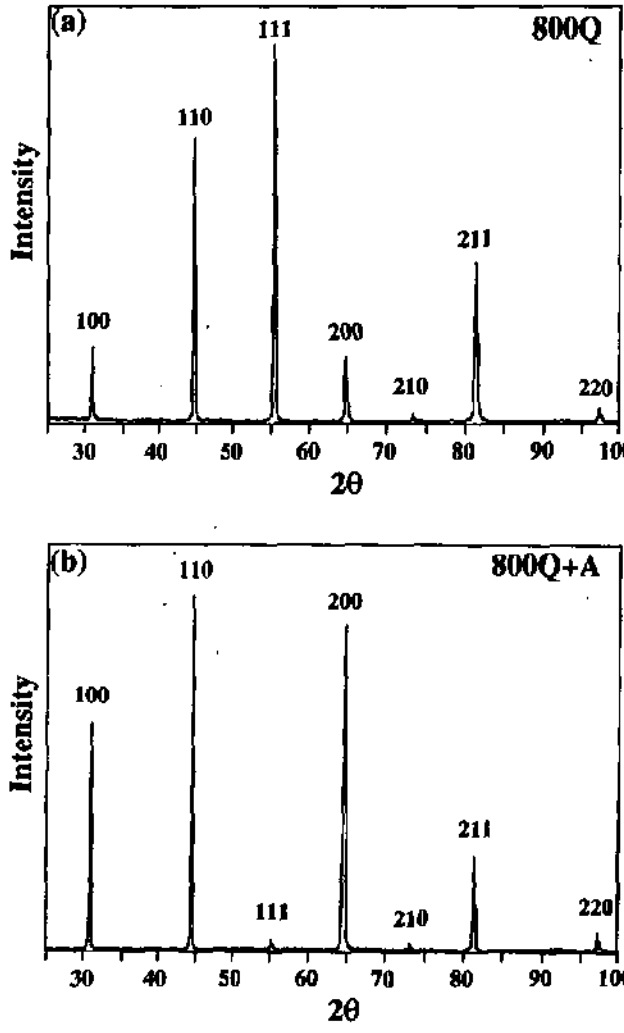

Fig. 4-26 Texture evolution by forging at 800°C (a) and by forging+annealing (b)

X-ray spectra and relative intensities of forging at 900°C rapid quenching, forging at 900°C slow quenching as well as 900°C rapid quenching + annealing are shown in fig. 4-27 (a)-(c)

respectively. The spectrum of forging at 900°C and rapid quenching is characterised by a very strong 200 peak, strong 110 and 111 peaks and less strong 211 peak shown in fig. 4-27 (a), while the slow quenched sample after forging featured a very strong 110 reflection, a strong 200 reflection, weak 111 and 211 reflections, whereas the spectrum of the forged slow quenched +annealed state showed 110 peaks to be very strong. To consider the relative intensities of these three conditions in the order of (a), (b), (c), the planar fraction of 111 planes decreases from

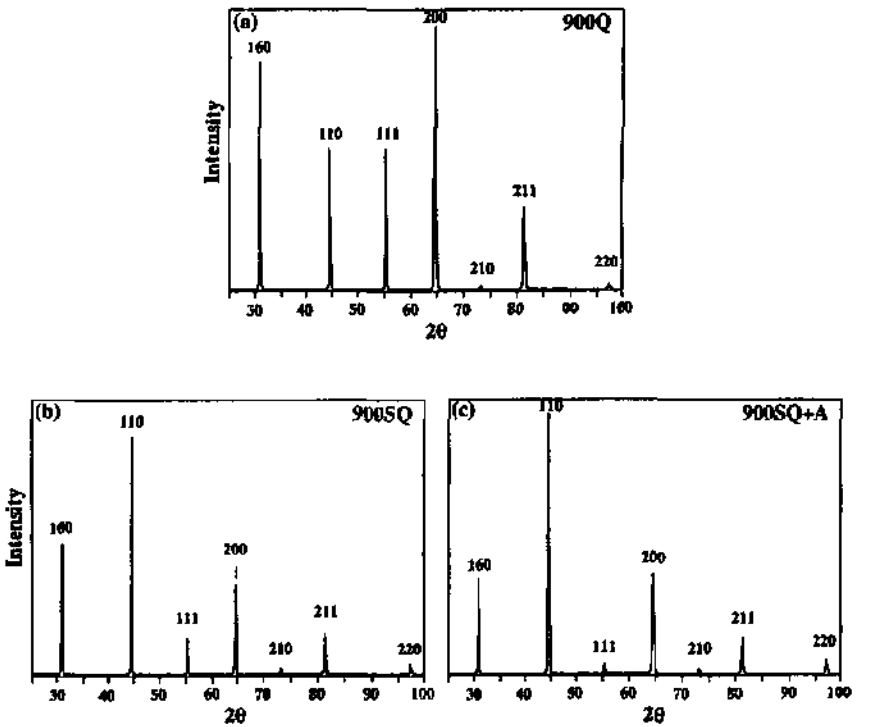

Fig. 4-27 Diffraction spectra and relative intensities of the samples forged at 900°C and rapid quenched (a), forged at 900°C and slow quenched (b) and forged at 900°C slow quenched and annealed (c)

70→54→13, the planar fractions of 110, 200 and 211 increase from 1→7→15, from 23→32→62 and from 6→7→10 respectively. Slow quenching after forging and annealing have substantially weakened the planar fraction parallel to 111 planes and greatly enhanced the planar fractions parallel to 200 and strengthened the 110 and 211 reflections to a certain extent.

The results in fig. 4-26 and fig. 4-27 indicate that annealing of the sample forged at 800°C and that forged at 900°C leads to significant changes in the relative intensities, featuring a drop in the relative intensity of the 111 peak a pronounced increase in that of the 200 peak and a small increment in that of the 110 and 211 peaks. The diffraction spectrum and relative intensities of the sample forged at 900°C and rapid quenched with a larger deformation (70% in height reduction) are similar to that of the sample forged at 900°C and annealed and the relative intensities are similar in these two cases, thus a fairly large quantity of recrystallization was expected.

X-ray spectra and the relative intensities of the sample forged at 1000°C and rapid quenched indicate that at such a elevated temperature, the planar fraction of planes parallel to 111 type on the section surface is further weakened compared with that of forging and rapid quenching at 800°C and at 900°C.

Table 4-3 Ratio of normalised x-ray intensities and relative intensities $f_{(hkl)}$

Material state (forging, cooling and heat treatment)	Ratio of normalised intensity				Relative intensity			
	{110}	{111}	{200}	{211}	{110}	{111}	{200}	{211}
initial	100	63	70	22	39	25	27	9
400Q	1	100	13	9	1	82	11	7
500Q	1	100	10	8	1	85	9	5
500Q+A	1	100	12	4	1	85	10	3
600Q	1	100	10	5	1	86	8	4
600Q+A	1	100	9	5	1	86	8	4
800Q	2	100	5	5	2	89	5	5
800Q+A	9	14	100	12	7	10	74	9
900Q	2	100	38	8	1	70	23	6
900SQ	13	100	59	12	7	54	32	7
900SQ+A	24	21	100	16	15	13	62	10
900Q (ε=70%)	23	33	100	29	12	18	55	15
1000Q	16	100	25	27	9	60	15	16

Note: Q-rapid quenched, SQ-slow quenched, A-anneal at 800°C for 10 minutes

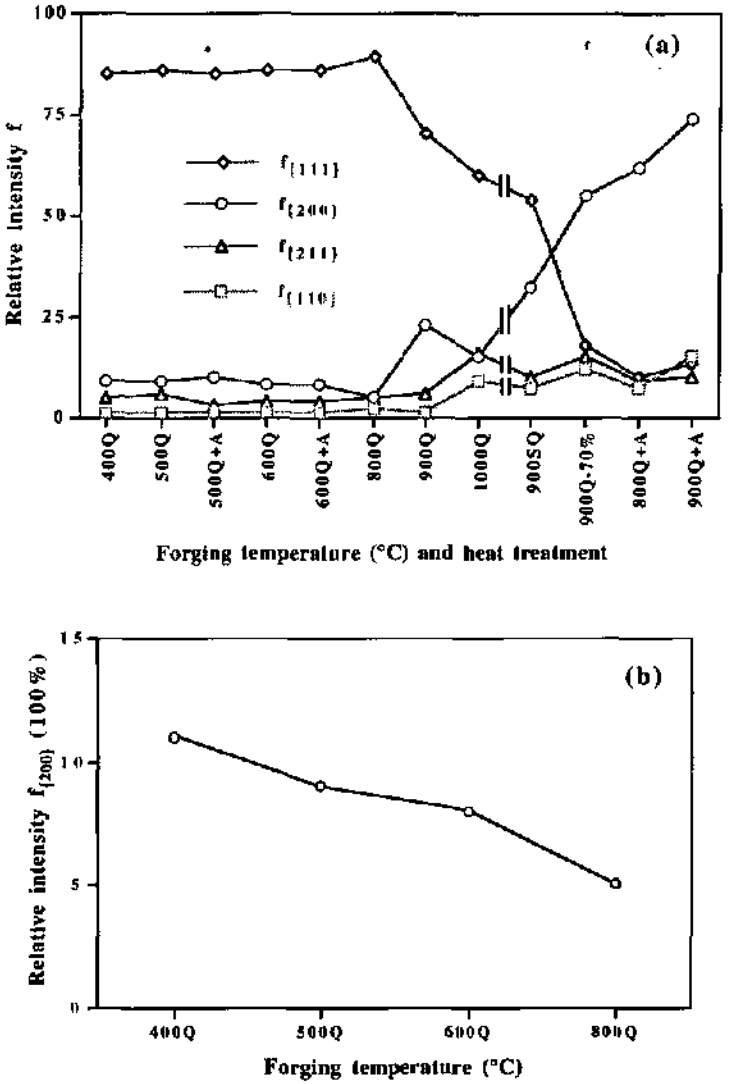

Fig. 4-28 Variation of relative intensities of four major reflections as function of forging temperature and post quenching and annealing treatment (a) and the comparison of f{200} when relative intensity axis is amplified

A Summary of x-ray diffraction results is shown below:

Fig. 4-28 (a) summarises the relative intensities in different states, including forging temperature, post quenching following forging as well as annealing. $f_{\{111\}}$ and $f_{\{200\}}$ change in an opposite sense as the temperature increases: the drop of $f_{\{111\}}$ corresponds to the increase of $f_{\{200\}}$. $f_{\{111\}}$ was always very high when forging was carried out at and below 800°C and decreases on forging at 900°C and in the conditions of slow quenching, larger deformation and annealing. $f_{\{200\}}$ stayed very low upon forging at and below 800°C. In addition, there is a slight decrease of $f_{\{200\}}$ when the forging temperature increases from 400°C to 800°C as shown more clearly in fig. 4-28 (b), which is an important observation for the discussion of texture evolution during forging by different slip systems. $f_{\{110\}}$ and $f_{\{211\}}$ were generally low and they increased slightly with the forging temperature. The delay before quenching has largely weakened $f_{\{111\}}$ and greatly strengthened $f_{\{200\}}$. This suggests that forging texture is {111} while annealing texture is {200}. In summary: the initial state shows a rather weak texture; forging at low temperatures leads to a strong 111 texture, with the 200 texture decreasing (11% to 5%) as the forging temperature increases (400°C to 800°C); annealing after low temperature forging hardly changes the texture for the annealing treatment given; annealing after high temperature forging (also during forging at 900-1000°C) leads to the increase of the 200 texture contribution.

4.4. Transmission electron microscopy and dislocation analysis

Transmission electron microscopy was applied to observation of microstructure in detail: determination of crystalline orientation as well as dislocation analysis (Burgers vector, glide plane, line direction and Schmid factor with respect to loading axis) for the samples forged at various temperatures. Close attention was paid to the analysis of forging at low temperature (below the expected transition temperature) and at high temperature (above the expected transition temperature). Thus, the transmission electron microscopy was conducted on samples forged at 400°C and 500°C (low temperature forging) and samples forged at 800°C and 1000°C (high temperature forging).

The TEM observation is usually confined to a very small volume of the sample and the information obtained from such a small space can hardly describe the general condition of the sample. Therefore the observation should be repeated on different areas in various thin foils prepared from different positions in the forged sample and the large number of analysed dislocations can consequently convey the overall information. As a result, several thin foils were prepared and observed for each forging temperature in order to obtain information as detailed as possible, so the results can reasonably represent the average condition of the forged sample.

4.4.1. Forging at 400°C

The deformed microstructure after forging at 400°C is shown in fig. 4-29, showing a high dislocation density. The analysed grain orientation is near [011]. Many areas were scanned in order to determine the crystalline orientation, which all exhibited nearly the same orientation because the thin foil field was generally in the same original grain with a large grain size. In any case there is very little difference of the orientation from place to place consistent with the slight variation of contrast at different sites shown in fig. 4-29.

Fig. 4-29 Deformed microstructure upon forging at 400°C showing high density of dislocation

Detailed examination of the area marked by A in fig. 4-29 is shown in fig. 4-30 (a)-(e). For weak beam imaging, the contrast condition was generally near the g:4g condition. Tilting to at least three major non-zonal zone axes (for example from the initial [111], to [011], [101], and to either [001] or [110]) imaging with at least five g vectors were carried out to identify both the Burgers vector and dislocation line direction, hence, the glide plane as well as Schmid factor (here, three zone axes: [111], [001], [011] and five g vectors $g=1\bar{1}0$, $g=\bar{1}01$, $g=020$, $g=0\bar{1}1$ and $g=110$ were used). In this field, most of the dislocations (89%) have <111> Burgers vector as is shown clearly by the dissociation into two partials and they are divided into two categories: $[11\bar{1}]$ and $[\bar{1}11]$. Four [010] and one [001] dislocations were observed, while no <110> was observed in this field. The many $[\bar{1}11]$ dislocations, lying in nearly the same direction and marked in fig. 4-30

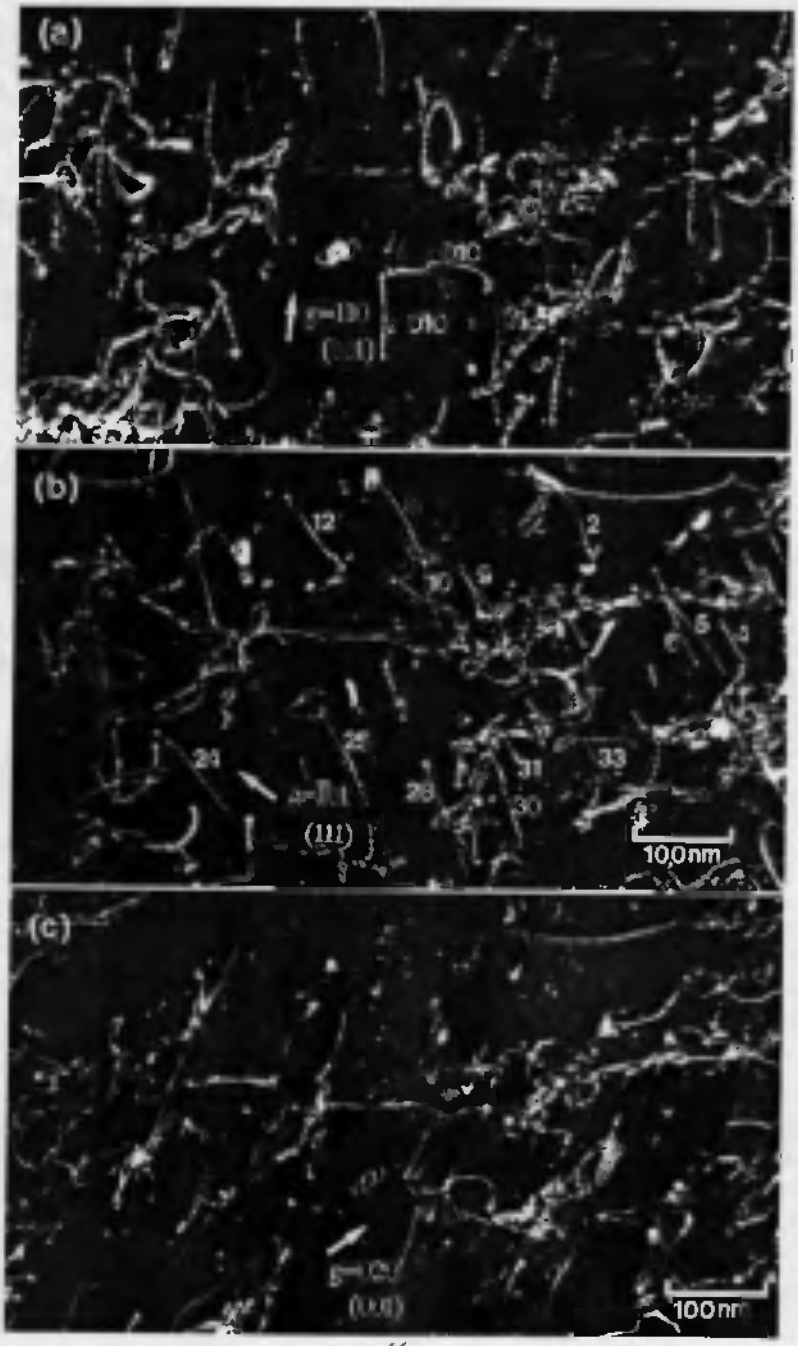
(a)
(b)
(c)
100nm
100nm

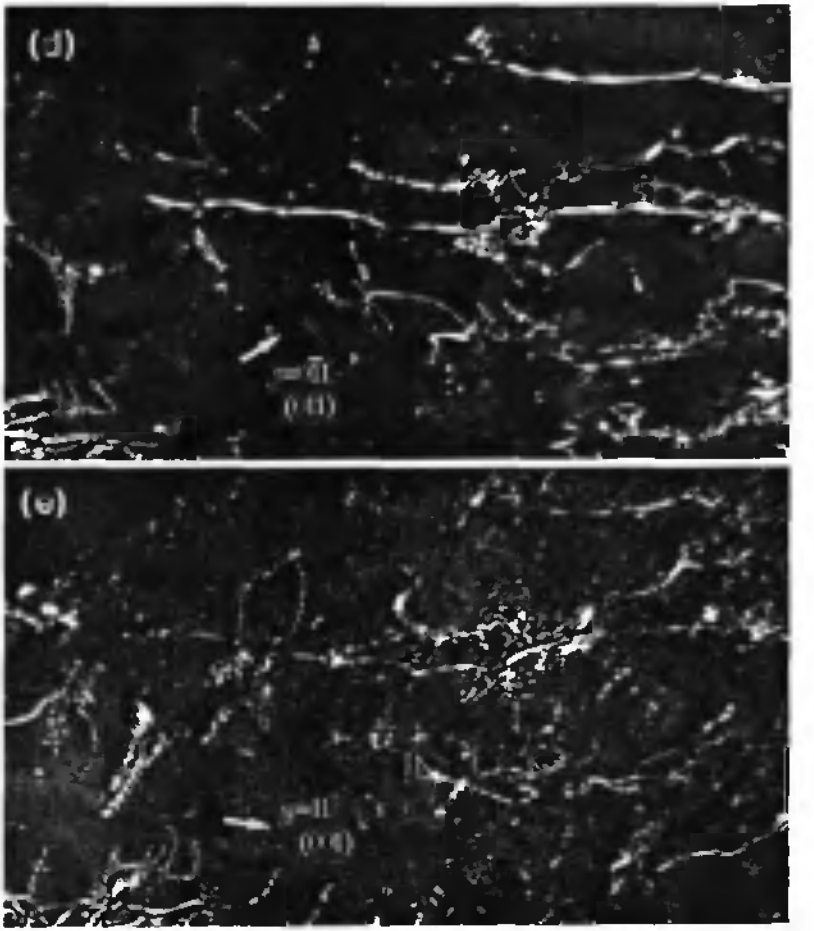

Fig. 4-30 Weak beam micrographs of sample forged at 400°C. Compression axis: near[011]. (a) zone axis]001], g=1 $\bar{1}$ 0; (b) zone axis [111], g= $\bar{1}$ 01; (c) zone axis]001], g=020; (d) zone axis [011], g=0 $\bar{1}$ 1; (e) zone axis [001], g=110

(b) by the same numbers as shown in appendix I. are near screw dislocations. The non-screw dislocations in fig. 4-30 with the same Burgers vector have a high Schmid factor (>0.4) mostly gliding on {110} planes and a few of them gliding on {211} planes. Only two of them have a Schmid factor of zero because their glide plane (0 $\bar{1}$ 1) is perpendicular to the thin foil and the loading axis. In contrast, [1 1 $\bar{1}$] dislocations have a Schmid factor of zero since the Burgers vector is perpendicular to the forging axis. Such dislocations make up only a small fraction of the total

dislocations. The presence of these [1 1 $\bar{1}$] dislocations indicates that their Schmid factor was not exactly zero, implying that the foil orientation was not exactly [011], thus the shear stress acted on them was not zero. Accordingly, the [111] dislocations gliding on ($\bar{1}$01) which could have high Schmid factor were not observed due to the deviation of the foil orientation from the [011] direction, hence, a lower Schmid factor. Therefore, the [$\bar{1}$ 1 1] dislocations and [1 $\bar{1}$] ones may be considered as the primary slip and second slip respectively. The five <100> dislocations (making up 11% of the total dislocations analysed) have low Schmid factors. A jog produced by interaction of two [010] dislocations, gliding on (101) and (100) respectively, was observed shown more clearly in fig. 4-30 (marked by arrow). Theoretically, these two [010] dislocations could not produce a jog due to the same Burgers vector when they moved in the same direction. Nevertheless, they lay in different directions and one of them has a zero Schmid factor and stayed unmoved while another one had a high Schmid factor and moved during deformation and consequently the interaction between them occurred resulting in a jog. The analysis results of the dislocations in this area are shown in appendix I (d-dislocation, g-diffraction vector, b- Burgers vector, u-dislocation line direction, p-glide plane and m-Schmid factor) , showing the <111> dislocation domination as a percentage of total number of dislocations. <100> dislocations did not contribute significantly to deformation of the analysed grain. As such the dislocation configuratinn of the material forged at 400°C is characterised by the easy glide of <111> dislocations presumably with the cross slip of screw dislocations and glide on several {110} planes, as well as a few dislocations on {211} planes.

Another thin foil with the orientation (forging axis) near [111] (2nd thin foil in appendix III) was examined and the dislocation structure is shown in fig. 4-31. This field is characterised by long <111> dislocations (making up 74% of the total analysed dislocations) and a few long curved [001] dislocations but no <110> dislocations. Most <111> dislocations are [1 $\bar{1}$ 1] Burgers vector and only two of them have [1 1 $\bar{1}$] Burgers vector. Interestingly, nearly all these <111> dislocations are screw dislocations except one [1 $\bar{1}$ 1] possessing a high Schmid factor m=0.47. Four [001] dislocations gliding on (110) plane also have a high Schmid factor. This suggests that the orientation of the analysed grain was favourable to the movement of dislocations of both <111> and [00$\bar{1}$] Burgers vectors. The analysis also confirms the predominance of <111> screw dislocations and only rarely is there dislocation interaction. Dislocation 2 is curled at mid-length due probably to the drag of a jog produced by interaction with a forest dislocation. Small dislocation loops may be produced by continued dislocation movement.

A third thin foil of the sample forged at 400°C (3rd thin foil in appendix III) was found to have an orientation near [011] and the analysed result of dislocation types (appendix II) showed that no <100> dislocation was found in the observed field and there exists only one [110] dislocation gliding on a ($\bar{1}$10) plane with a low Schmid factor (m=0.25). The rest are all <111> ones (about 95% of the total dislocations) among which three [1 1 $\bar{1}$] gliding on (101) plane have a Schmid

factor of zero and the others have the screw configuration. Small jogs were seen on some <111> screw dislocations and they were probably caused by the interaction of dislocations gliding on different planes with different line directions. The main feature of this field is also the predominance of <111> dislocations.

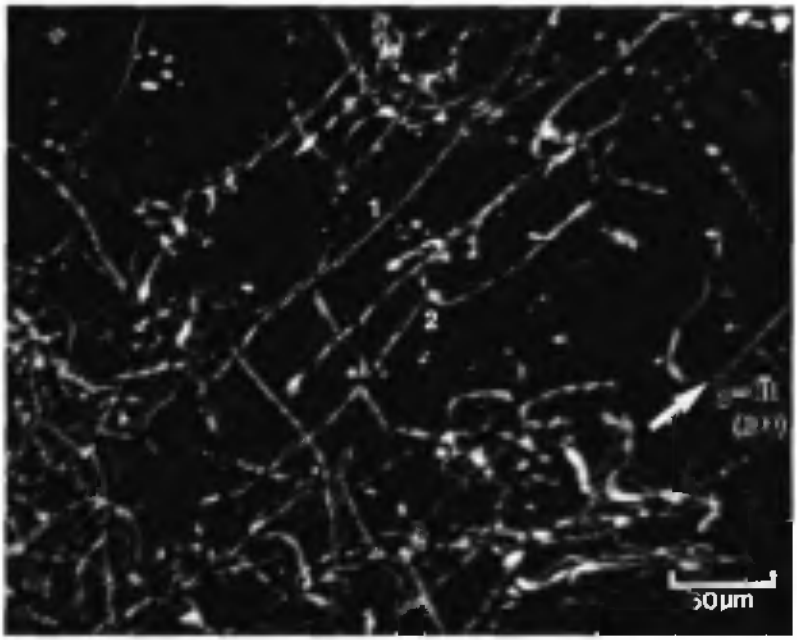

Fig. 4-31 Weak beam micrographs of another thin foil of sample forged at 400°C. Compression axis: near [111]. Zone axis [100], g=0$\bar{1}$1

The summary of the dislocation structures produced by forging at 400°C is shown in appendix III, considering the orientation of the analysed grain, the fraction of each type of dislocation, the Schmid factor and the percentage of dislocation of each type. It is evident that nearly 90% of dislocations are <111> type and most of them are screw dislocations or mixed dislocations gliding mostly on {011} planes with a high Schmid factor. Very few <100> and nearly no <110> dislocation were observed. The structure of dislocations change little from one thin foil to another but principally most of them are long and smooth indicating the easy glide of <111> dislocations during deformation at this temperature.

4.4.2. Forging at 500°C

Observation of the material forged at 500°C at various magnifications showed a high density of dislocations having some similar features to the material forged at 400°C. Several thin foils were

examined and they had such orientations as [001], [212] or [331] as estimated by analysis of diffraction patterns and Kicuchi lines. Detailed investigation revealed some difference between the dislocation configurations after forging at 400°C and at 500°C.

Fig. 4-32 shows in detail an area examined of the 500°C forged sample (1st thin foil in appendix VII) imagined using g vectors (020, 200). Imaging by these two g vectors provides some important information about the analysed dislocations shown in the photos. More than half of the analysed dislocations (57%) are <111> type composed of mainly two variants (determined from other images with a variety of diffraction vectors): $[\bar{1}11]$ and [111] and most of them lay in the screw direction with a few exceptions. These edge dislocations were shown to lie on {110} planes and possess a high Schmid factor. The $[\bar{1}11]$ dislocations are approximately horizontal in this figure while the [111] ones are near vertical. Some curved dislocations exhibit screw segments and edge segments, for example dislocation 1 shows a screw segment (near horizontal direction) and a mixed segment (near vertical direction), and zigzagged dislocation 2 shows the screw sections (near vertical direction) and the mixed sections. For these two dislocations no climb happened as seen by their uniform separations, and as confirmed from the analysis of Burgers vector and line direction which confirmed the habit plane to be a glide plane.

An important feature of many other <111> screw dislocations in this field is the gliding away from each other of two partials, for example, dislocation 3, 10, 12 shown by a curled section or the kinks, indicating the occurrence of cross-slip of screw superdislocations. A more detailed analysis of two screw dislocations 10 and 12 showed that a partial glided away onto $(1\,\bar{1}\,2)$ plane, suggesting that the cross-slip of a $[1\,1\,\bar{1}]$ partial to $(1\,\bar{1}\,2)$ plane happened during deformation. Many dislocation loops were observed and they played a role as obstacles to dislocation gliding, thus the interactions between dislocations and these loops happened and led to the curling of subsequent dislocation lines and an increased resistance of dislocation movement. Such loops are presumably formed at a jog (or other obstacle) preventing the movement at one point on the superdislocation, which bends around the obstacle, forming a dipole, which breaks off the dislocation, the dipole subsequently rounding to the loop shape. Beside these <111> dislocations, some <100> dislocations (34% of the total dislocations) gliding on {100} or {110} planes were identified in this area. Only one [011] dislocation was observed. All the <100> and this [011] dislocations have zero Schmid factor regardless of their variants and glide plane. The three variants of <100> dislocations were not present in equal numbers; here 11 [100] dislocations, 11 [001] dislocations but no [010] dislocation was found, suggesting that they were not the result of the decomposition of <111> dislocations (in this case approximately equal numbers of each type of <100> dislocations would be expected). The analysed results of this area including Burgers vector, dislocation line direction, glide plane as well as Schmid factor is summarised in appendix IV.

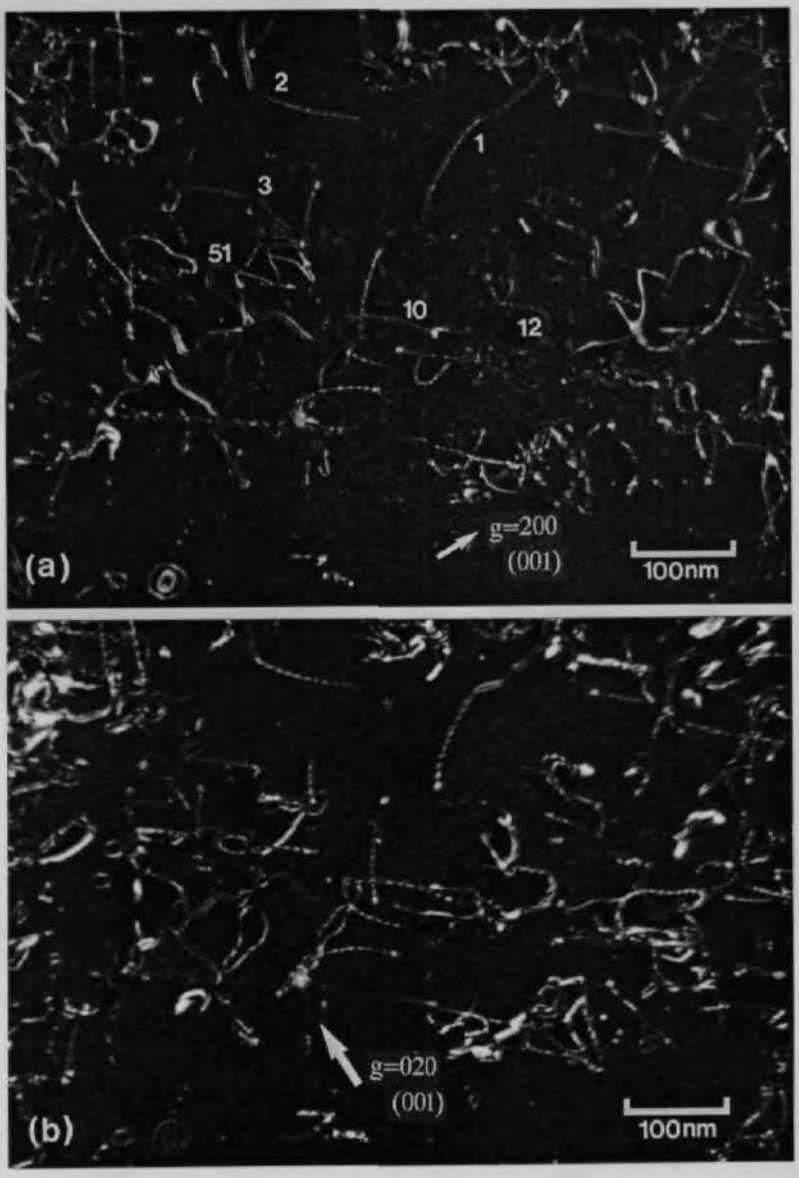

Fig. 4-32 Weak beam micrographs of 500°C forged material
(a) zone axis [001], g=200; (b) zone axis [001], g=020

Another thin foil prepared from the material forged at 500°C was examined and the weak beam micrograph is shown in fig. 4-33 (2nd thin foil, field one in appendix VII). The foil orientation (loading axis) was estimated as being less than 2° from [212] direction for the grain analysed.

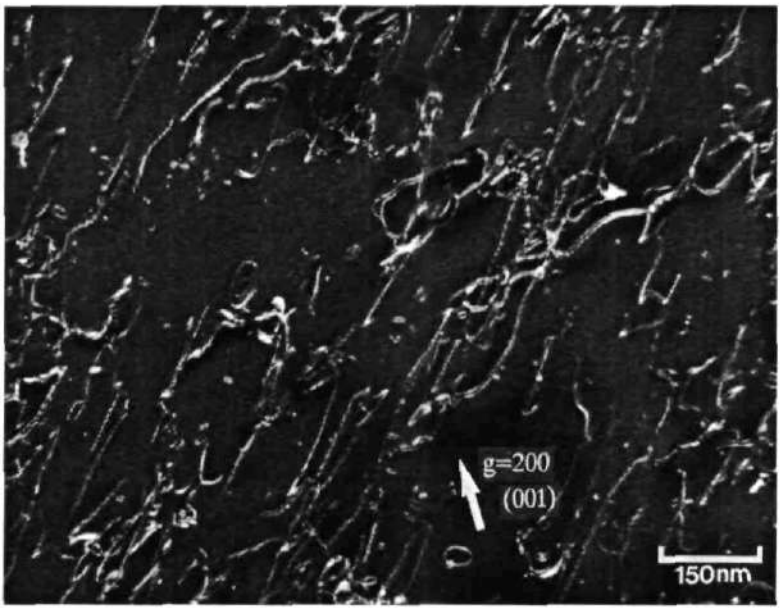

Fig. 4-33 Bright field image showing the deformed microstructure of another thin foil prepared from the material forged at 500°C. Zone axis [001], g=200

In this area, more than half (53%) of the total dislocations was identified to be <111> type and some of them are screw types. The edges <111> dislocations are shown to glide on {110} or {211}planes and some exhibit a low Schmid factor. Cross-slip of some <111> dislocations was seen. Some <100> dislocations with high Schmid factor (m=0.47) were observed and they glide mostly on (110) plane. Some dislocations of <110> type were also seen and they have a low Schmid factor (m=0.16-0.17). It can be concluded that in this region, the deformation was dominated by mainly <111> dislocations. In addition <100> dislocations also contributed slightly to deformation. Some small dislocation loops, concentric loops and fine debris were observed in this area.

Another area in the same thin foil (2nd thin foil, field two in appendix VII) as that of fig. 4-33 was examined in detail and the weak beam micrographs and the analysed results of dislocation types (appendix V) showed that about three quarters of total dislocations are <111> type. Two thirds of

these <111> dislocations are screw ones and the rest are analysed to glide on {110} or on {211} planes possessing a relatively low Schmid factor. One stepped dislocation (with $[\bar{1}11]$ Burgers vector) has both edge and screw segments gliding on the (101) plane. The observed [001] dislocations making up of about 15% of the total dislocations have generally a high Schmid factor (0.44-0.47) while two [010] ones have a Schmid factor of zero. Some <110> dislocations with a low Schmid factor (0.16-0.17) were seen and they glide principally on {011} planes. A dissociation of a dislocation $1/2[\bar{1}11] \rightarrow 1/2[\bar{1}10] + 001$ was observed. Here $1/2[\bar{1}11]$ and 001 dislocations have a high Schmid factor while the $1/2[\bar{1}10]$ has a low one, suggesting that this dissociated $1/2[\bar{1}10]$ dislocation was not mobile and acted as an obstacle impeding the further movement of $1/2[\bar{1}11]$ and 001 dislocations. Some dislocation loops were also seen but were fewer than shown in fig. 4-33. Climbing was rarely seen in the material forged at this temperature.

A third thin foil was prepared from the sample forged at 500°C with the orientation near [331] and the dislocation analysis results are shown in appendix VI. Weak beam examination and the analysis showed that the <111> dislocations, making up 60% of total dislocations, have a variety of Schmid factors. Some of them have a Schmid factor lower than 0.25, indicating an incompatibility between slip system and loading axis direction, and others have a high Schmid factor of 0.45. The non-screw <111> dislocations glide on {110} and many of them glide on {211} planes. There were, in addition, fewer screw <111> dislocations in this region. The <110> dislocations were estimated as being 23% of total dislocations, having a low Schmid factor 0.21-0.22 and some of them have a zero Schmid factor. *<100> dislocations, accounting for 16% of total dislocations, have generally* low Schmid factor except for a few dislocations of type [100] on (011), [100] on $(0\bar{1}1)$ and [100] on (010).

In summary, the dislocation structure of material forged at 500°C has the following features compared with that of material forged at 400°C: i) a slightly lower percentage of <111> dislocations of the total dislocations, hence, a slightly increased proportion of <100> and <110> dislocations (the percentages of <100>, <110> and <111> dislocations at 400°C are 12%, 1% and 87% respectively, while that at 500°C they are 24%, 12% and 64% respectively); 2) proportion of screw <111> dislocation of all <111> type is lower than that of the 400°C forged condition; 3) more <111> dislocations gliding on {211} planes; 4) cross-slip of the superdislocations were observed more frequently; 5) dislocation loops were observed while they were rarely seen in the material forged at 400°C. The characteristics of dislocations of the 500°C forged condition are summarised in appendix VII.

4.4.3. Forging at 800°C

Several thin foils were prepared and many areas were studied for the sample forged at 800°C. Bright field images were used for the determination of dislocation characteristics since most of the dislocations were <100> type and only few dissociated <111> ones were observed by weak beam

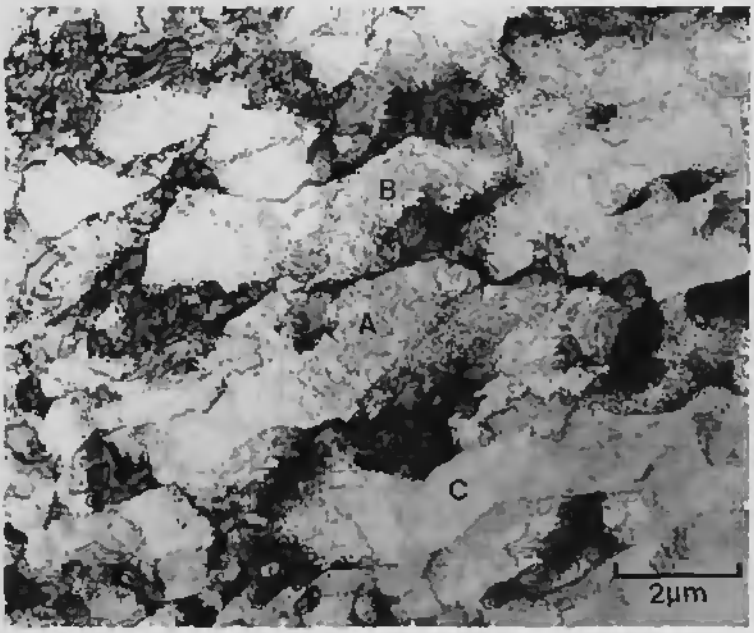

Fig. 4-34 Bright field image of material forged at 800°C showing highly deformed microstructure composed of loose prolonged subgrains. Zone axis [111], g=$\bar{1}01$

imaging. The long exposure time and careful setting up of contrast condition needed for viewing a large number of thin foils and many areas, particularly for some thicker areas of foils, meant that weak beam micrographs were not generally taken. Bright field micrographs were obtained using different g vectors (at least 5) in various zone axis, sufficient to analyse the dislocations.

Fig. 4-34. shows the heavily deformed microstructure composed of fine loose subgrains having a similar crystal orientation near [111] which is consistent with x-ray diffraction results showing strong {111} texture ($f_{\{111\}}$=89%, table 4-2). The deformed microstructures upon forging at high temperature (above 800°C) were generally composed of loose sub-grains with high dislocation density both in the wall regions and in the subgrains. The orientation deviation of one subgrain from another is very small, for example, the deviation among the subgrains A, B, C is estimated by

Kikuchi patterns as being less than 2°. Very similar structures as well as identical subgrain orientations near [111] were found in other areas of the same foil. The subgrain size is about 1-2μm, and most of them are more or less elongated in the same direction.

Fig. 4-35 illustrates some typical dislocations found in subgrain A in fig. 4-34. Bright field images obtained using two g vectors $\bar{1}01$ and $0\bar{1}1$ in two zone axes, (111) and (011) respectively, show analysed dislocations for the sample forged at 800°C. The vast majority (89%) of analysed dislocations in this subgrain have <100> Burgers vectors presenting all three variants but not in equal numbers (more[100] than [010] than [001]). Such dislocations were typically present in 45-90° edge directions and lay on {001} planes with intermediate to high Schmid factors (m=0.33-0.47) and on {011} planes with low or high Schmid factors depending on the combination of Burgers vector, glide plane and crystalline orientation of the analysed grain. Some <110> dislocations were observed lying on {001} or {011} planes with a zero Schmid factor. Such dislocations are presumably formed by interactions between <100> dislocations. No <111> dislocation was found in this area.

Detailed examination of subgrains B and C in fig. 4-34 showed similar microstructure to that of subgrain A. Dislocation analysis results of these two areas are shown in appendix VIII and IX respectively. Appendix VIII (sub-grain B) shows that 90% of total dislocations have <100> Burgers vectors and they glide on both {001} and {011} planes with mostly high Schmid factors (0.33-0.47), and they exhibit unequal numbers of the three variants (here 17 [100] dislocations, 10 [010] dislocations and 21 [001] ones), suggesting that these <100> dislocations were unlikely the result of <111> decomposition. These dislocations lay in such directions as [001], [$\bar{1}$01], [130], etc., presenting also 45-90° edge directions. There were four <110> dislocations (making up 8% of total dislocations): two [011] ones glide on (100) and ($2\bar{1}1$) planes with Schmid factor of 0.47 and 0.38 respectively with the [$\bar{1}$10] dislocations gliding on (110) plane having zero Schmid factor. Only one [$1\bar{1}1$] dislocation was observed as <111> type and it glides on (011) plane with a intermediate Schmid factor (m=0.27). This dislocation was presumably generated by the reaction (association of <100> dislocations).

Dislocation analysis result of subgrain C listed in appendix IX shows that the <100> dislocations amount to 88%, gliding principally on {001} and {011} planes with intermediate to high Schmid factors (0.33-0.47), and unequal number of three variants were observed (9 [100] dislocations , 23 [010] dislocations and 10 [001] ones). Most of them present in [001], [011], [012], [013], as well as [111] type directions, thus as 45-90° edge dislocations. Three <110> dislocations (accounting for 6% of total dislocations) were identified:[$\bar{1}$10], [011] and [$\bar{1}$01], gliding on (110), (100) and ($1\bar{1}1$) planes with Schmid factors of 0, 0.47 and 0 respectively. The [011] dislocation

resulted from the interaction of two <100> dislocations as described by the following equation (Burgers vector, glide plane as well as Schmid factor are indicated):

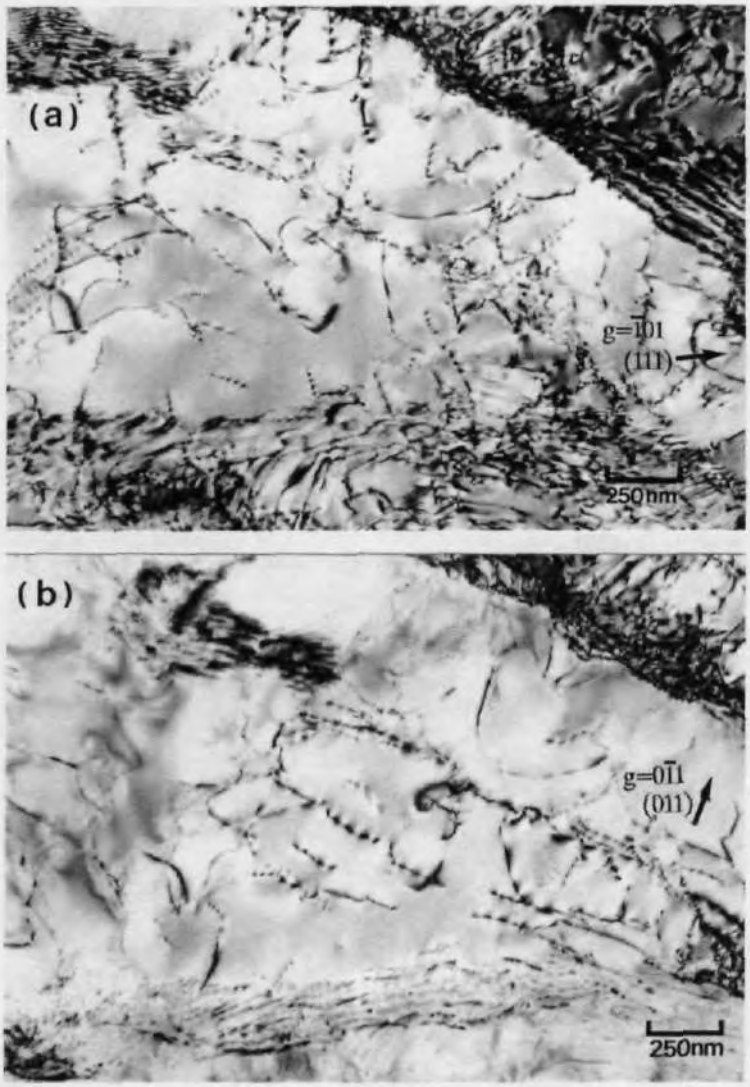

Fig. 4-35 Bright field images of sub-grain A shown in fig. 4-33
(a) zone axis [111], g= $\bar{1}$01; (b) zone axis [011], g=0 $\bar{1}$ 1

[001]	+	[010]	→	[011]
(010)		(100)		(100)
m=0.33		m=0.33		m=0.47

This reaction was confirmed by high magnification examination of the dislocations involved. In this sub-grain, three $[\bar{1}11]$ dislocations (making up 6% of total dislocations) were observed and they glide on $(0\bar{1}1)$, (110) and (101) with Schmid factors of 0, 0.27 and 0.27 respectively.

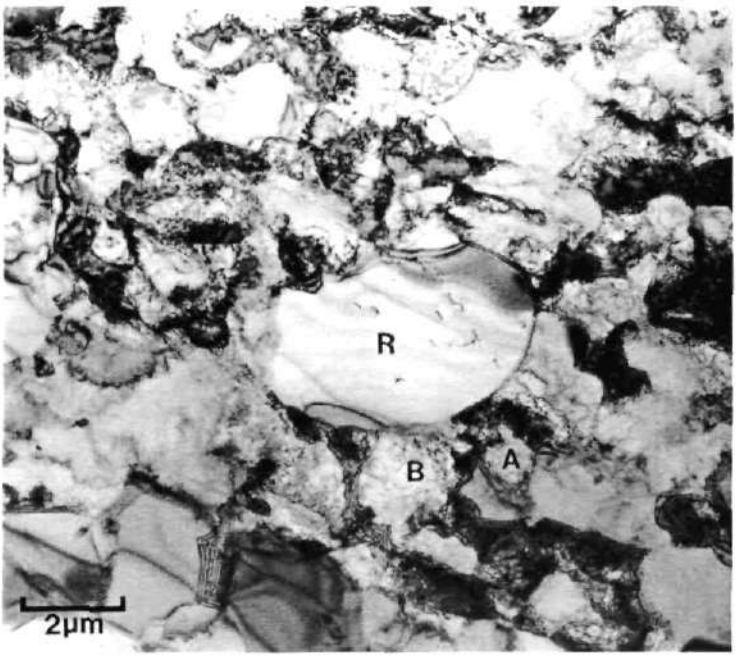

Fig. 4-36 Bright field image of second thin foil prepared from material forged at 800°C showing some recrystallized grains dispersed in the loose subgrains with high dislocation density

Fig. 4-36 is a low magnification bright field image of another thin foil prepared from the same sample forged at 800°C. Some recrystallized grains are seen, about 5μm in size, dispersed in the fine, highly deformed loose sub-grains, 0.5-1μm in size. The orientation of the recrystallized grains has changed greatly (about 55°) relative to the deformed subgrains. All subgrains exhibited a very high dislocation density while very few dislocations were found in the recrystallized grains.

There were about ten dislocations in the recrystallized grain R (in the middle of the photo). The orientations of numerous subgrains and recrystallized grains were studied with respect to the loading axis by Kikuchi line analysis on double tilting the thin foil. For seventeen analysed sub-grains, all of them exhibited an orientation near <111> (their {111} plane was approximately parallel to the thin foil) with a deviation of 2.6°-3.5°. For eight studied recrystallized grains, six of them had a <001> orientation with a deviation of 2.7°-3.8° and two others oriented near {011} with a deviation of 3.5°-4.5°. Such analysis results are closely consistent with the x-ray diffraction examination.

A sub-grain A near the recrystallized grain (2nd thin foil, field one in appendix XI) in fig. 4-36 was identified to be oriented to [111] direction and the dislocation analysis results demonstrate that 80% of dislocations in this sub-grain are <100> type with unequal number of the three variants [100], [010] and [001], gliding on {001}, {011} and occasionally on {012} planes. Most of these <100> dislocations have intermediate to high Schmid factors (0.33-0.47). Four <110> dislocations were observed gliding principally on {001} planes. Only one [111] dislocation was seen and determined to glide on $(1\,1\,\bar{2})$ plane with Schmid factor of zero.

Another sub-grain B (2nd thin foil, field two in appendix XI) in fig. 3-36 was studied and many dislocations were examined. Most of analysed dislocations (82%) are <100> type, gliding on both {001} and {011} planes with intermediate to high Schmid factor (0.33-0.47). A few <110> dislocations were found to glide on {001} planes with zero or intermediate Schmid factor. No <111> dislocation was observed in this area. A dislocation interaction was found and identified as follows (Burgers vector, glide plane and Schmid factor are indicated):

$$\begin{array}{ccccc} [100] & + & [001] & \rightarrow & [101] \\ (011) & & (010) & & (010) \\ m=0.47 & & m=0.33 & & m=0.33 \end{array}$$

Such an interaction indicates again that the <110> dislocations likely resulted from <100> dislocation interactions.

Fig. 4-37 shows in detail a recrystallized grain (2nd thin foil, field three in appendix XI) in fig. 4-36. A few dislocations were observed in this newly formed grain and most of them were determined to have Burgers vector of type <110>, occasionally <100> and <111> with Schmid factor near zero for almost all dislocations. Such a low Schmid factor indicates that either it was incompatibility stresses between the soft, just-recrystallized grain and the surrounding hard, unrecrystallized subgrains, or undefined thermal stresses that induced the deformation.

Another thin foil prepared from the sample forged at 800°C was investigated, featuring fine subgrains amongst which were dispersed some equiaxed recrystallized grains. Orientation evaluation of these subgrains and some recrystallized grains was carried out and similar results to those in fig. 4-37 were obtained: the vast majority of sub-grains were oriented near <111> directions and most of recrystallized grains oriented to near <001> directions.

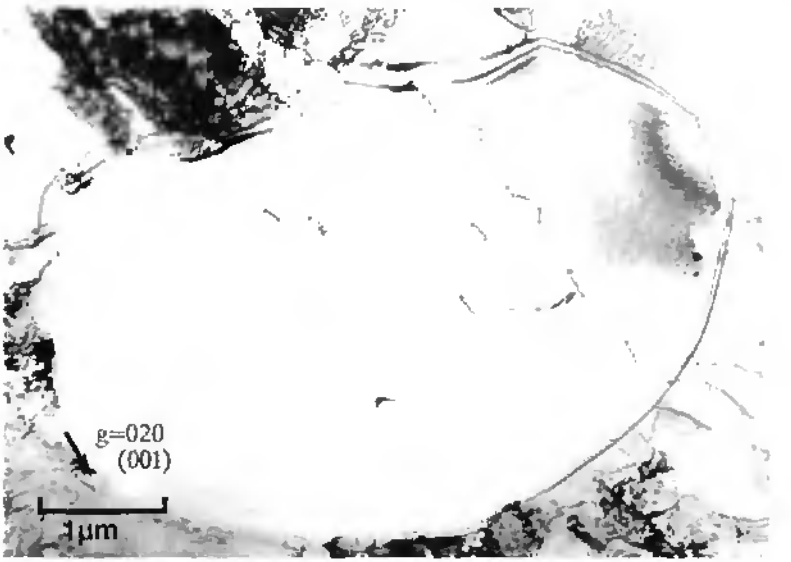

Fig. 4-37 Bright field image showing a recrystallized grain in fig. 4-36

A recrystallized grain in this foil (3rd thin foil, field one in appendix X1) was studied and the dislocations were analysed. In this grain, <100> dislocations account for near 80% gliding prevailingly on {001} and {011} planes, occasionally on {012} planes. Nearly all of these dislocations had zero Schmid factor, suggesting incompatibility between direction of loading and the grain orientation. The ratio of three variants [100]:[010]:[001] is 4:4:5, which is far from equal and this suggests that in such a just-recrystallized grain <100> dislocations were not likely generated by the decomposition of <111> dislocations. In contrast, some <100> dislocations near and arranged perpendicular to the grain boundary were seen and were likely generated from the grain boundary. Some <110> dislocations were seen with a high Schmid factor, gliding on {011} planes. A few <111> dislocations were determined to glide on {211} plane with a high Schmid factor.

A sub-grain oriented near [111] in the same thin foil (3rd thin foil, field two in appendix XI) was examined and the analysed result showed that <100> dislocations make up of about 80% of total dislocations gliding mostly on {001} and {011} and a very few of them gliding on {012} planes. The majority of these dislocations had a high Schmid factor. Some <110> dislocations were observed and determined to lie on {100} planes, but having a zero Schmid factor. No <111> dislocation was seen in this area.

Another subgrain in this thin foil (3rd thin foil, field three in appendix XI) was examined and the dislocation analysis results are shown in appendix X, illustrating again that the majority of dislocations (82%) are <100> type, gliding on {001} and {011} planes, occasionally on {012} planes. Most of these dislocations had high Schmid factors. The ratio of three variants is [100]:[010]:[001]=12:29:9, which does not support the suggestion of the formation of <100> dislocations by < 111> decomposition. Some <110> dislocations (about 15%) were determined to glide on {001} planes, possessing an intermediate Schmid factor. Only two <111> dislocations were observed and they glided on {011} planes with a intermediate Schmid factor.

Another thin foil was prepared from the sample forged at 800°C and a recrystallized grain in this foil was examined to investigate the dislocation configurations in this just-recrystallized grain (4th thin foil, field one in appendix XI). The orientation of this foil was [101] (the foil is parallel to (101) plane of the recrystallized grain) and the bright field micrographs are shown in fig. 4-38. Dislocation analysis showed that <100> dislocations account for 89% of the total dislocations while<111> dislocations account for only 11%. No <110> dislocation was observed. There are many long straight dislocations near the grain boundary and they are parallel each other. Such dislocations have Burgers vectors [001] (for example, dislocations 1, 2, 3, 23, 28, 29, 32, etc.) or [100] (for example, dislocations 30, 31, 33, 36,etc.). The [001] dislocations glide on (100) plane while the [100] dislocations glide on (001) plane, thus a very high Schmid factor 0.5 was obtained referring to the [101] orientation of this grain which is highly favourable to the slip of such dislocation configurations. They are mostly 45°-90° edge dislocations with line directions {010}, <012>~<013>, etc. and were responsible for the deformation. The [001] and [100] dislocations did not glide on the (010) plane, which has a zero Schmid factor because the plane is perpendicular to the crystalline orientation, hence, to the loading axis. Similarly, all the dislocations with [010] Burgers vector have a zero Schmid factor (for example, dislocations 4-8, 24-26, etc.) because such a Burgers vector is perpendicular to the grain orientation, hence, to the loading axis. The combination of unfavourable Burgers vector, slip plane and crystalline orientation limited movement of such dislocations. A few stepped dislocations, 56, 57, 58, were determined to have [001] Burgers vector and the segments parallel to those long straight <100> dislocations lay on

(100) with high Schmid factor (0.5), while the segments perpendicular to those long, straight <100> dislocations lay on (010) plane with a zero Schmid factor. Such dislocations are suggested

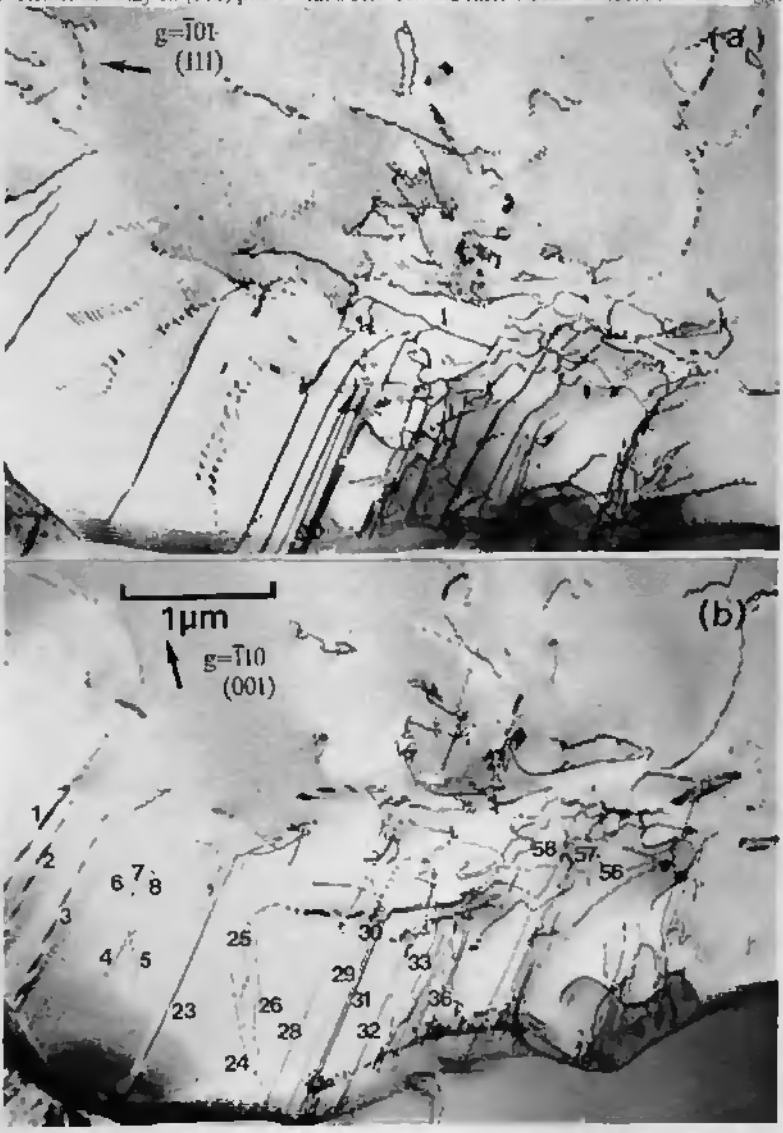

Fig. 4-38 Bright field images of a recrystallized grain in fourth thin foil of material forged at 800°C. (a) zone axis [111], g= $\bar{1}$01; (b) zone axis [001], g= $\bar{1}$10

resulted from the relaxation of long curved mixed dislocations. There were also a few [100] dislocations gliding on {011} planes with a Schmid factor (0.35). Some <111> dislocations were found to glide on {011} and {211} planes with high Schmid factor (0.41-0.47). The dislocation analysis of another recrystallized grain also showed the dominance of <100> dislocations with high Schmid factor (4th thin foil, field two in appendix XI).

In brief, the deformation of this newly recrystallized grain was dominated by <100> slip owing to the favourable combination of Burgers vector, glide plane and grain orientation.

In conclusion, different areas in various thin foils prepared from the sample forged at 800°C were examined and the dislocations were analysed and summarised in appendix XI. About 80% of dislocations are <100> type gliding on both {001} and {011} planes with generally high Schmid factor both in the deformed subgrains and in the just-recrystallized grains. Neither the numbers of three variants [100], [010] and [001] nor the number of these three variants with high Schmid factor are equal, suggesting that they did not likely resulted from the dissociation of <111> dislocations. <110> dislocations account for a very small fraction of total dislocations, gliding on principally {001} and {011} planes with low or high Schmid factor depending on the combination of Burgers vector, glide plane as well as crystalline orientation. Some dislocation reactions of <100> to produce <110> dislocations were observed and such reactions suggest that the <110> dislocations probably resulted from the encounter and reaction of <100> dislocations rather than <111> decomposition. <111> dislocations make up also a small part of the total dislocations and they glide mostly on {011} and {211} planes with different values of Schmid factor depending on their configuration with respect to crystalline orientation.

4.4.4. Forging at 1000°C

In order to investigate the dislocation structure in the material forged at even higher temperature, several thin foils were prepared and examined in the same way as for the analyses mentioned above. The deformed microstructure of material forged at 1000°C is shown in fig. 4-39, featuring a high dislocation density and loose subgrains which have a larger size (2-5μm) than those in the samples forged at 800°C. Many sub-grains were examined and found to have an orientation near [111], and there was only a slight deviation of orientation between these subgrains.

A subgrain in fig. 4-39 (marked A) (1st thin foil in appendix XIII) was studied and a bright field micrograph image using g vector $0\bar{1}1$ in zone (111) is shown in fig. 4-40. Dislocation analysis illustrates that <100> dislocations amount to 90% of total dislocations and they glided on {001} and $\{01\bar{1}\}$ planes with generally high Schmid factor (0.33-0.47). The ratio of three variants is [100]:[010]:[001]=5:34:25. The pile-up seen in the upper-left corner is composed of such [010] dislocations, lying in the [100] direction and on the (001) plane. The distance between the

dislocations in such a pile-up decreases as a function of the distance from dislocation 1 to the tail of the pile-up, due to the interaction forces between them[104]. Another pile-up at the lower right corner is composed of [001] dislocations, lying in the [010] direction, and on the (100) plane. Since the foil orientation is near the [111] direction and this photo was taken in axis zone (111), then the angle between the dislocation line of these two groups of dislocations is about 60°. The few <111> dislocations (7% of total dislocations) lie in {011} planes and have generally moderate to high Schmid factors. Only two <110> dislocations were seen. The reaction of two <100> dislocations A and B to produce a <110> dislocation C was identified and is expressed as follows:

$$\begin{array}{ccccc} [001] & + & [0\bar{1}0] & \rightarrow & [0\bar{1}1] \\ (010) & & (001) & & (100) \\ m=0.33 & & m=0.33 & & m=0 \end{array}$$

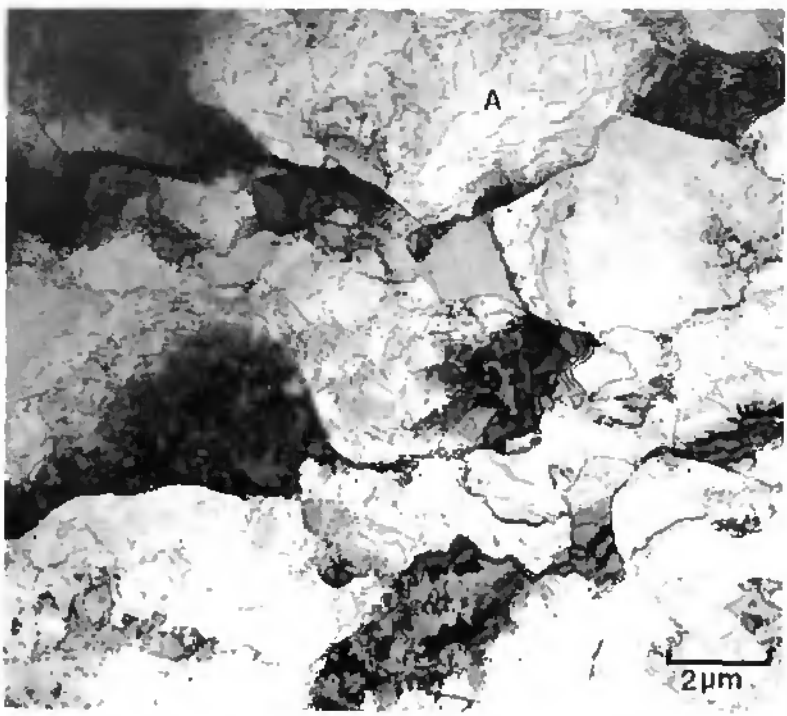

Fig. 4-39 Bright field image of material forged at 1000°C showing loose subgrains. Zone axis [111], g= $\bar{1}01$

The newly formed $\{0\,\bar{1}\,1\}$ dislocation had a zero Schmid factor, and such a reaction suggests that at 1000°C, many of the <110> dislocations are probably generated by <100> dislocations rather than by <111> decomposition or by the motion and multiplication of the <110> dislocations themselves.

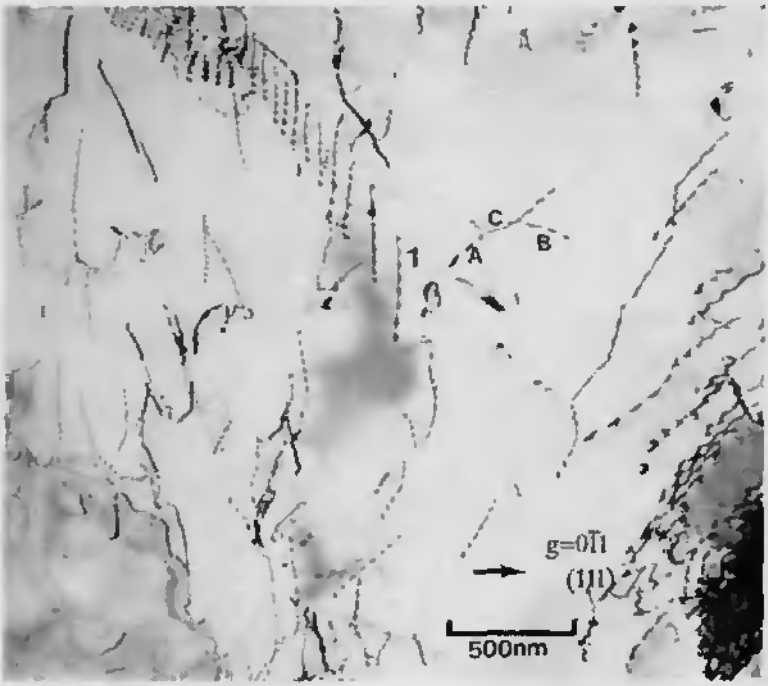

Fig. 4-40 Bright field images of subgrain A in fig. 4-39. Zone axis [111], g=0 $\bar{1}$ 1

Fig. 4-41 shows the bright field micrographs (imaged using five g vectors) of another thin foil of the material forged at 1000°C as an example of dislocation analysis (2nd thin foil, field one in appendix XIII). The <100> dislocations amount to about 80% of total dislocations, gliding mostly on {001} planes and occasionally on {011} planes and {012} planes, possessing mostly high Schmid factor (0.33-0.47). The ratio of three variants is [100]:[010]:[001]=14:7:29, evidently not equal in number. A pile-up of [001] dislocations was seen to lie in the [100] direction, and on (011) plane, and finally to form a subgrain boundary. Some long <100> dislocations were observed and the reactions of <100> dislocations to form <110> dislocations were seen (marked by A and B in fig. 3-41(a)) and illustrated as:

$$[001] + [\bar{1}00] \rightarrow [\bar{1}10]$$
$$(100) \quad (001)$$
$$m=0.33 \quad m=0.33 \quad \text{screw}$$

Such dislocation reactions suggest again that <100> dislocation interaction is responsible for the formation of <110> dislocations even at 1000°C during forging.

Another subgrain in the same thin foil (2nd thin foil, field two in appendix XIII) was examined and the bright field images and dislocation analysis are shown in fig. 4-42 and in appendix XII respectively. Again, 80% of total dislocations are <100> type, with most of them gliding on generally {001} planes with moderate Schmid factor and a few of them gliding on {011} and {012} planes with high Schmid factor. It is well worth noting that at the corners of the photos, there are four groups of dislocations gliding on different planes marked by A, B, C and D receptively. Group A is in fact a pile-up of [100] dislocations, lying in the [010] direction, and on a (001) plane. Group B is also a pile-up of dislocations but composed of [010] type, lying in the [100] direction and also on a (001) plane. Group C is composed of [001] dislocations, lying in the [010] direction and on a (100) plane, while group D is composed also of [001] dislocations but lying in the[100] direction and on a (010) plane. These four groups of dislocations can allow such a [111] oriented grain to deform with no change of orientation. A few <111> dislocations were seen to glide on {011} planes with zero to intermediate Schmid factor. A very few <110> dislocations were observed and the $[0\,\bar{1}\,1]$ variant has zero Schmid factor because it is perpendicular to the foil with, hence, zero shear stress.

A [001] oriented subgrain with respect to loading axis in another thin foil (3rd thin foil in appendix XIII) was studied and the dislocation analysis showed that the fraction of <100> dislocations (70%) is smaller than that in preceding areas and all the [100] and [010] ones have a zero Schmid factor due to the right angle between such Burgers vectors and the crystalline orientation (loading axis). Many [001] dislocations lying on (010) plane also have a zero Schmid factor because of the right angle between such a plane and the loading axis. Some <110> dislocations were found to glide on {011} planes with a high Schmid factor. A few <111> dislocations were found to glide on (011) and (211) planes with moderate to high Schmid factors and a small number of <110> type were also observed, gliding mainly on {011} planes with high Schmid factor owing to the favourable combination of Burgers vector, glide plane and sub-grain orientation.

In summary, the microstructure and dislocations of material forged at 1000°C exhibit a great similarity with that of the material forged at 800°C: most of the sub-grains analysed have an orientation near [111]; <100> dislocations account for about 80% of total dislocations, gliding generally on {001} and {011} planes with mostly high Schmid factors. The three variants [100],

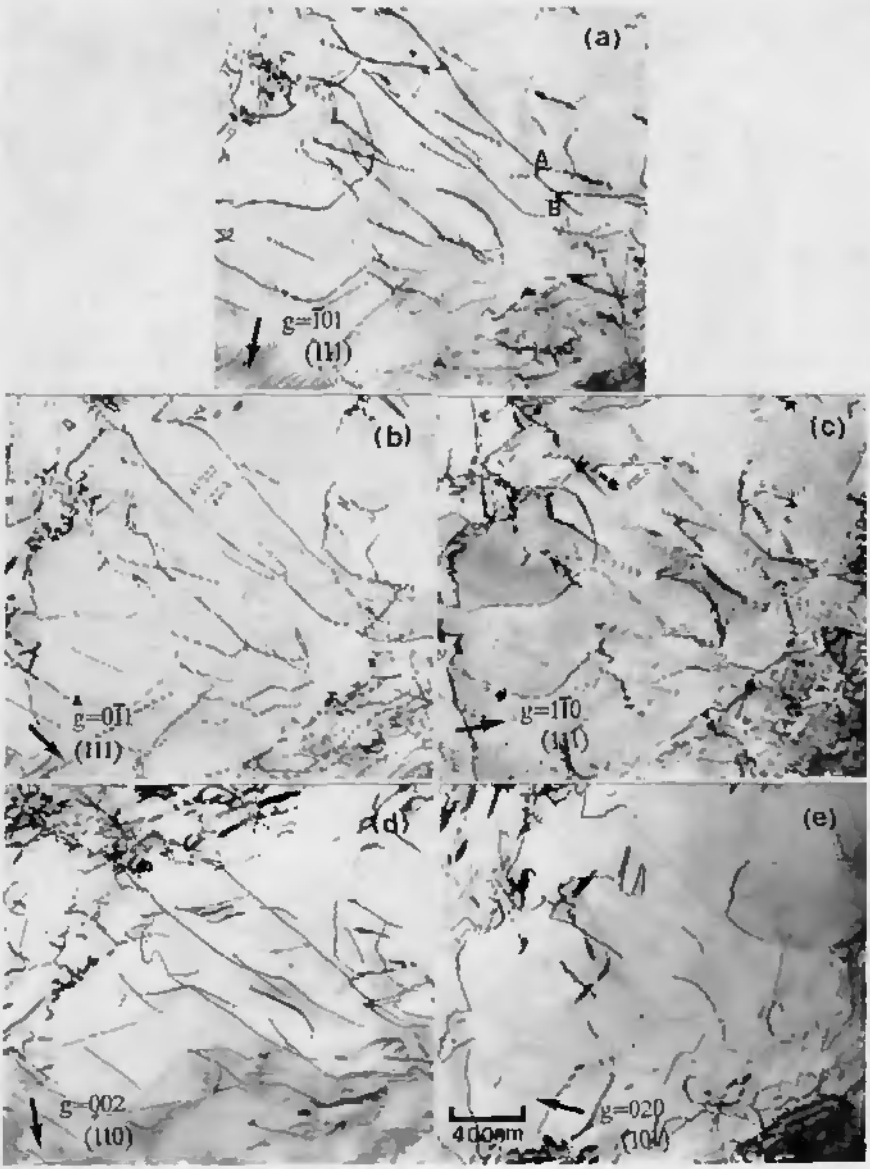

Fig. 4-41 Bright field micrographs of another thin foil of material forged at 1000°C (a) zone axis [11], g=$\bar{1}$01; (b) zone axis [111], g=0$\bar{1}$1; (c) zone axis [111], g=1$\bar{1}$0; (d) zone axis [110], g=002; (e) zone axis [101], g=020

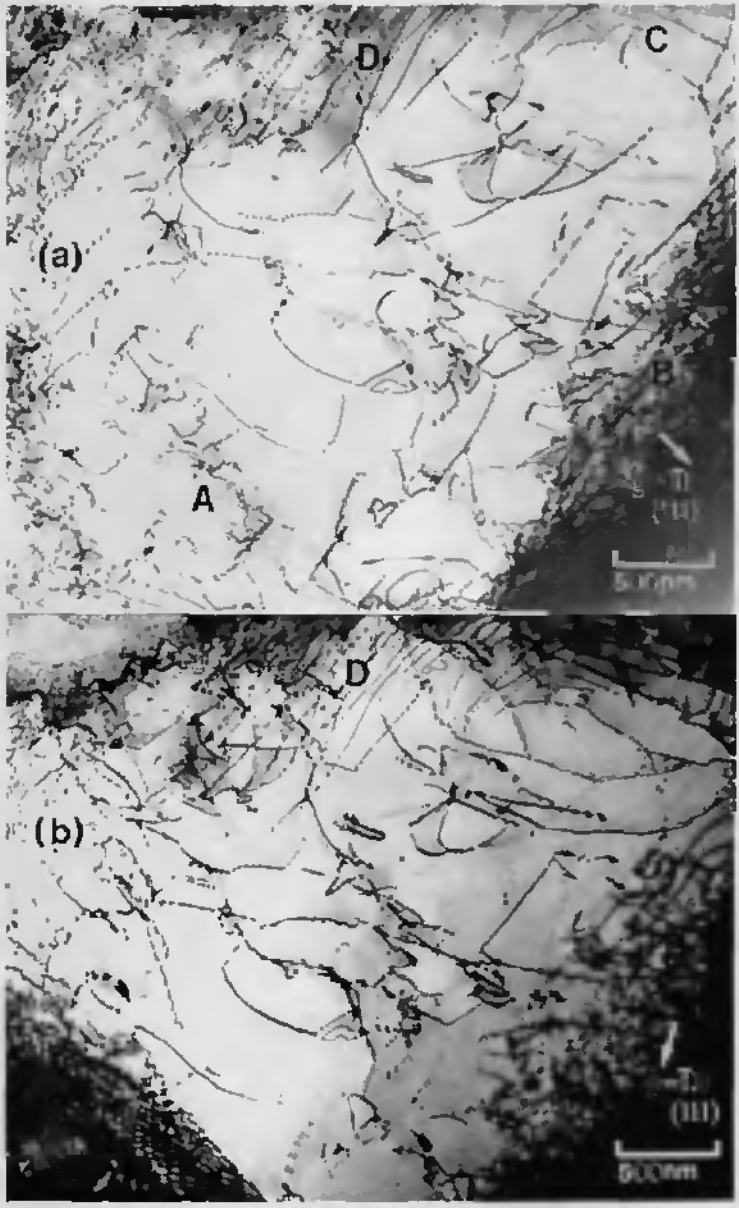

Fig. 4-42 Bright field images of another subgrain in the same foil as that of fig. 4-41. (a) zone axis [111], g=0$\bar{1}$1; (b) zone axis [111], g=$\bar{1}$10

[010] and [001] are not equal in number. Interaction of <100> dislocations to produce <110> dislocations was observed. A few <111> dislocations were found to glide on {011} and {211}planes with low to intermediate, and occasionally high Schmid factor. A small number of <110> dislocations were also seen, gliding on {011} and sometimes on {001} planes with low, intermediate and occasionally high Schmid factor. Finally, there was a difference in the size of the sub-grains in these two conditions. The subgrains in the material forged at 1000°C were coarser than that in the material forged at 800°C. The dislocation analyses of different areas in various thin foils are summarised in appendix XIII.

Discussion and interpretation of results

5. Discussion and interpretation of results

Thermomechanical processing of FeAl type intermetallics is useful not only as a way of obtaining material in suitable shapes but also as a way of modifying the mechanical properties by adopting the appropriate processing scheme based on deformation and recrystallization principles[26, 29, 31]. Forging, rolling, extrusion, etc. are widely used in the forming of intermetallics especially for those which have a mediocre plasticity at room temperature but a very good one at medium or at high temperature. Thus, the understanding of deformation characteristics (deformation texture, recrystallization, grain refinement and finally the deformation systems in a wide range of temperature) are of great importance to predict and control the final microstructure and mechanical properties.

The deformation texture that results from a large amount of straining is closely related to the slip systems and the mechanical behaviour during deformation depends greatly on both the internal state (single crystal or polycrystal, grain size, crystalline orientation, dislocation configuration) and processing condition (temperature, strain rate). Thus, the comprehensive study of deformation texture (macrostructure), slip system or dislocation analysis (microstructure) as well as some mechanical parameters (yield point, maximum stress, work hardening condition) as function of temperature and strain rate can bring light to the understanding of macrostructure and microstructure evolution as well as deformation mechanisms.

5.1. Deformed and recrystallized microstructures--recrystallization and orientation of recrystallized grains

The alloy used for the present studies has uniform and equiaxed grains with grain size of about 1000μm after the annealing treatment before forging as shown in fig. 4-14. The forging process at various temperatures resulted in different microstructures—deformed microstructure at intermediate temperatures (400 and 500°C, fig. 4-15) and mixed microstructure-deformed regions and recrystallized grains at higher temperatures (e.g. 800-1000°C, fig. 3-17-fig. 4-20). The highly deformed microstructure at high temperature is not stable. The stored energy in the form of dislocations is the driving force to recrystallization in the deformed alloys[105, 106] and the driving force is given approximately as $p=\rho Gb^2$ for single phase alloys, where ρ is the dislocation density , b is the Burgers vector and G is shear modulus[106]. If a metal is subjected to a strain rate high enough at high temperature, it is possible that dynamic recrystallization may occur[1]. But at low or at intermediate temperatures with moderate deformation, the driving force and the thermal activation are not high enough to cause dynamic recrystallization and this is supported by true strain-true stress curves of 400°C-600°C forged material, exhibiting no drop of stress after the maximum strength. Only at higher temperatures with larger strain can such recystallization take place. Forging at higher temperatures, for example, at 800°C to 1000°C at a strain rate of about $1s^{-1}$ is favourable to the occurrence of dynamic recrystallization. The detailed observation of these recrystallized

grains showed that the dislocation density varied from one recrystallized grain to another. There were three sorts of recrystallized grains: i) recrystallized grains with fairly high dislocation density, for example, fig. 4-38, which probably recrystallized during deformation and hence subsequently deformed further. During dynamic recrystallization, new grain nuclei at first grow rapidly but the concurrent deformation steadily increases the dislocation density in the recrystallized grains; ii) those which had a very low dislocation density, e.g. the one in the centre of fig. 4-36, which was formed at the end of deformation, thus the deformation introduced dislocations were not numerous. It is also possible that such a few dislocations be introduced by thermal stress during cooling after forging; iii) recrystallized grains in which no dislocation was observed, for example, the small recrystallized grains at low-left corner in fig. 4-36. This type of grains was likely formed after forging before quenching. As described in section 4.2, the deformation was not uniformly distributed in all the original grains, even within the same grain the deformation was different from place to place, so the stored energy is not homogeneous every-where, thus there was a difference in the recrystallization kinetics in different grains or at different sites in the same grain, and consequently recrystallization may not occur simultaneously and uniformly throughout the material. Heavily deformed grains or locations will recrystallize earlier than at places where there is less deformation. The recrystallized grains are more susceptible to deformation than deformed grains due to their low dislocation density and low yield strength and the work hardening of the adjacent deformed grains.

The recrystallized grain size and recrystallized fraction is summarised in fig. 4-23 based on table 4-2 for the convenience of comparison. The recrystallized fraction increases with increase of forging temperature and/or with the addition of a holding time at high temperature as shown by

$$f_r=1-\exp(-Bt^k) \qquad (5\text{-}1)$$

where f_r is the volume fraction recrystallized, t is time and B and k are constants, illustrating the relation between recrystallized fraction and holding time after deformation[1]. When the deformed sample was quenched very quickly, the holding time was very short, so the recrystallized fraction is small; while the deformed sample was held at forging temperature, i.e. the holding time is longer, the recrystallization fraction increases rapidly. Therefore the recrystallized fraction in the slow quenched sample forged at 900°C is fairly high.

At high temperature, the fine grain is not yet stable and further growth of recrystallized grains may occur. This growth as a function of time can be written:

$$D-D_0=kt^n \qquad (5\text{-}2)$$

where D_0 is the initial size of recrystallized grain size , k and n are constants and n<0.5 [106]. So the sample forged and held at forging temperature had a larger grain size than that of rapid quenched sample deformed at the same temperature.

The discussion above confirms the ease of recovery and dynamic recrystallization during high temperature forging and the necessity of rapid cooling after deformation to obtain the real deformed microstructure at high temperature. This point is particularly emphasised by the significant changes brought about during the few seconds before quenching of the 900SQ sample.

The orientation of the recrystallized grains with respect to the forging axis was analysed for the samples deformed at 400°C, 500°C, 800°C and 1000°C. Nearly all the analysed recrystallized grains in 800°C and 1000°C forged material had an orientation near [001] direction. It can be inferred that the ideal recrystallization texture of the present alloy is {001} type. In contrast, the orientation of most of the analysed subgrains had an orientation near [111] and some others had the orientation near [212], [331], [101], etc. Materials forged at 400°C and 500C° and studied by TEM showed various grain orientations because of the small deformation (5% in height reduction). In this case, the grains did not rotate from the original orientations significantly and the deformation texture was not well developed. Thus the orientation of the grains was distributed fairly randomly, exhibiting little or no orientation preference. When a deformed metal is recrystallized the crystallographic orientation of the new grains may be quite different from that of the previously-existing ones. If this is the case, the recrystallized texture will be different from the deformation texture[106]. The development of recrystallized texture is due to the recrystallization grains having a preferred orientation. Otherwise the growth rate of the growing grains may depend on their orientation relative to the deformed matrix[105]. In the present investigation, the [001] orientation of recrystallized grains is very different from that of the deformed subgrains which had mostly the [111] orientation, and this new orientation appears to be well established from the beginning, i.e. the recrystallization texture is determined by nucleation not by growth aspects.

5.2. Evaluation of deformation texture and recrystallization texture

Deformation textures or slip systems in iron aluminides have been investigated by various means (slip trace analysis, x-ray diffraction method as well as simulation of texture development) for a long time. Examination of slip traces on the surface of deformed FeAl samples showed that the slip systems at low temperatures were <111>{011} and <111>{211} [63, 83]. At intermediate temperatures both <111> and <100> slips were observed depending on the crystallographic orientation[66, 84, 107] and at high temperatures, <100> slip was dominant[61]. Analysis of slip traces in individual grains of imperfectly B2 ordered Fe_3Al rolled at moderate temperatures also indicate that <111>{011} and <111>{211} were dominant slip systems [75]. On the other hand, the latest studies by Kad et al show that both Fe_3Al and FeAl deform by <111>{011} and

<111>{112} to very high temperature[80]. The discrepancies of the different conclusions reached by previous investigations have stimulated the start of the present work. In the present study, the relative intensity of a given reflection $f_{\{hkl\}}$ based on x-ray diffraction together with identification of the orientation deformed and recrystallized structures by TEM were employed to assess deformation texture as well as recrystallization texture. In addition, the recrystallized fraction was assessed to understand the relative intensity of x-ray reflections at different forged conditions.

Fig. 5-1 shows the change of relative intensities $f_{\{111\}}$ and $f_{\{200\}}$ as well as the percentage of recrystallization as a function of forging temperature and post annealing.

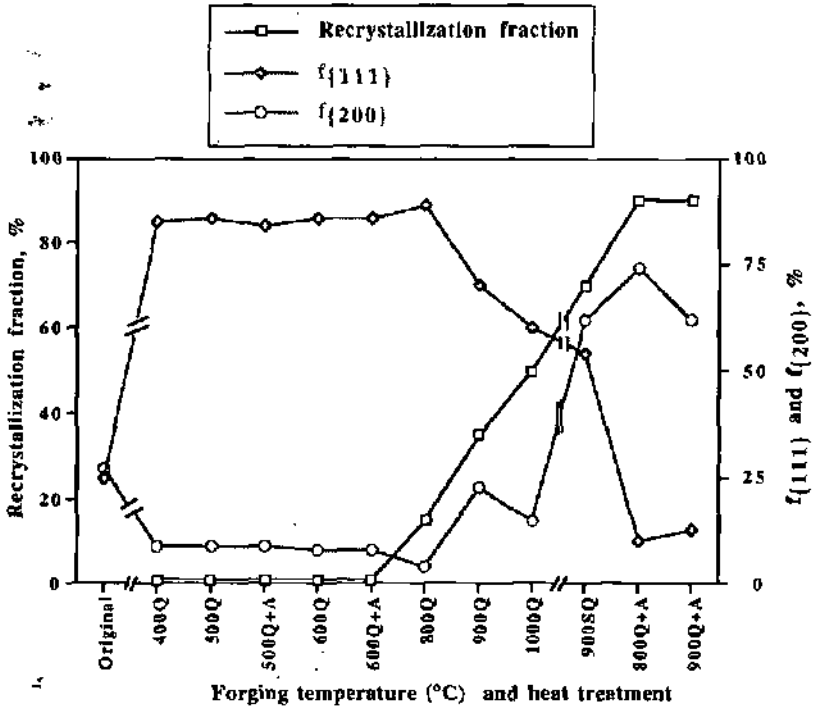

Fig. 5-1 Variation of relative intensity of {111} and {002} reflections and recrystallization fraction as a function of forging temperature, holding time before quenching and annealing

It is clear that the $f_{\{111\}}$ value is very high from the material forged at 400°C to the material forged at 800°C and it decreases with both increasing the forging temperature (e.g. forging at 900°C and at 1000°C) and the holding time at forging temperature (e.g. slow quenching after 900°C quenching).

The post-forging annealing (here 800Q+A and 900SQ+A) has considerably lowered $f_{\{111\}}$. Comparing now the variation of $f_{\{111\}}$ with the variation of recrystallization fraction as a function of forging temperature and the holding time shown in fig. 5-1, it can be seen clearly that these two curves have completely opposite tendencies with changing the forging temperature and holding time as well a the heat treatment condition: high $f_{\{111\}}$ values for forging from 400°C to 800°C correspond to low recrystallization fractions. $f_{\{111\}}$ decreases from 900Q to 900SQ+A monotonically while the recrystallization fraction increases almost linearly. The $f_{\{111\}}$ of 89% (800Q) corresponds to the recrystallization fraction=15% while the $f_{\{111\}}$ of 10% (800Q+A) corresponds to 90% recrystallization fraction. On the contrary, the curve representing $f_{\{200\}}$ has the same form and the same trend as that of the curve of the recrystallization fraction: $f_{\{200\}}$ stays very low from 400Q to 800Q and recrystallization fraction is fairly low, then $f_{\{200\}}$ increases from 800Q to 800Q+A (1000Q is an exception for some unknown reason) and finally decreases a little from 800Q+A to 900SQ+A while recrystallization fraction increases from 800Q to 800Q+A and then increases a little at 900SQ+A. The high values of $f_{\{200\}}$ at 800Q+A and 900SQ+A (74% and 62%) correspond to high recrystallization fractions (90%). Such an opposite trend between $f_{\{111\}}$ and the

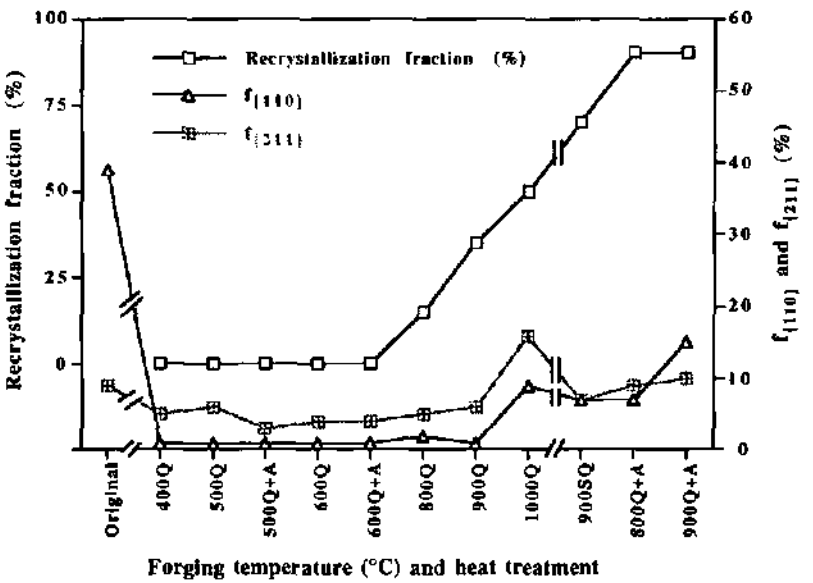

Fig. 5-2 Variation of relative intensity of {011} and {211} reflections and recrystallization fraction as a function of forging temperature, holding time before quenching and annealing

recrystallization fraction and the same trend between $f_{\{200\}}$ and the recrystallization fraction strongly suggest that the non-recrystallized part has the <111> orientation while the recrystallized part orients preferably to <001>. In other words, deformation texture is {111} from intermediate to high temperature and recrystallization texture is {200}.

The variation of $f_{\{110\}}$ and $f_{\{211\}}$ as a function of forging temperature and holding time after forging as well as annealing is shown in fig. 5-2. $f_{\{110\}}$ is very low from 400Q to 900Q and it increases from 900Q to 1000Q and decreases a little at 900SQ, and then increases again until 900SQ+A. $f_{\{211\}}$ has a similar trend to that of $f_{\{110\}}$. However, neither $f_{\{110\}}$ nor $f_{\{211\}}$ changes as much as $f_{\{111\}}$ and $f_{\{200\}}$ as recrystallization takes place from condition 800Q to condition 900SQ+A.

The slip systems must be intimately related to the resultant forging texture, thus the simulation of crystallographic texture based on assumed slip directions and glide planes can allow the determination of the operating slip systems. The present experimental result of texture evaluation is very well consistent with the forging texture simulation conducted by Kad[77]. Three projections, {100}, {110}, and {111}, in simulated pole figure based on <111>{011} and <111>{112} showed (fig. 2-8) that such operating systems produced very strong{111}, very weak {100} and even weaker {110} textures. The relative intensities in the present work shows very high $f_{\{111\}}$, very weak $f_{\{200\}}$, and nearly zero $f_{\{110\}}$ for forging at low or intermediate temperatures (400°C, 500°C and 600°C), suggesting <111> slip directions on {011} or {112} planes upon forging in such a temperature regime. This result is also supported by a rolling experiment on Fe_3Al (rolling at 560°C in B2 ordered regime) showing a fibre texture close to {111}<uvw> [108]. Texture examination of warm rolling of B2 ordered polycrystalline Fe-28at.%Al-2at.%Cr and texture simulation showed a best correspondence between simulated and experimentally detected rolling textures for simulation based on <111>{011} and <111>{112} slip systems [76], supporting the present results.

For forging at high temperature (above 800°C), the deformation texture is similar to that of forging below 600°C. However whilst recrystallization occurred more evidently in the samples forged at 900°C and 1000°C as well as in the forged and annealed samples (800Q+A, 900SQ+A), the relative intensity $f_{\{hkl\}}$ of 800°C forged sample is taken as relative intensity of deformed structure since there is only a small amount of recrystallization. When $f_{\{111\}}$ and $f_{\{200\}}$ of the material forged at 800°C and that of the material forged at 400°C, 500°C and 600°C are compared, a subtle difference between $f_{\{200\}}$ of the material forged at 800°C and that of the material forged at low or moderate temperatures can be noted (fig. 4-28 (b)): $f_{\{111\}}$ stays very high and unchanged from 400Q to 800Q, while $f_{\{200\}}$ decreases from 400Q to 800Q (from about 10% to 5%) (while $f_{\{110\}}$ and $f_{\{211\}}$ are fairly stable in this regime). Such an observation can be understood by comparing the

simulated pole figures based on <111>{011} and <111>{112} slip systems and that based on the <100>{011} slip system (fig. 2-8) [77]: very strong {111} and very weak {110} are found in both cases, while a medium weak {200} is seen in the {100} pole figure generated based on <111>{011} and <111>{112} slip and near zero {200} in {100} pole figure generated based on the <100>{011} slip system. Then it can be deduced that the deformation texture upon forging at high temperature (above or at 800°C) was generated not by the <111>{011} and <111>{112} slip systems (which would show a strong {111} texture and a moderate to weak {200} texture) but by <100>{011} slip system (which would show a similarly strong {111} texture but not {200} texture). The simulation of forging texture based on <100>{001} showed that such a system did not result in significant grain rotations although it contributed to deformation to a certain extent. Texture examination on hot extrusion of Fe-40at.%Al and Fe-40at.%Al-0.1wt.%B B2 structured alloys (such extrusion must have been carried out at fairly high temperature) showed also a very strong {111} fibre which is identical to present texture evaluated by relative x-ray peak intensity[109].

The above discussion strongly suggests that the {111} texture is the deformation texture over a wide range of forging temperature for B2 ordered iron alumindes, generated by <111>{011} and <111>{112} operating systems at low or intermediate temperatures and by <100>{011} slip systems at high temperatures. As the temperature increases from low temperature (400°C) to high temperature (800°C) there is always a dominant {111} texture, but a gradual reduction in strength of the weak {200} texture component - it is this that reflects the change of deformation slip system. On the other hand, the dominant {200} texture was mainly produced by recrystallization process. As described in section 4.4, the result of selected area diffraction showed that most of the analysed subgrains in 800°C and 1000°C forged samples oriented to nearly [111] direction, occasionally to [101], [212], [331], etc., while most of the recrystallized grains orient to nearly [001] direction, occasionally near [101]. Although the deformed subgrains do not take exactly the [111] orientation referring to the forging axis, the deviation is only slight, most of the subgrains have a deviation within 2-3°. The orientations of these deformed subgrains do not change very much one from another since they are separated by low angle subgrain boundaries. As such it is confirmed again that the {111} texture is the major texture generated by forging.

5.3. Dislocation dominance and glide plane at various temperatures

In the preceding section, the forging texture and the recrystallization texture were discussed and evaluated based on the measurements of the relative intensities of x-ray diffraction peaks, indicating that forging texture is {111} generated by <111>{011} and <111>{112} slip systems at low temperature and <100>{011} slip system at high temperature, and the recrystallization texture is {002}. In this section, emphasis is put on microstructure analysis, i.e. dislocation examination and an effort will be made to correlate the dislocation analysis result to texture determination.

The slip systems in both Fe_3Al and FeAl alloy at low and high temperatures were investigated extensively in previous studies. Critical conclusions were obtained for Fe_3Al and FeAl alloys at low temperatures, indicating the deformation by <111> slip system , confirmed by both TEM examination [62, 80-82, 85, 110] and slip trace analysis [54, 55, 61]. At high temperatures, the incompatibility of the results has been noted: for Fe_3Al ordered alloy, slip trace analysis showed the <111>slip direction [55] while dislocation examination confirmed the deformation by <100> slip system[56]; for FeAl type alloy, most of the studies indicated that the deformation is controlled by <100> dislocations[56, 61, 62, 64, 84]. However, <111> slip system was also noted by TEM investigation[80] at high temperature. Thus, the key point is to shed light on the slip system at high temperature.

Kad and co-workers showed <111> dislocation dominance at high temperature in both Fe_3Al and FeAl and suggested that the <100> dislocations were formed during cooling after deformation, emphasising the importance of rapid cooling after deformation for the study of dislocation configurations[80]. Accordingly, the samples forged at various temperatures were cooled quickly after deformation in the present study to reduce the effect of prolonged exposure at high temperature and the low cooling rate on the possible dislocation reorganisation. At the same time, it is of great importance to correlate the dislocations present, crystalline orientation of analysed grains or subgrains and forging textures so as to identify the real slip system during deformation. The dislocation dominance at low and at high temperatures will be discussed separately as follows.

The summary of dislocation analyses of the materials forged at 400°C and 500°C in appendixes III and VII show that the <111> dislocations were dominant (87% for 400°C forging and 65% for 500°C forging) during deformation at low temperatures. Most of the <111> dislocations lay in the screw direction and the few non-screw dislocations that could be analysed showed that their glide planes were typically {011} planes but rarely {112} planes for the material forged at 400°C. At 500°C, there were fewer screw <111> dislocations than at 400°C with the non-screw dislocations again gliding both on {011} and {112} planes. The present results showed clearly that the deformation at low or intermediate temperatures of B2 ordered FeAl alloy at high strain rate is mainly attributed to <111> dislocations. The deformation textures generated by forging at 400°C and 500C° are similar to that obtained by texture simulation based on the <111>{011} and <111>{112} slip systems which were also observed in the present study, indicating the consistence of slip systems with the resultant deformation texture. That the majority of <111> dislocations lay in screw directions in a Fe-39.5Al deformed at room temperature was also noted by Yoshimi et al[62] and high density of <111> dislocations was observed by Yamagata [111]. Dipoles generated by double-cross slipping at room temperature was investigated by Baker and Horton using *in situ* observation[112]. Similar double cross-slip of screw <111> dislocations

from (001) onto (112) and back to (001) and dipole formation near temperature just below stress increasing regime were confirmed by Rösner and co-workers[113]. These features were also determined by other studies to be maintained to temperatures[63, 84, 114] in the region of anomalous increasing stress. Slip trace observations deduced the same result. Yamagata et al examined the slip traces of single crystals of FeAl submitted to compression from 77K to 473K and concluded that slip systems were <111>{011} and <111>{112} in all crystal orientations, occasionally <111>{123} at very low temperature (77K) [83]. Dislocation energy calculations and mobility evaluations also support the movement of <111> dislocations in B2 structured FeAl alloy (for Aluminium atomic percentage of 35%, 40% and 50%) [115]. A transition in slip directions from <111> to <100> was confirmed by both the slip trace examination and TEM observation in FeAl alloy at intermediate and high temperatures [84, 85]. Schröer et al conducted compression tests on a Fe70Al30 alloy and the results also showed <111>{011} and <111>{112} systems at intermediate temperatures[55]. In any case, a very small fraction of <100> dislocations was observed at 400°C (very few <110> dislocations in this case) and about one fifth of <100> dislocations was found at 500°C. The reason is that the slip at moderate temperatures is mixed type, thus both <111> and <100> slips exist in this transition temperature range[61]. In fact, the orientation of the crystal has an effect on the activation of a slip system[53, 84], and thus in different grains which have different orientations, the <111> and <100> dislocation fractions varied as shown by dislocation analyses in appendixes III and VII. In addition, the fraction of <100> at 500°C is higher than at 400°C, suggesting that slip direction starts to change in this temperature range, even at such a high strain rate.

Previous studies of dislocations in B2 ordered FeAl alloy showed similar results. At low temperatures there were mostly <111> dislocations[82, 107, 110] and at intermediate temperatures, a transition from <111> to <100> occurred[63, 64, 85, 88, 115, 116]. TEM observation of dislocation in Fe_3Al alloys[55, 56] demonstrated D03 superdislocations at low temperature and coexistence of 1/2a<111> superdislocations and <100> dislocations at moderate temperatures (partially or highly B2 ordered state), and the fraction of these two types of dislocations depended on both temperature and strain rate [91]. At higher temperature (600°C) and high strain rate, <111> dislocations were dominant while at very low strain rate at the same temperature, <100> was dominant. Therefore, the present results are consistent with previous studies in respect to slip systems in the FeAl alloy.

The selected area diffraction analysis of 800°C forged material showed that most deformed subgrains have an orientation near [111] direction, which is in agreement with x-ray diffraction examination, featuring a very strong {111} texture. The statistics of the dislocation analysis of the sample forged at 800°C shown in appendix VIII indicates that about 80% of the analysed dislocations in such deformed subgrains oriented near [111] are <100> type, gliding on {001} or

{011} planes, occasionally on {012} planes for some areas. The <110> dislocations make up generally about 10% of total analysed dislocations, gliding on principally on {001} and on {011} planes. As for <111> dislocations, they account for less than 10% of total dislocations and glide on mostly on {011} planes but rarely on {112} at such a high temperature. In some areas, no <111> dislocations at all were observed as shown in appendix XI. Such quantitative analysis results are well consistent with most previous investigations of B2 ordered FeAl alloys[64, 82, 85, 88, 107, 110, 115, 116] and B2 regime in Fe_3Al alloys[56, 91] but there is a discrepancy with the dislocation investigation in Fe_3Al and in FeAl alloys [80] (as discussed above).

In the recrystallized grains, the percentage of <100> dislocations changed very much from one grain to another, for example, in fig. 4-37, the <100> dislocations are only a very small fraction while <110> account for 83% of the dislocations present but in fig. 4-38, the <100> dislocations make up 79%, <110> types are 3% and <111> dislocations are 19% of the dislocations present. The reason is that the orientations of these recrystallized grains are different and the shear stress for these <100> dislocations relative to compression axis varies evidently, as a result of the difference in Schmid factor. For example, <100> slip direction on {001} planes could easily be activated in view of its [101] orientation (fig.4-38), hence, a very high Schmid factor (0.5), while the orientation of the recrystallized grain in fig. 4-37 is not favourable to the activation of cube slip on {001} planes. In any case, in these recrystallized grains, the dominant dislocations are not <111> ones but <100> ones.

The dislocation analysis of the material forged at 1000°C, summarised in appendix XIII, shows similar results to those of forging at 800°C for deformed subgrians orienting to [111] direction. Considering the x-ray diffraction examination and the TEM observation, again nearly all the deformed subgrains orient to near [111] direction. More than 80% of the dislocations are <100> type, mostly gliding on {001} and some of them gliding on {011} planes and occasionally on {012} planes. In addition, one [001] oriented subgrain was observed and analysed in which the proportion of <100> is smaller (69%) than that of {111} oriented subgrains and the ratio of <110> and <111> dislocations is higher (both are 15%) due to its unfavourable orientation for activating <100> dislocations.

Fig. 5-3 shows the arrangement of <100> dislocations in the subgrain shown in fig. 4-40 with the angle between these two groups of dislocations about 60° as discussed in 4.4.4. In fact, another group of <100> dislocations was found in this subgrain but is outside the area shown in this micrograph. It is clear that the movement of these three groups of <100> dislocations gliding on {001} planes did not result in any grain rotation which maintains its present orientation (whether such a {111} oriented subgrain held its [111] orientation from the beginning or was produced from

an original grain with different orientation by rotations caused by forging is not known). Fig. 5-4 shows the layout of <100> dislocations in another subgrain (fig. 4-42). The movement of these

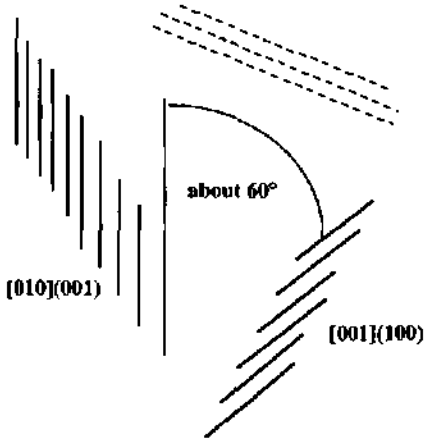

Fig. 5-3 Arrangement of dislocations in a [111] oriented subgrain of 1000°C forged material (shown in fig. 4-40)

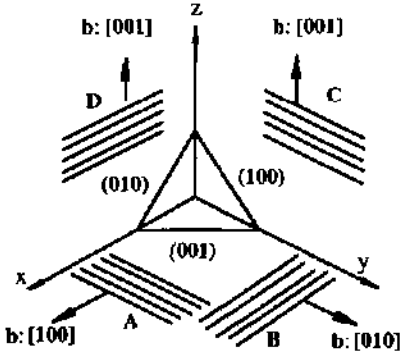

Fig. 5-4 Layout of dislocations in a [111] oriented subgrain of 1000°C forged material (shown in fig. 4-42)

four groups of dislocations maintain unchanged the present orientation of this subgrain during deformation. Such cube slip on {001} planes maintains the [111] orientation of such subgrains and

does not finally generate evident textures, as was indicated previously by texture simulation [77]. However, the original grains with other orientations e.g. <100>, <110>, <112>, etc. would turn finally to near <111> direction and consequently the strong {111} texture could be formed due to the operation of <100>{011} slip suggested by forging texture simulation.

It is also important to note that the ratio of [100]:[010]:[001] dislocations of various analysed areas in different thin foils is not near 1:1:1, suggesting that the <100> dislocations were not likely to have resulted from <111> dislocation decomposition. It seems reasonable to consider that any initial distribution of<111> dislocations would decompose to an approximately equal number of each variety of <100> dislocations. However, there are many long <100> dislocations in the deformed subgrains of 1000°C forged material.

To correlate the forging textures and dislocation configurations, it is clear that at low or intermediate temperatures (here 400°C and 500°C) the slip of <111> on {011} and {112} planes confirmed by dislocation analysis agrees very well with the textures evaluated in the present study. At high temperatures (at and above 800°C) the glide planes of <100> dislocations are mainly {001} and {011} types and <100>{011} slip systems resulted in a strong {111} texture by forging confirmed by texture simulation, while cube slip on {001} planes generated no evident grain rotation according to texture simulation [77]. So the dislocation configurations and the texture determination are well consistent with each other, suggesting that the deformation is attributed mainly to <111> slip at low temperatures and is dominated by cube slip at high temperature.

5.4. Activated state and movement of dislocations during high temperature deformation

The movement of dislocations in a perfect crystal commences when the shear force on the dislocation line overcomes the Peierls force. Subsequently the velocity of moving dislocations relies on the resolved shear stress acting on them[117]. Thus the resolved stress is a essential external factor affecting the dislocation movement for the given dislocations. Only those dislocations which have a favourable configuration can move easily. Shear stress for a given dislocation is expressed by $\tau=\tau_0\cos\alpha\cos\beta$, where τ_0 is the applied stress and $\cos\alpha\cos\beta$ is the Schmid factor, α and β were discussed in section 3.5.3. In this study, the Schmid factor was obtained for most of the analysed dislocations in different thin foils prepared from the materials forged at 400°C, 500°C, 800°C, and 1000°C and will be employed to explain the mobility of each type of dislocation under various conditions (crystalline orientation, temperature, recrystallized or unrecrystallized state).

Schmid factor or Schmid factor ratio SR was widely used to assess the favourable slip systems at different temperatures and to investigate the dependence of stress anomaly on such slips both by

slip trace analysis [54, 55, 61, 83, 84, 118] and by TEM examinations[64, 68, 81] in deformation of single crystals of FeAl or Fe_3Al alloys.

Dislocations in the material forged at 400°C have mostly <111> Burgers vector lying in screw directions. The few edge dislocations that can be analysed (since only for those can we determine the slip plane) have been shown to have a high Schmid factor, gliding generally on {011} planes and rarely on {112} planes. The screw dislocations, though it is difficult to identify the glide plane and Schmid factor due to zero angle between Burgers vector and dislocation line direction, are probably on the same glide planes. A certain plane is presumably selected according to its preferred crystallographic orientation with respect to the loading axis, and these screw <111> dislocations are considered to be the activated or mobile dislocations for this temperature. A very few <100> dislocations were also seen to have high or low Schmid factor gliding mainly on {011} planes. So it can be easily deduced that it is <111> dislocations that are responsible for deformation while <100> dislocations have very little effect on such deformation due to the very low fraction of such dislocations present.

At 500°C, the <111> dislocations in the material are also dominant in fraction but a little less so than that in the material forged at 400°C. Additionally, the proportion of screw <111> dislocations in all these type dislocations is smaller compared with that at 400°C. However, most of these non-screw dislocations have high Schmid factor. It is interesting to note that there are more non-screw <111> dislocations which glide on {112} planes at 500°C than at 400°C, suggesting that <111>{112} slip became more easy when the temperature was increased. Similar results have been noted in slip trace examination of FeAl single crystal, showing that at temperatures between 300K and 700K the slip system <111>{011} was found to be active as primary slip system whereas at higher temperatures the primary slip system changed to <111>{112}[54]. Slip trace analysis of Fe-30Al demonstrated a similar change at intermediate temperatures depending on the crystallographic orientation[55]. However, an investigation of slip traces on a FeAl single crystal did not reach the same conclusions[83], deducing that at very low temperature (77K) the <111>{112} slip system is active and at higher temperatures, <111>{011} became more active. The present results also show that the <100> dislocation fraction is higher at 500°C than that at 400°C (<110> dislocations also increased but less markedly so) and these <100> dislocations, gliding principally on {001} and {011} planes, have high, moderate as well as low Schmid factors depending on the crystallographic orientation.

In brief, the dislocation configuration and the calculated Schmid factor at 400°C and 500°C favour the activation of screw dislocations and <111>{011} and <111>{112} slip. A few <100> dislocations may also be activated depending on their glide plane and the grain orientation relating to the loading axis.

As discussed in 5.2., the orientation of most deformed subgrains in both the samples forged at 800°C and forged at 1000°C is near the [111] direction, in this case, cube dislocations gliding on {001} planes have a Schmid factor of m=0.33. However, there are some <100> dislocations gliding on {011} planes, occasionally on{012} planes having a higher Schmid factor, for example, m=0.45-0.47. Low Schmid factor, for example, m=0-0.15 was also found for a few <100> dislocations gliding on {011} or {012} planes with unfavourable combination of Burgers vector, glide plane and grain orientation. In any case, nearly all <100> dislocations observed have a high Schmid factor whereas most <110> and <111> dislocations in these deformed [111] oriented subgrains have low Schmid factor. This reflects the activation of these <100> dislocations during deformation at elevated temperature. Moreover, the ratio of the three variants of <100> dislocations possessing a high Schmid factor [100]:[010]:[001] is far from 1:1:1 in all analysed areas in various thin foils of the materials forged at 800°C and 1000°C and this demonstrates convincingly that these activated <100> dislocations probably did not result from <111> decomposition. Besides, in some subgrains, no <111> dislocations were observed, but instead, most dislocations are <100> type. Accordingly, <111> dislocation decomposition is not likely the source of the <100> dislocation and it is not <111> but <100> dislocations which dominate the deformation at high temperature. Additionally, the high Schmid factor (m=0.5) of long straight <100> dislocations in newly recrystallized grains, as shown in fig. 4-38, reflects the importance of glide of such dislocations with high Schmid factor. So the statistical results of calculations of Schmid factors of a large quantity of dislocations in several areas of different thin foils at high temperatures shows the activation of <100>{001} and <100>{011} systems and confirms that the cube slip dominates the high temperature deformation.

5.5. Interaction of dislocations

Dislocation decomposition or dislocation reactions were observed at low and high temperatures respectively in the present study. Dislocation interactions producing <100> or <110> from <111> were not found in the materials forged at 400°C and 500°C, while the glide dissociation of <111> dislocations to <100>+<110> was observed, for example, $[1\,\bar{1}\,1](011)\rightarrow[001](110)+[1\,\bar{1}\,0](110)$ in the material forged at 500°C. Here the $[1\,\bar{1}\,1]$ and [001] dislocations have high Schmid factors (0.41 and 0.47 respectively) while the $[1\,\bar{1}\,0]$ dislocation has a low Schmid factor (0.24), indicating that the further movement of these dislocations will be impeded by this $[1\,\bar{1}\,0]$ dislocation. It is the low Schmid factor for the glide of the <110> dislocation and the absence of any evidence of the glide of such dislocations at such temperature that confirms that the dislocation interaction involved is such a decomposition of <111> dislocations and not a combination of initial, gliding <100> and <110> dislocations. Similar decompositions were also seen in a Fe-40Al alloy deformed at 500 and at 512°C[64, 65]. However, dislocation interactions and dislocation decompositions were not frequently observed in low or intermediate forged materials.

In contrast, many dislocation interactions were observed and analysed in the high temperature forged samples (at 800°C and 1000°C). These interactions were typically <100> dislocations interacting to produce <110> ones. The resultant <110> dislocations have different glide planes and Schmid factors for various interactions. For example, for the interactions (both Burgers vectors and glide planes, and Schmid factors are indicated in the following interactions) [001](010)/0.33+ [010](001)/0.33 → [011](100)/0.47 and [100](011)/0.47+[001](010)/0.33 → [101](010)/0.33 in the material forged at 800°C, the cube dislocations and the *<011>* dislocations have high Schmid factor, suggesting that the <011> dislocations are mobile during deformation. The interaction of <100> dislocations to produce a $[\bar{1}01]$ dislocation lying in a screw direction was observed in the 1000°C forged condition and was analysed as shown in fig. 5-5. The crystallographic orientation of this subgrain is near [111] then both $[\bar{1}00]$ on (001) plane and [001] on a (100) (45° edge dislocation) have the same fairly high Schmid factor m=0.33, suggesting the high mobility of both these <100> dislocations. Such a dislocation reaction configuration makes it difficult for further movement to occur, however, because of the low Schmid factor of the $[\bar{1}01]$ product. Climb may possibly occur to allow limited movement of this junction dislocation.

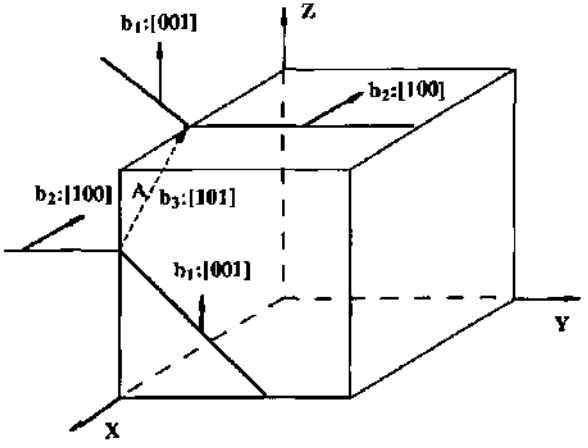

Fig. 5-5 Schematic illustration of a dislocation interaction observed in a [111] oriented subgrain in 1000°C forged material: $[\bar{1}00](001) + [001](100) \rightarrow [\bar{1}01](010)$. The line directions of the dislocations with the Burgers vector $\mathbf{b_1}$, $\mathbf{b_2}$ and $\mathbf{b_3}$ are $[0\bar{1}1]$, [010] and $[\bar{1}01]$ respectively

A $[0\bar{1}1]$ dislocation in a configuration where no shear stress was applied was found in the material forged at 1000°C and was shown to have been produced by the following dislocation reaction: $[001](100)/0.33+[0\bar{1}0](001)/0.33 \rightarrow [0\bar{1}1](100)/0$. Such a dislocation reaction will act as an obstacle to further deformation due to lack of shear stress on the $\{0\bar{1}1\}$ dislocation. <111>

decomposition resulting in <100> dislocations was not observed in the sample deformed at high temperatures even though there is a small fraction of <111> dislocations. On the other hand, <100> interactions to produce <110> dislocatinns suggest that the defomation at high temperature is attributed mostly to these <100> dislocations and they were not generated from <111> decompositinn nor <111> interactions.

The present results of dislocation reactions at high temperatures are not consistent with the previous investigation on dislocation configuration in B2 state of high temperature deformed Fe_3Al alloy[80], showing an example of <111> interaction to produce <100> dislocations and suggesting that the cube dislocations were rapidly exhausted at low strains. However, the dislocations seen both in highly deformed subgrains and newly recrystallized grains are mostly <100> type (in a few recrystallized grains, <110> dislocations are dominant) and neither <111> decomposition nor <111> reaction was observed at high temperatures but instead <100> glide and interaction to produce <110> dislocations were seen frequently. This result is supported by a study of flow stress in FeAl [116], suggesting that <111> and/or <110> dislocations may have been present as junction dislocations arising from reactions of the type: a[100]+a[010]→a[110] and a[110]+a[001]→a[111] which have been also noted in the related B2 NiAl alloy. According to the dislocation reaction analysis above, it can be concluded again that deformation is controlled by <111> slip at 400°C and 500°C and controlled by <100> slip at high temperatures (800°C and 1000°C) upon forging for B2 ordered FeAl alloy at high strain rates.

5.6 Some specific characteristics of moving dislocations at various temperatures

It is worthwhile to recall the specific configuration of dislocations at different temperatures briefly before examining the stress anomaly and the dependence of work hardening on temperature in the following section.

It is confirmed that most of the dislocations in the material forged at 400°C were <111> type lying generally in screw directions gliding mostly on {011} but rarely on {112}. There was no evidence of any climb, neither for screw nor for edge dislocations. Occasional long bowed <111> dislocations gliding on {011} planes with zero Schmid factor were seen (as shown in fig. 4-30). Such dislocations were bowed due to the presence of other pinning dislocations at their ends. Small jogs produced by dislocation interactions were observed and only few dislocation loops were seen at this temperature. At 500°C some subtle changes of <111> dislocations were noted: i) cross-slip of a partial <111> dislocations was seen on some occasions; ii) significant number of <111> dislocations gliding on {112} planes. In addition, a few loops and some concentric loops produced by the interaction of moving dislocations with the original loop were seen. Such cross-slip and dislocation loops were seen clearly in fig. 4-32 and fig. 4-33. Climbing of <111> dislocations

which is closely related to the increase of temperature and the increase of diffusivity[56, 68] was rarely seen at 500°C under the condition of high strain rate.

Dislocations in the materials forged at 800°C and 1000°C have similar characteristics but different from the 400-500°C dislocations. Both short and long curved <100> were seen in the two cases but more long curved <100> dislocations were observed at 1000°C than at 800°C . In addition the subgrain size at 1000°C was larger than that at 800°C. Planes such as {012} were often determined to be glide planes for <100> dislocations at such high temperatures in addition to {001} and {011} planes because the <100>{012} slip is favoured by crystallographic orientation of the applied stress and the high Schmid factor. The report on such slip has rarely been noted for deformation study of FeAl. Occasionally <110> dislocations were observed, with high Schmid factor, and were apparently mobile at these high temperatures. A very small number of <111> dislocation was also seen, but these contributed only very slightly to deformation.

5.7. Stress anomaly and dislocation configurations

The anomalous increases of stress at intermediate temperatures, that is the positive dependence of yield point on deformation temperature in iron aluminides over a wide range of Al concentration has drawn great attention over the last two decades and extensive studies have been carried out and several models have been proposed to explain such an interesting phenomenon as highlighted in several review papers[51, 65]. The stress anomaly was also noted in the present study and will be discussed based on the relevant models mentioned above and the results obtained such as dislocation configurations, textures and general microstructures.

5.7.1. Correspondence between flow stress and Burgers vector of dislocations at various temperatures

The dislocations found are mostly <111> at low and moderate temperatures and mostly <100> at high temperatures in deformed FeAl alloy as discussed in section 5.3. The curves of yield stress as a function of forging temperature in fig. 4-9 clearly shows a stress increasing from 400°C to 800°C and then a decrease in stress upon forging at higher temperatures. Similar transitions in slip direction with the appearance of the intermediate temperature stress peak were already reported in many studies on both Fe_3Al and FeAl alloys[18, 56, 61-63, 67, 84]. The transition in slip direction was explained by examining the critical resolved shear stress (C.R.S.S) for the <111>{011}, <100>{011}and <100>{001} systems, and showing that the C.R.S.S of <111>{011} decreased slowly as the temperature increased while the C.R.S.S of <100>{011}and <100>{001} decreased rapidly with increasing temperature[84], leading to the transition in slip direction at intermediate temperature when the C.R.S.S of <111>{011} becomes higher than that of <100>{001}. Additionally, the lower value of $\tau_{\langle 001\rangle\{010\}}$ than $\tau_{\langle \bar{1}10\rangle\{001\}}$ at high temperatures implies that <100>{001} slip is preferred to <100>{011} as confirmed by slip trace observation in the same

study. Mixed slip on <100>{001} and <100>{011} was also noted by Baker and co-workers [18] at the peak temperature and they suggested that the critical resolved shear stress for <111> was so high that other slip vectors become active and a transition occurred in glide direction from <111> to non-<111>, specifically, to a mixture of <100> and <110>. A similar result was obtained in the present work by the quantitative dislocation analysis which showed that more <100>{001} slip combinations than <001>{011} were found at the peak temperature (800°C) and at higher temperatures although <100>{011} slip makes an important contribution to the deformation texture at high temperatures. Yoshimi et al examined the relationship between dislocation structures and yield point at different temperatures in a B2 structured Fe-39.5Al alloy compressed at various temperatures (T1-the temperature where the yield stress begins to increase anomalously, Tp-the temperature where the stress peak appeared)[62]. Below T1 (room temperature in their study), the microstructure is characterised by completely long straight <111> screw dislocations. Below Tp and above T1, it was again <111> dislocations that dominate but most of them were not screws. Over Tp, bundles of tangled [010] dislocations were determined to lie along the [100] direction. Screw dislocations were also noted in Fe_3Al alloy deformed at 400°C for both low strain rate ($4x10^{-6}$ s^{-1}, all the dislocations were <111> type on {011} planes, mostly screws, few edges) and at relatively high strain rates ($4x10^{-3}$ s^{-1}, all the dislocations were <111> type and about half of them were screw types on {011} planes)[91].

The stress variation and transition in slip direction was also examined by slip trace observations by Yoshimi and co-workers on a B2 ordered FeAl alloy[61]. Below the peak temperatures (near 873K or 823K depending on the crystallographic orientation), <111> slip was dominant and it changed to <100> slip over the peak temperature. It is interesting to note that the slip direction at temperatures where the stress peak appeared was <100> for all crystallographic orientations, suggesting that <100> slip is responsible to deformation at the stress peak temperature. A critical result obtained in the present study, showed that <100> dislocations make up the majority, about 80%, of the total dislocations at 800°C where the peak in stress appeared.

5.7.2. Increases of stresses and changes of dislocation structures from 400°C to 500°C

It is of interest to compare the microstructures of materials forged at 400°C and at 500°C to explain the increasing stress over this temperature range. In the first place, most of the <111> dislocations were screw at 400°C while there were fewer screw <111> dislocations at 500°C. At the very onset of deformation, the screw <111> dislocations have the possibility to slip on several planes: {011} or {112}, depending on the crystallographic orientation of the applied stress for the particular Burgers vector. It may then be considered that the density of mobile <111> dislocations is higher at 400°C than at 500°C, leading to lower yield stress at 400°C than at 500°C.

The cross-slip of <111> dislocations is more evident at 500°C than in material forged at 400°C as pointed out in section 4.6, for example, the cross-slip of some [1 $\bar{1}$] variants onto (1 $\bar{1}$ 2) occurred during deformation and this is responsible for the increasing stress, as shown in the mechanical data of fig. 4-9. In fact, the cross-slip of superdislocation reduces the segment length of mobile dislocations, leading to increase of shear stress as described by

$$\tau=\frac{\mu b}{\lambda} \qquad (5\text{-}3)$$

where μ is the shear modulus, b is the Burgers vector and λ is the average segment length of mobile dislocations.

An investigation on the stress anomaly in Fe_3Al single crystal by Hanada[52] argued that the screw part of a superdislocation moving on the ($\bar{1}$01) plane cross slipped thermally onto the ($\bar{2}$11) plane on the twinning side or the ($\bar{1}$ $\bar{1}$2) on the anti-twinning side, thus the cross slipped part acted as a dragging point for the motion of the screw dislocation on the ($\bar{1}$01) plane, leading consequently to the stress increase. Detailed observation of dislocations in an Fe_3Al alloy deformed at various temperatures showed[56, 81] that cross-slip became more and more evident above ambient temperature and the stress increase at intermediate temperature regime was also closely associated with the locking of <111> dislocations as a result of climb to a plane nearly perpendicular to the Burgers vector. Similar climb dissociated configuration of some <111> dislocations was also identified in a B2 Fe-39.5Al alloy[62]. It was believed that the meandering, fairly short [111] superdislocations strayed off the operative ($\bar{1}$01) plane frequently during deformation slightly below the peak temperature.

Another aspect to which attention should be paid is the dislocations loops generated by cross-slip and further movement of dislocations as discussed in section 5.6. More dislocation loops were noted in the present work in the material forged at 500°C than at 400°C. The loops may act as a dislocation obstacle, leading to stress increase, as shown in fig. 4-32 by the interaction of a bowed [111] dislocation (dislocation 51) with a loop. Further movement of such dislocation may leave another loop around the original one leading to the formation of concentric loops as shown in the same fig. 4-32 and 4-33. Fine loops were also observed in a Fe-43Al alloy and they were considered to produce significant hardening[119].

In addition, a few dislocation decompositions of <111> to <110> and <100> were noted in the 500°C forged condition. For example, a [1 $\bar{1}$] dislocation gliding on a (011) plane with Schmid factor 0.41 decomposed to a [1 $\bar{1}$ 0] dislocation gliding on a (110) plane with Schmid factor 0.17 and a [001] dislocation gliding equally on the (110) plane with Schmid factor 0.47. The low Schmid factor of the newly generated [1 $\bar{1}$ 0] dislocation may imply its low mobility and such decomposed dislocations may lead to dragging of the other two dislocations, giving rise to a stress

increase. It seems, based on the discussion above, that the increasing stress in this temperature regime may correlate to several mechanisms instead of only one mechanism during deformation at the high strain rate used in the present study.

Just as the fraction of <111> dislocations after forging at 500°C is lower than after forging at 400°C, it can be expected that this fraction may become lower at 600° and 700°C leading eventually to the transition from <111> slip to <100> as the temperature increases. In the present study, the peak in stress at 800°C takes place when <111> dislocations are no longer predominant as seen by examining fig. 4-9. Previous studies by slip trace analysis of FeAl single crystal deformed at different temperatures showed that the peak stress corresponded to <100> slip for various orientations[61]. Dislocation examinations in another study also indicated the correspondence between peak in stress and predominant <100> dislocations[116]. The following evolution of structure with temperature seems possible: i) the number of screw <111> dislocations decreases with increasing temperature, leading to a lower density of readily mobile dislocations; ii) at higher temperatures, thermally activated cross-slip becomes more evident and leads to the decrease of average segment length of mobile superdislocations; iii) more obstacles such as glide-produced small loops may also exist; iv) the critical resolved shear stress of <100> dislocations reaches a level where it is lower than that of <111> dislocations, and thereafter the flow stress falls. Thus it is reasonable to expect a range of increasing stress with temperature and a peak in stress at some temperature.

5.7.3. Variation of work hardening rate as a function of temperature

It is interesting to note that the work hardening index or work hardening rate shown in figs. 4-12 and 4-13 decreases almost linearly from 400°C to 800°C while the yield point increases from 400°C to 800°C. In other words, the yield point and work hardening rate have an opposite dependence on forging temperatures between 400°C and 800°C. The variation of maximum stress as a function of the forging temperature shown in fig. 4-10 demonstrates also a near linear negative dependence on forging temperature (note that the stress measured at the maximum strain on forging at 400°C was not a true maximum but simply the highest stress at the point where forging was halted). The anomalous stress increasing from 400°C to 800°C was discussed in section 5.7.2 and the negative dependence of work hardening rate on forging temperature is discussed here.

Work hardening of ordered alloys was studied and shown to be correlated with deformation by superdislocations[120-122]. An investigation on work hardening of fully-ordered Cu_3Au showed very high densities of superlattice screw dislocations which had cross-slipped onto {100} and which were believed responsible for the rapid Stage II hardening since they induce other dislocations gliding on the primary slip plane to cross-slip and remove them from subsequent glide[122]. Davies and Stoloff had reached a similar conclusion on examining the work hardening

of Cu_3Al single crystal, indicating that the increase of work hardening due to ordering in the alloy studied arises from a source exhaustion mechanism; dislocations from a source cannot move large distances before being held up at barriers formed by partial cross slip of superdislocations[120]. In addition, a study of tensile behaviour upon ordering of Ni_3Fe single crystals showed that the ordered specimens work-hardened more rapidly than the disordered ones, implying that the superdislocations (complex dislocations) were responsible for the higher work hardening rate while the perfect dislocations in the disordered state led to lower work hardening rate[121]. These studies suggest that superdislocations may result in higher work hardening rate than perfect or simple dislocations.

In the present study, the fraction of the <111> superdislocations and the work hardening rate decrease with increasing deformation temperature. If we assume also that the work hardening rate when deformation is controlled by <111> superdislocations is higher than when it is controlled by <100> perfect dislocations, it is possible also to explain the decreasing work hardening rate with increasing forging temperature by the decreasing fraction of <111> dislocations on forging at higher temperatures. Thus the work hardening rate may be considered as being composed of two components:

$$\theta=\theta_{<111>}+\theta_{<100>} \qquad (5\text{-}4)$$

where $\theta_{<111>}$ and $\theta_{<100>}$ are contributions of <111> and <100> dislocations to work hardening rate (the component of <110> dislocations $\theta_{<110>}$ is neglected in view of the small fraction of such dislocations which are present). According to the previous discussion $\theta_{<111>}>>\theta_{<100>}$ and this can perhaps simplify equation (5-4) as $\theta= f_{<111>}\cdot\theta_{<111>}$. Therefore, the higher the <111> dislocation fraction, the higher the work hardening rate, and this can shed useful light on the transition from <111> to <100> slip system with increasing deformation temperature. Such an explanation needs a detailed examination of the work hardening mechanisms of B2 ordered FeAl when <111> and <100> dislocations operate respectively, as well as the temperature dependence of each mechanism, and the interaction of work hardening mechanisms (that is, for example, the role that <111> dislocations play in modifying $\theta_{<100>}$) and this discussion cannot be developed further at the present time.

5.7.4. Mechanical behaviour at different strain rates

The comparison in fig. 4-9 shows clearly that the data obtained by forging were shifted to higher temperature by the higher strain rate while the values of peak in stress in the two cases did not vary significantly. Therefore, the slope of the stress-temperature curve in the rising stress stage is smaller than for compression. The shift of the curve at high strain rate to higher temperature may be associated with thermally activated locking mechanism, in other words, there is less time for locking at high strain rate than at low strain rate when the temperature is the same, whether the locking mechanism responsible for the stress increase is climb, cross slip, or any other pinning

mechanism. This conclusion would seem, however, to eliminate the vacancy hardening model of strengthening.

Nevertheless, the sensitivity of peak stress to strain rate shows some incompatibilities in different works. The studies of the yield stress anomaly in B2 ordered Fe-40Al and Fe-39.5Al alloys showed certain increases in peak stress at high strain rate compared with low strain rate[61, 67], while an investigation of yield stress in Fe_3Al showed only a very small change of peak stress as a function of strain rate[91]. The present work shows no significant increase of peak stress when the strain rate changed from 4×10^{-4} s^{-1} to 1^{-1}, while the shift of peak temperature is significant and may be related to the thermally activated process controlling the movement of dislocations. Considering the extent of stress rise (locking $\Delta\sigma^{+}$)as a function of deformation temperature:

$$\Delta\sigma^{+}=A\exp(-Q_b/RT)\cdot\dot{\varepsilon}^{-n} \qquad (5\text{-}5)$$

where A is a constant, Q_b the activation energy of the locking process, R and T the gas constant and the temperature, $\dot{\varepsilon}$ is the defromation rate, and n a positive constant. It is clear that higher strain rates will reduce the stress increase at a given temperature, and tend to push the anomalous peak temperature to a higher value. It is not possible to deduce further, however, from the present results what precise pinning processes are involved.

Conclusions

6. Conclusions

High strain rate, large strain deformation was performed at various temperatures (400°C to 1000°C) on a *Fe-41Al-2Cr alloy by forging and rapid quenching. Slow quenching after forging* and subsequent annealing was employed to investigate the final structure and its sensitivity to such annealing. Measurement of mechanical properties such as yield point, maximum stress, work hardening parameters, microstructure examination by optical and by SEM observation, texture evaluation by x-ray diffraction based on the relative intensity of different reflections, dislocation analysis and TEM determination of Burgers vector, line direction, glide plane and Schmid factor as well as crystallographic orientation determination of deformed grains or subgrains, were all carried out. The results of microstructure and macrostructure as well as mechanical behaviour during deformation at low, intermediate and high temperatures were discussed and the following conclusions have been drawn:

1) Fast deformation by forging from 400°C to 600°C resulted in very limited recovery and no recrystallization due to the relatively low temperatures, while some recovery was distinguished after forging at 700°C. At higher temperatures from 800°C to 1000°C, both recovery and recrystallization occurred because of high thermal activation at such temperatures. Annealing greatly changed the deformed microstructure after large deformation, but hardly changed the deformed microstructure after only a fairly small deformation. The recrystallized fraction and recrystallized grain size increase with increasing forging temperature. The holding time before quenching after forging at high temperature enhanced further recrystallization enormously, confirming that rapid quenching after forging is extremely important to retain the deformed microstructure from high temperature to room temperature. Forging can significantly refine the microstructure when parameters such as forging temperature, deformation, cooling rate after forging, etc., are well combined.

2) The relative intensity of x-ray diffraction reflections was used to evaluate the forging and recrystallization textures, and it proved to be able to describe fairly precisely the textures obtained. The analysis of relative intensity of x-ray diffraction reflections, the examination of deformed microstructure as well as the orientation determination of a large number of deformed subgrains and recrystallized grains in various conditions by TEM diffraction were very well consistent and showed that the dominant forging texture is {111} at both high and low forging temperatures and the recrystallization texture after forging at high temperature or after forging plus annealing is {200}. The results of texture evaluation by x-ray relative intensity conformed very well to simulated textures based on different operating systems: <11>{01} or <111>{112} at low forging temperatures, both generating very strong {111} texture and a rather weak {002} texture, <100>{011} at high forging temperatures generating a strong {111} texture and a significantly weaker {002} reflection.

3) A large quantity of dislocations in different areas of various thin foils prepared from the materials forged at 400°C, 500°C, 800°C and 1000°C was analysed to determine Burgers vector, dislocation line direction, glide plane as well as Schmid factor with respect to the forging axis. The results showed that most of the analysed dislocations were <111> type at low or intermediate temperatures and many of them were screw ones; the others were edge or mixed type gliding on {011} and {112} planes with high Schmid factor. There were more screw <111> dislocations at 400°C than at 500°C while there were more dislocations gliding on {112} planes at 500°C than at 400°C. At higher (above 800°C) temperatures, most dislocations were <100> type, gliding on {001} and {011} planes, occasionally on {012} planes and generally showing a high Schmid factor.

The reaction of <111> dislocations to produce non-<111> dislocations was only rarely seen at intermediate temperature where the deformation was dominated by <111> dislocations. At the same time, occasional glide decomposition of <111> to generate <100> and <110> dislocations was observed. At high forging temperatures, many dislocation interactions of <100> to produce <110> dislocations were identified and some of the resultant <110> dislocations were mobile and others were not, based on the analysis of their Schmid factor.

The ratio of the three variants of <100> dislocation: [100]:[010]:[001] and the ratio of these three variants with high Schmid factor both in deformed subgrains and in recrystallized grains were not near 1:1:1, suggesting that the <100> dislocations did not likely generate from <111> decomposition or <111> reactions. The dislocation configuration at 800°C and at 1000°C exhibited similar characteristics. The coincidence of the texture evaluation and the statistical analysis of dislocations confirms that the deformation systems during forging changed from low temperature to high temperature; the deformation was controlled by <111>{011> and <111>{112] slip at low and intermediate temperatures and by <100>{001} and <100>{011} at high temperatures.

4) Slip transition from intermediate temperature to high temperature was identified by both texture examination and dislocation analysis and this transition occurred over a wide range of temperature, not at one specific temperature. Neither the <111> dislocations at low and intermediate temperatures nor <100> dislocations at high temperatures were the unique type of dislocation present but instead a mixture of both types was observed over a wide temperature range.

5) A peak in 0.2% flow stress was observed at 800°C upon forging and this peak was a broad one, spread over a wide temperature range at the high strain rate of forging. Locking of superdislocations (either by cross-slip or by climb at higher temperatures) had insufficient time to occur at high strain rate when the deformation temperature was relatively low, thus the stress increase caused by such locking was less important, and as a result, the slope of the yield point-temperature curve in the temperature regime of increasing stress was lower. The value of the peak

stress obtained during forging had a similar magnitude to that obtained by compression at low strain rates.

6) Work hardening rate showed a negative dependence on forging temperature due to two factors: i) work hardening rate is lower at higher temperature attributed to thermal relaxation mechanisms; ii) it is assumed that <111> dislocations produce a higher work hardening rate than <100> ones, and hence, the higher fraction of <111> dislocations formed at lower temperatures corresponds to a higher work hardening rate.

Appendices

Appendix I Dislocation analysis of an area in the material forged at 400°C shown in fig. 4-29. Orientation of analysed grain: near [011].

d \ g	$\bar{1}10$	$\bar{1}01$	$0\bar{1}1$	110	020	b	u	p	m
1	i	v	v	v	v	$[11\bar{1}]$	[001]	$(\bar{1}10)$	0
2	v	v	i	i	v	$[\bar{1}11]$	$[\bar{1}11]$	screw	
3	v	v	i	i	v	$[\bar{1}11]$	$[2\bar{3}1]$	(211)	0.47
4	v	v	i	i	v	$[\bar{1}11]$	$[\bar{1}11]$	screw	
5	v	v	i	i	v	$[\bar{1}11]$	$[\bar{1}11]$	screw	
6	v	v	i	i	v	$[\bar{1}11]$	$[\bar{1}11]$	screw	
7	i	v	v	v	v	$[11\bar{1}]$	$[\bar{1}10]$	(110)	0
8	v	v	i	i	v	$[\bar{1}11]$	$[\bar{1}11]$	screw	
9	v	v	i	i	v	$[\bar{1}11]$	$[\bar{1}11]$	screw	
10	v	v	i	i	v	$[\bar{1}11]$	$[\bar{1}11]$	screw	
11	v	v	v	v	v	$[11\bar{1}]$			
12	v	v	i	i	v	$[\bar{1}11]$	$[\bar{1}11]$	screw	
13	v	i	v	v	v	[010]	$[\bar{1}22]$	(201)	0.22
14	i	v	v	v	v	$[11\bar{1}]$	[001]	(110)	0
15	i	v	v	i	i	[001]	[001]	screw	
16	v	i	v	v	v	[010]	$[\bar{1}22]$	(201)	0.22
17	v	v	i	i	v	[111]			
18	v	v	i	i	v	$[\bar{1}11]$	$[\bar{3}31]$	(110)	0.41
19	v	v	i	i	v	$[\bar{1}11]$	[100]	$(0\bar{1}1)$	0
20	v	v	i	i	v	[111]			
21	v	v	i	i	v	$[\bar{1}11]$	$[\bar{3}13]$	(101)	0.41
22	v	v	i	i	v	$[\bar{1}11]$	[010]	(101)	0.41
23	i	v	v	v	v	$[11\bar{1}]$	[010]	(101)	0
24	v	v	i	i	v	$[\bar{1}11]$	$[\bar{1}11]$	screw	
25	v	v	i	i	v	$[\bar{1}11]$	$[\bar{1}11]$	screw	
26	v	i	v	v	v	[010]	$[\bar{1}11]$	(101)	0.35
27	v	i	v	v	v	[010]	[011]	(001)	0
28	v	v	i	i	v	$[\bar{1}11]$	$[\bar{1}11]$	screw	
29	v	v	i	i	v	$[\bar{1}11]$	[010]	(101)	0.41
30	v	v	i	i	v	$[\bar{1}11]$	$[\bar{1}11]$	screw	
31	v	v	i	i	v	$[\bar{1}11]$	$[\bar{1}11]$	screw	
32	v	v	i	i	v	$[\bar{1}11]$			

Appendix I continued

33	v	v	i	i	v	$[\bar{1}11]$	$[\bar{1}11]$	screw	
34	v	v	i	i	v	$[\bar{1}11]$	[111]	$(0\bar{1}1)$	0
35	v	v	i	i	v	$[\bar{1}11]$	$[\bar{3}12]$	$(1\bar{1}2)$	0.24
36	i	v	v	v	v	$[11\bar{1}]$	$[\bar{1}31]$	(101)	0
37	v	v	i	i	v	$[\bar{1}11]$	$[\bar{1}11]$	screw	
38	i	v	v	v	v	$[11\bar{1}]$	[001]	$(\bar{1}10)$	0
39	i	v	v	v	v	$[11\bar{1}]$	$]11\bar{1}[$	screw	
40	i	v	v	v	v	$[11\bar{1}]$	$[\bar{1}01]$	(101)	0
41	v	v	i	i	v	$[\bar{1}11]$	[211]	$(0\bar{1}1)$	0
42	i	v	v	v	v	$[11\bar{1}]$	[001]	$(\bar{1}10)$	0
43	i	v	v	v	v	$[11\bar{1}]$	[001]	$(\bar{1}10)$	0

Note: d-dislocations, g-imaging vector, b-Burgers vector, u-dislocation line direction, p-glide plane, m-Schmid factor.

Appendix II Dislocation analysis of third thin foil of the material forged at 400°C. Orientation of analysed grain: near [011].

d	g 0$\bar{1}$1	10$\bar{1}$	1$\bar{1}$0	002	200	b	u	p	m
1	v	v	i	v	v	[11$\bar{1}$]	[$\bar{2}$12]	(101)	0
2	v	v	i	v	v	[11$\bar{1}$]	[11$\bar{1}$]	screw	
3	v	v	i	v	v	[11$\bar{1}$]	[11$\bar{1}$]	screw	
4	v	v	i	v	v	[11$\bar{1}$]	[$\bar{2}$12]	(101)	0
5	v	v	i	v	v	[11$\bar{1}$]	[11$\bar{1}$]	screw	
6	v	v	i	v	v	[11$\bar{1}$]	[11$\bar{1}$]	screw	
7	v	v	i	v	v	[11$\bar{1}$]	[11$\bar{1}$]	screw	
8	v	v	i	v	v	[11$\bar{1}$]	[010]	(101)	0
9	i	v	v	v	v	[$\bar{1}$11]	[$\bar{1}$11]	screw	
10	i	v	v	v	v	[$\bar{1}$11]	[$\bar{1}$11]	screw	
11	i	v	v	v	v	[$\bar{1}$11]	[$\bar{1}$11]	screw	
12	v	v	i	v	v	[11$\bar{1}$]	[11$\bar{1}$]	screw	
13	v	v	i	v	v	[11$\bar{1}$]	[11$\bar{1}$]	screw	
14	v	v	i	v	v	[11$\bar{1}$]	[11$\bar{1}$]	screw	
15	v	v	i	v	v	[11$\bar{1}$]	[11$\bar{1}$]	screw	
16	i	v	v	v	v	[$\bar{1}$11]	[$\bar{1}$11]	screw	
17	v	v	i	v	v	[11$\bar{1}$]			
18	v	v	i	v	v	[11$\bar{1}$]			
19	v	v	i	i	v	[110]	[113]	($\bar{1}$10)	0.25
20	v	v	i	v	v	[11$\bar{1}$]			

Appendix III Summary of dislocation analysis on three thin foils of the material forged at 400°C

1	proportion of <100>:<110>:<111>		5 : 0 : 38	5 : 0 : 14	0 : 1 : 19
2	percentage of {100}		0%	0%	0%
3	percentage of {010}		9%	0%	0%
4	percentage of {001}		2%	26%	0%
5	percentage of <110>		0%	0%	5%
6	percentage of {111}		5%	0%	0%
7	percentage of {111}		58%	5%	0%
8	percentage of {111}		0%	58%	0%
9	percentage of {111}		26%	11%	65%
10	analysed thin foil		1st thin foil	2nd thin foil	3rd thin foil
11	orientation of analysed grain		[01]	[111]	[011]
12	characteristic of analysed grain		non-recrystallised	non-recrystallised	non-recrystallised
13	number of total dislocations		43	19	20
14	{100}	percentage with high m	0%	0%	0%
15		percentage with low m	0%	0%	0%
16	{010}	percentage with high m	50%	0%	0%
17		percentage with low m	50%	0%	0%
18	{001}	percentage with high m	100%	100%	0%
19		percentage with low m	0%	0%	0%
20	{111}	percentage with high m	/	0%	0%
21		percentage with low m	/	0%	0%
22	{111}	percentage with high m	80%	100%	100%
23		percentage with low m	16%	0%	0%
24	{111}	percentage with high m	0%	100%	0%
25		percentage with low m	0%	0%	0%
26	{111}	percentage with high m	0%	100%	60%
27		percentage with low m	91%	0%	20%
28	<100>	percentage with high m	60%	100%	0%
29		percentage with low m	40%	0%	0%
30	<110>	percentage with high m	0%	0%	0%
31		percentage with low m	0%	0%	100%
32	<111>	percentage with high m	79%	100%	68%
33		percentage with low m	11%	0%	16%
34	proportion of [100]:[010]:[001]				
35	with high Schmid factor, m		0 : 2 : 1	0 : 0 : 5	0 : 0 : 0
36	comments		<111> dominate	<111> dominate	<111> dominate

Note: **Line 1** shows the proportion of three types of dislocations <100>, <110> and <111>.

Lines 2-4, line 5 and lines 6-9 indicate the percentages of three variants of <100> dislocations of the total dislocations analysed, the percentage of <110> dislocations of the total dislocations and the percentages of four variants of <111> dislocations of the total dislocations, respectively.

Line 14 and line 15 show the percentages of {100} dislocations with high and with low Schmid factor of the total {100} dislocations analysed. **Lines 16-19** have the similar meaning.

Line 20 and line 21 show the percentages of {111} variant with high and with low Schmid factor of the total {111} dislocations. **Lines 22-27** have the similar meaning.

Lines 28-33 show the percentages of three types of dislocations <100>, <110> and <111> with high and with low Schmid factor of the total dislocations of each type.

Lines 34-35 show the proportion of three <100> variants with high Schmid factor.

Appendix IV Dislocation analysis of an area of the material forged at 500°C as shown in fig. 4-32. Orientation of analysed grain: near [001].

d	g 020	200	$\bar{1}10$	110	$0\bar{1}1$	b	u	p	m
1	v	v	i	v	i	[111]	[111]	screw	
2	v	v	v	i	i	[$\bar{1}$11]	[$\bar{1}$11]	screw	
3	v	v	v	i	i	[$\bar{1}$11]	[$\bar{1}$11]	screw	
4	v	v	i	v	i	[111]	[111]	screw	
5	i	v	v	v	i	[100]	[001]	(010)	0
6	i	v	v	v	i	[100]	[$\bar{1}$10]	(001)	0
7	v	v	i	v	i	[111]	[111]	screw	
8	v	v	i	v	i	[111]	[010]	($\bar{1}$01)	0.41
9	v	v	i	v	i	[111]	[010]	($\bar{1}$01)	0.41
10	v	v	v	i	i	[$\bar{1}$11]	[$\bar{1}$11]	screw	
11	v	v	i	v	i	[111]	[111]	screw	
12	v	v	v	i	i	[$\bar{1}$11]	[$\bar{1}$11]	screw	
13	v	v	v	i	i	[$\bar{1}$11]	[$\bar{1}$11]	screw	
14	v	v	v	i	i	[$\bar{1}$11]	[$\bar{1}$11]	screw	
15	v	v	v	i	i	[$\bar{1}$11]	[$\bar{1}$11]	screw	
16	i	v	v	v	i	[100]	[$\bar{3}$01]	(010)	0
17	v	v	v	i	i	[$\bar{1}$11]	[$\bar{1}$11]	screw	
18	v	v	i	v	i	[111]	[111]	screw	
19	v	v	i	v	i	[111]	[100]	($0\bar{1}$1)	0.41
20	v	v	i	v	i	[111]	[211]	($0\bar{1}$1)	0.41
21	i	v	v	v	i	[100]	[310]	(001)	0
22	v	v	i	v	i	[111]			
23	v	v	v	i	i	[$\bar{1}$11]	[$\bar{1}$11]	screw	
24	v	v	v	i	i	[$\bar{1}$11]	[001]	(110)	0
25	i	v	v	v	i	[100]	[001]	(010)	0
26	i	v	v	i	i	[100]	[001]	(010)	0
27	i	v	v	i	i	[100]	[001]	(010)	0
28	i	v	v	i	i	[100]	[001]	(010)	0
29	v	v	v	i	i	[$\bar{1}$11]	[001]	(110)	0
30	v	v	i	v	i	[111]	[100]	(011)	0.41
31	v	v	i	v	i	[111]	[100]	($0\bar{1}$1)	0.41
32	v	v	v	i	i	[$\bar{1}$11]	[$\bar{1}$11]	screw	
33	v	v	v	i	i	[$\bar{1}$11]	[$\bar{1}$11]	screw	
34	v	v	v	i	i	[$\bar{1}$11]	[101]	(12$\bar{1}$)	0.24

Appendix IV continued

35	v	v	v	i	i	$[\bar{1}11]$	[101]	$(12\bar{1})$	0.24
36	v	v	v	i	i	$[\bar{1}11]$	[100]	$(0\bar{1}1)$	0.41
37	v	v	v	i	i	$[\bar{1}11]$	$[\bar{1}11]$	screw	
38	v	i	v	v	i	(011)	[001]	(100)	0
39	i	v	v	v	i	[100]	$[11\bar{1}$	(011)	0
40	i	v	v	v	i	[100]	$]11\bar{1})$	(011)	0
41	v	v	i	v	i	[111]			
42	v	v	i	v	i	[111]	[111]	screw	
43	v	v	i	v	i	[111]	[010]	$(\bar{1}01)$	0.41
44	i	v	v	v	i	[100]	[011]	$(0\bar{1}1)$	0
45	v	v	v	i	i	{111}			
46	i	i	i	i	v	[001]			
47	i	i	i	i	v	[001]			
48	i	i	i	i	v	[001]			
49	i	i	i	i	v	[001]			
50	i	i	i	i	v	[001]			
51	v	v	v	i	i	$[\bar{1}11]$			

Appendix V Dislocation analyis of another area in the same thin foil of the material forged at 500°C as that of fig. 4-33. Orientation of analysed grain: near [2$\bar{1}$2].

d	g $\bar{1}$10	$\bar{1}$01	01$\bar{1}$	200	002	020	b	u	p	m
1	v	v	v	v	i	v	[$\bar{1}$10]	[$\bar{1}$11]	(110)	0.16
2	v	i	v	v	v	v	[1$\bar{1}$1]	[1$\bar{1}$1]	screw	
3	v	i	v	v	v	v	[1$\bar{1}$1]	[1$\bar{1}$1]	screw	
4	i	v	v	i	v	i	[001]	[$\bar{1}$11]	(110)	0.47
5	v	v	i	v	v	v	[$\bar{1}$11]	[$\bar{1}$11]	screw	
6	v	v	i	v	v	v	[$\bar{1}$11]	[$\bar{1}$11]	screw	
7	i	v	v	i	v	i	[001]	[111]	(110)	0.47
8	v	i	v	v	v	v	[1$\bar{1}$1]	[1$\bar{1}$1]	screw	
9	v	v	v	v	i	v	[1$\bar{1}$0]	[$\bar{1}$12]	(110)	0.17
10	v	i	v	v	v	v	[1$\bar{1}$1]	[2$\bar{1}$1]	(011)	0.41
11	i	v	v	i	v	i	[001]	[1$\bar{1}$1]	(110)	0.47
12	v	i	v	v	v	v	[1$\bar{1}$1]	[3$\bar{1}$2]	($\bar{1}$12)	0.24
13	v	v	i	v	v	v	[$\bar{1}$11]	[$\bar{2}$12]	(101)	0.18
14	v	v	i	v	v	v	[$\bar{1}$11]	[$\bar{1}$11]	screw	
15	v	i	v	v	v	v	[1$\bar{1}$1]	[1$\bar{1}$1]	screw	
16	v	i	v	v	v	v	[1$\bar{1}$1]	[3$\bar{1}$2]	($\bar{1}$12)	0.24
17	v	v	i	v	v	v	[$\bar{1}$11]	[001]	(110)	0.14
18	v	v	i	v	v	v	[$\bar{1}$11]	[$\bar{1}$11]	screw	
19	v	v	i	v	v	v	[$\bar{1}$11]	[101]	(12$\bar{1}$)	0.05
20	v	v	i	v	v	v	[$\bar{1}$11]	[$\bar{1}$1$\bar{1}$]	(101)	0.18
21	v	i	v	v	v	v	[1$\bar{1}$1]	[1$\bar{1}$1]	screw	
22	v	v	i	v	v	v	[$\bar{1}$11]	[1$\bar{1}$3]	(110)	0.14
23	v	i	v	v	v	v	[1$\bar{1}$1]	[1$\bar{1}$1]	screw	
24	v	v	i	v	v	v	[$\bar{1}$11]	[$\bar{1}$11]	screw	
25	v	v	i	i	v	v	[011]	[$\bar{1}$11]	(0$\bar{1}$1)	0.17
26	i	v	v	i	v	i	[001]	[2$\bar{2}$1]	(110)	0.47
27	v	v	i	v	v	v	[$\bar{1}$11]	[$\bar{1}$11]	screw	
28	v	v	i	v	v	v	[1$\bar{1}$1]	[1$\bar{1}$1]	screw	
29	v	i	v	v	v	v	[1$\bar{1}$1]	[1$\bar{1}$1]	screw	
30	v	i	v	v	v	v	[1$\bar{1}$1]	[1$\bar{1}$1]	screw	
31	v	i	v	v	v	v	[1$\bar{1}$1]	[1$\bar{1}$1]	screw	
32	v	i	v	v	v	v	[1$\bar{1}$1]	[1$\bar{1}$1]	screw	
33	v	i	v	v	v	v	[1$\bar{1}$1]	[$\bar{1}$11]	(110)	0.41

Appendix V continued

34	v	i	v	v	v	v	[1 $\bar{1}$ 1]	[1 $\bar{1}$ 1]	screw	
35	v	i	v	i	i	v	[010]	[1 $\bar{1}$ 1]	($\bar{1}$01)	0
36	i	v	v	i	v	i	[001]	[$\bar{1}$11]	(110)	0.47
37	v	i	v	i	i	v	[010]	[1 $\bar{1}$ 1]	(101)	0
38	v	v	i	v	v	v	[$\bar{1}$11]	[$\bar{1}$11]	screw	
39	v	i	v	v	v	v	[1 $\bar{1}$ 1]	[1 $\bar{1}$ 1]	screw	
40	v	v	v	v	i	v	[$\bar{1}$11]	[11 $\bar{1}$]	(101)	0.18
41	i	v	v	i	v	i	[001]	[2 $\bar{2}$ 1]	(110)	0.47
42	i	v	v	i	v	i	[001]	[$\bar{3}$31]	(110)	0.47
43	v	i	v	v	v	v	[1 $\bar{1}$ 1]	[1 $\bar{1}$ 1]	screw	
44	v	i	v	v	v	v	[1 $\bar{1}$ 1]	[$\bar{3}$31]	(110)	0.41
45	v	v	v	v	i	v	[$\bar{1}$10]	[$\bar{1}$11]	(110)	0.17
46	v	v	i	v	v	v	[$\bar{1}$11]	[$\bar{1}$01]	(101)	0.18
47	v	v	i	v	v	v	[$\bar{1}$11]	[1 $\bar{2}$ 1]	(101)	0.18
48	i	v	v	i	v	i	[001]	[$\bar{1}$10]	(110)	0.47
49	v	i	v	v	v	v	[1 $\bar{1}$ 1]	[1 $\bar{1}$ 1]	screw	
50	v	i	v	v	v	v	[1 $\bar{1}$ 1]	[1 $\bar{1}$ 1]	screw	
51	i	v	v	i	v	i	[001]	[032]	(100)	0.44
52	v	v	i	v	v	v	[$\bar{1}$11]	[$\bar{1}$11]	screw	
53	v	i	v	v	v	v	[1 $\bar{1}$ 1]	[1 $\bar{1}$ 1]	screw	
54	v	v	i	v	v	v	[$\bar{1}$11]	[110]	(1 $\bar{1}$2)	0.13
55	v	i	v	v	v	v	[1 $\bar{1}$ 1]	[1 $\bar{1}$ 1]	screw	
56	v	v	i	v	v	v	[$\bar{1}$11]	[$\bar{1}$11]	screw	
57	v	v	v	v	v	v	[1 $\bar{1}$ 1]	[$\bar{1}$01]	(121)	0.47
58	v	i	v	v	v	v	[1 $\bar{1}$ 1]	[0 $\bar{1}$ 1]	(011)	0.41
59	v	v	i	v	v	v	[$\bar{1}$11]	[$\bar{1}$11]	screw	
60	i	v	v	i	v	i	[001]	[$\bar{1}$12]	(110)	0.47
61	v	v	v	i		v	[0 $\bar{1}$ 1]	[001]	(100)	0.16
62	v	i	v	v	v	v	[1 $\bar{1}$ 1]	[101]	($\bar{1}$01)	0
63	v	i	v	v	v	v	[1 $\bar{1}$ 1]	[1 $\bar{1}$ 1]	screw	
64	v	v	v	v	i	v	[$\bar{1}$10]	[1 $\bar{1}$ 3]	(110)	0.17
65	v	i	v	v	v	v	[1 $\bar{1}$ 1]	[1 $\bar{1}$ 1]	screw	
66	v	i	v	v	v	v	[1 $\bar{1}$ 1]	[1 $\bar{1}$ 1]	screw	

Appendix VI Dislocation analysis of third thin foil of the material forged at 500°C. Orientation of analysed grain: near [331].

d	g $10\bar{1}$	$01\bar{1}$	$\bar{1}10$	002	200	b	u	p	m
1	i	v	v	v	v	$[1\bar{1}1]$	$[\bar{1}\bar{1}1]$	screw	
2	v	v	v	v	v	$[\bar{1}01]$			
3	v	i	v	v	v	$[\bar{1}11]$	$[\bar{1}13]$	(211)	0.12
4	v	i	v	v	v	$[\bar{1}11]$	$[11\bar{1}]$	(101)	0.09
5	v	v	i	v	v	$[11\bar{1}]$	$[11\bar{1}]$	screw	
6	v	v	v	v	i	$[0\bar{1}1]$			
7	v	v	i	v	v	$[11\bar{1}]$			
8	v	v	i	v	v	$[11\bar{1}]$	$[11\bar{1}]$	screw	
9	v	v	v	i	v	$[\bar{1}10]$	[001]	(110)	0
10	v	v	v	v	i	$[0\bar{1}1]$	$[13\bar{3}]$	(011)	0.21
11	v	v	i	v	i	[001]	[111]	$(\bar{1}10)$	0
12	v	v	v	v	v	$[\bar{1}01]$			
13	v	v	i	v	v	$[11\bar{1}]$	$[1\bar{1}1]$	(011)	0.43
14	i	v	v	i	i	[010]	$[2\bar{1}1]$	$(\bar{1}01)$	0.22
15	v	v	i	v	v	$[11\bar{1}]$	$[1\bar{2}2]$	(011)	0.43
16	i	v	v	i	i	[010]			
17	v	v	v	v	v	$[\bar{1}01]$	$[\bar{1}21]$	(101)	0.21
18	v	v	i	i	v	[110]			
19	v	v	v	v	v	$[\bar{1}01]$	[501]	(010)	0.22
20	v	v	i	v	v	$[11\bar{1}]$	$[\bar{1}01]$	(101)	0.43
21	v	i	v	i	v	[100]	$[11\bar{2}]$	(021)	0.16
22	v	v	i	v	v	[111]	$[1\bar{1}3]$	$(2\bar{1}1)$	0.25
23	v	v	i	v	v	[111]	$[1\bar{1}3]$	$(2\bar{1}1)$	0.25
24	i	v	v	v	v	$[1\bar{1}1]$	$[1\bar{1}1]$	screw	
25	i	v	v	v	v	$[1\bar{1}1]$	$[1\bar{1}1]$	screw	
26	v	v	v	v	i	$[0\bar{1}1]$	$[0\bar{2}1]$	(100)	0.22
27	v	i	v	i	v	[100]	$[1\bar{1}1]$	(011)	0.45
28	v	v	v	v	v	$[\bar{1}01]$	$[\bar{1}11]$	(101)	0.21
29	i	v	v	v	v	$[1\bar{1}1]$	$[1\bar{1}1]$	screw	
30	i	v	v	v	v	$[1\bar{1}1]$	$[1\bar{3}3]$	(011)	0.09
31	v	i	v	i	v	[100]	$[0\bar{1}1]$	(011)	0.45

Appendix VI continued

32	v	v	i	v	v	[11$\bar{1}$]	[11$\bar{1}$]	screw	
33	v	v	i	v	v	[11$\bar{1}$]	[11$\bar{1}$]	screw	
34	v	v	i	v	v	[111]	[0$\bar{1}$1]	(011)	0.43
35	v	i	v	v	v	[11$\bar{1}$]	[1$\bar{1}$1]	(110)	0.22
36	v	v	i	v	v	[$\bar{1}$11]	[21$\bar{1}$]	(011)	0.43
37	v	v	v	v	v	[$\bar{1}$01]			
38	v	i	v	i	v	[100]	[120]	(001)	0.16
39	v	v	i	v	i	[11$\bar{1}$]	[120]	(2$\bar{1}$1)	0.25
40	v	v	i	v	v	[11$\bar{1}$]	[21$\bar{1}$]	(011)	0.43
41	v	v	i	v	v	[11$\bar{1}$]	[10$\bar{1}$]	(101)	0.43
42	v	v	i	v	v	[11$\bar{1}$]	[21$\bar{3}$]	(2$\bar{1}$1)	0.25
43	v	v	i	v	v	[11$\bar{1}$]	[213]	(2$\bar{1}$1)	0.25
44	v	v	i	v	v	[11$\bar{1}$]	[$\bar{3}$13]	(101)	0.43
45	v	v	i	v	v	[11$\bar{1}$]	[1$\bar{2}$2]	(011)	0.43
46	i	v	v	v	v	[11$\bar{1}$]	[11$\bar{1}$]	(011)	0
47	v	v	i	v	v	[11$\bar{1}$]	[122]	(011)	0.43
48	v	i	v	i	v	[100]	[105]	(010)	0.47

Appendix VII Dislocation analysis on three thin foils of the material forged at 500°C

1	proportion of <100>:<110>:<111>		17 : 1 : 33	9 : 6 : 17	12 : 6 : 48	8 : 11 : 29
2	percentage of [100]		22%	0%	0%	10%
3	percentage of [010]		0%	3%	3%	4%
4	percentage of [001]		12%	25%	15%	2%
5	percentage of <110>		2%	19%	9%	23%
6	percentage of [11]		30%	0%	0%	0%
7	percentage of [11]		34%	28%	30%	6%
8	percentage of [11]		0%	19%	42%	13%
9	percentage of [11]		0%	6%	0%	42%
10	*analysed thin foil*		*1st thin foil*	*2nd thin foil*	*2nd thin foil*	*3rd thin foil*
11	field			field one	field two	
12	orientation of analysed grain		[001]	[212]	[212]	[331]
13	characteristic of analysed grain		non-recrystallised	non-recrystallised	non-recrystallised	non-recrystallised
14	number of total dislocations		50	32	66	48
15	[100]	percentage with high m	0%	0%	0%	60%
16		percentage with low m	100%	0%	0%	40%
17	[010]	percentage with high m	0%	/	0%	0%
18		percentage with low m	0%	/	100%	50%
19	[001]	percentage with high m	/	75%	100%	0%
20		percentage with low m	/	/	0%	100%
21	[11]	percentage with high m	81%	0%	0%	0%
22		percentage with low m	0%	0%	0%	0%
23	[11]	percentage with high m	76%	56%	55%	0%
24		percentage with low m	24%	44%	45%	67%
25	[11]	percentage with high m	0%	100%	89%	67%
26		percentage with low m	0%	0%	11%	33%
27	[11]	percentage with high m	0%	0%	0%	20%
28		percentage with low m	0%	100%	0%	0%
29	<100>	percentage with high m	0%	67%	83%	38%
30		percentage with low m	50%	0%	17%	50%
31	<110>	percentage with high m	0%	0%	0%	0%
32		percentage with low m	100%	83%	100%	55%
33	<111>	percentage with high m	79%	65%	75%	62%
34		percentage with low m	12%	35%	25%	14%
35	proportion of [100]:[010]:[001]					
36	with high Schmid factor, m		0 : 0 : --	0 : 0 : 6	0 : 0 : 10	3 : 0 : 0
37	comments		<111> dominate	<111> dominate	<111> dominate	<111> dominate

Note: **Line 1** shows the proportion of three types of dislocations <100>, <110> and <111>.
Lines 2-4, line 5 and lines 6-9 indicate the percentages of three variants of <100> dislocations of the total dislocations analysed, the percentage of <110> dislocations of the total dilsocations and the percentages of four variants of <111> dislocations of the total dislocations, respectively.
Line 15 and **line 16** show the percentages of [100] dislocations with high and with low Schmid factor of the total [100] dislocations analysed. **Lines 17-20** have the similar meaning.
Line 21 and **line 22** show the percentages of [111] variant with high and with low Schmid factor of the total [111] dislocations. **Lines 23-28** have the similar meaning.
Lines 29-34 show the percentages of three types of dislocations <100>, <110> and <111> with high and with low Schmid factor of the total dislocations of each type.
Lines 35-36 show the proportion of three <100> variants with high Schmid factor.

Appendix VIII Dislocation analysis of subgrain B in fig. 4-34. Orientation of analysed subgrain: near [111]

d	g $\bar{1}01$	$0\bar{1}1$	$1\bar{1}0$	002	200	b	u	p	m
1	v	v	i	v	i	[001]			
2	v	i	v	i	v	{100}	{001}	(010)	0.33
3	v	i	v	i	v	[100]	$[\bar{1}22]$	$(0\bar{1}1)$	0
4	i	v	v	i	i	{010}	{130}	(001)	0.33
5	v	i	v	i	v	[100]			
6	v	i	v	i	v	{100}			
7	v	i	v	i	v	[100]			
8	v	v	i	v	i	[001]	{010}	(100)	0.33
9	i	v	v	i	i	[010]	{150}	(001)	0.33
10	v	i	v	i	v	{100}	$\{13\bar{3}\}$	(011)	0.47
11	v	i	v	i	v	{100}			
12	v	i	v	v	i	{011}	$\{01\bar{1}\}$	(100)	0.47
13	v	i	v	i	v	[100]	$[\bar{3}21]$	$(0\bar{1}2)$	0.15
14	v	i	v	i	v	{100}			
15	v	i	v	v	i	{011}			
16	v	i	v	v	i	{011}			
17	v	i	v	i	v	[100]	[111]	$(0\bar{1}1)$	0
18	v	v	i	v	i	{001}	{510}	(010)	0.33
19	i	v	v	i	i	{010}	$[\bar{2}01]$	(102)	0.15
20	v	v	i	v	i	{001}			
21	i	v	v	i	i	{010}			
22	v	i	v	i	v	[100]	[001]	(010)	0.33
23	v	v	v	i	v	$[\bar{1}10]$	[001]	(110)	0
24	v	v	i	v	i	{001}	$[\bar{3}01]$	(010)	0.33
25	i	v	v	i	i	{010}			
26	v	v	i	v	i	{001}			
27	v	v	i	v	i	{001}			
28	v	v	i	v	i	{001}			
29	i	v	v	v	v	$[1\bar{1}1]$	$[13\bar{3}]$	(011)	0.27
30	v	i	v	i	v	[100]	[001]	(010)	0.33
31	v	i	v	i	v	[100]			

Appendix VIII continued

32	v	i	v	i	v	[100]	[111]	$(0\bar{1}1)$	0
33	v	i	v	i	v	[100]			
34	i	v	v	i	i	[010]			
35	v	v	i	v	i	[001]			
36	v	v	i	v	i	[001]			
37	v	i	v	i	v	[100]	[130]	(001)	0.33
38	v	v	i	v	i	[001]			
39	i	v	v	i	i	[010]			
40	i	v	v	i	i	[010]			
41	v	i	v	i	v	[100]	[001]	(010)	0.33
42	v	v	i	v	i	[001]			
43	i	v	v	i	i	[010]			
44	i	v	v	i	i	[010]			
45	v	v	i	v	i	[001]	[010]	(100)	0.33
46	v	v	i	v	i	[001]	[010]	(100)	0.33
47	v	v	i	v	i	[001]	[010]	(100)	0.33
48	v	v	i	v	i	[001]	[010]	(100)	0.33
49	v	v	i	v	i	[001]	[010]	(100)	0.33
50	v	v	i	v	i	[001]	[010]	(100)	0.33
51	i	v	v	i	i	[010]			
52	v	v	i	v	i	[001]			
53	v	v	i	v	i	[001]			

Appendix IX Dislocation analysis of subgrain C in fig. 4-34. Orientation of analysed subgrain: near [$\bar{1}11$]

d	g $\bar{1}01$	$0\bar{1}1$	$1\bar{1}0$	002	200	b	u	p	m
1	v	i	v	i	v	[100]	[001]	(010)	0.33
2	v	i	v	i	v	[100]	[001]	(010)	0.33
3	v	i	v	i	v	[100]	[11$\bar{1}$]	(011)	0.33
4	v	i	v	i	v	[100]	[001]	(010)	0.33
5	v	v	i	v	i	[001]			
6	v	v	i	v	i	[001]	[010]	(100)	0.33
7	i	v	v	i	i	[010]	[$\bar{2}$01]	(102)	0.45
8	i	v	v	i	i	[010]	[$\bar{2}$01]	(102)	0.45
9	i	v	v	i	i	[010]	[$\bar{2}$01]	(102)	0.45
10	v	v	i	v	i	[001]	[100]	(010)	0.33
11	i	v	v	i	i	[010]	[$\bar{2}$01]	(102)	0.45
12	i	v	v	i	i	[010]	[100]	(001)	0.33
13	i	v	v	i	i	[010]	[100]	(001)	0.33
14	v	i	v	i	v	[100]	[1$\bar{2}$1]	(012)	0.45
15	i	v	v	i	i	[010]	[100]	(001)	0.33
16	v	i	v	i	v	[100]	[101]	(010)	0.33
17	i	v	v	i	i	[010]	[100]	(001)	0.33
18	i	v	v	i	i	[010]	[100]	(001)	0.33
19	i	v	v	i	i	[010]	[100]	(001)	0.33
20	v	v	i	v	i	[001]			
21	i	v	v	i	i	[010]	[$\bar{1}$11]	(101)	0.47
22	i	v	v	i	i	[010]	[$\bar{2}$01]	(102)	0.45
23	v	v	i	v	i	[001]	[100]	(010)	0.33
24	i	v	v	i	i	[010]			
25	v	i	v	i	v	[100]	[011]	(0$\bar{1}$1)	0
26	v	v	v	i	v	[$\bar{1}$10]	[001]	(110)	0
27	v	v	i	v	i	[001]	[0$\bar{3}$1]	(100)	0.33
28	v	i	v	i	v	[100]	[0$\bar{1}$2]	(021)	0.45
29	v	v	i	v	i	[001]	[032]	(100)	0.33
30	v	v	i	v	i	[001]	[0$\bar{3}$1]	(100)	0.33
31	v	i	v	v	v	[$\bar{1}$11]	[011]	(0$\bar{1}$1)	0

Appendix IX continued

32	v	v	i	v	i	[001]	[100]	(010)	0.33
33	i	v	v	i	i	[010]			
34	i	v	v	i	i	[010]	[100]	(001)	0.33
A	v	i	v	v	i	[011]	[$0\bar{1}1$]	(100)	0.47
35	v	i	v	v	v	[$\bar{1}11$]	[001]	(110)	0.27
36	i	v	v	i	i	[010]			
37	i	v	v	i	i	[010]			
38	i	v	v	i	i	[010]			
39	v	i	v	v	v	[$\bar{1}11$]	[010]	(101)	0.27
40	v	i	v	i	v	[100]			
41	v	v	i	v	i	[001]	[$\bar{3}01$]	(010)	0.33
42	i	v	v	i	i	[010]	[100]	(001)	0.33
43	i	v	v	i	i	[010]			
44	i	v	v	i	i	[010]			
45	i	v	v	i	i	[010]			
46	v	v	v	v	v	[$\bar{1}01$]	[011]	($1\bar{1}1$)	0
47	i	v	v	i	i	[010]			

Appendix X Dislocation analysis of an area of a second thin foil of the material forged at 800°C. Orientation of analysed subgrain: near [111]

d	g $10\bar{1}$	$01\bar{1}$	$1\bar{1}0$	002	200	$\bar{b}$	$\bar{u}$	p	m
1	i	v	v	i	i	[010]	$[\bar{3}10]$	(001)	0.33
2	i	v	v	i	i	[010]	[100[	(001)	0.33
3	i	v	v	i	i	[010]	[100]	(001)	0.33
4	v	v	i	v	i	[001]	[012]	(100)	0.33
5	v	v	i	v	i	[001]	$[2\bar{2}1]$	(110)	0.47
6	v	v	i	v	i	[001]	$[3\bar{1}1]$	$(\bar{1}20)$	0.15
7	v	v	i	v	i	[001]	[201]	(010)	0.33
8	v	v	i	v	v	$[11\bar{1}]$			
9	v	v	i	v	i	[001]			
10	i	v	v	i	i	[010]	$[2\bar{1}0]$	(001)	0.33
11	i	v	v	i	i	[010]	$[3\bar{1}0]$	(001)	0.33
12	i	v	v	i	i	[010]			
13	i	v	v	i	i	[010]			
14	v	v	i	v	i	[001]			
15	i	v	v	i	i	[010]	[100]	(001)	0.33
16	i	v	v	i	i	[010]	[100]	(001)	0.33
17	i	v	v	i	i	[010]	$[\bar{2}11]$	(102)	0.45
18	v	i	v	i	v	[100]	$[0\bar{1}1]$	(011)	0.47
19	v	v	i	v	i	[001]	$[\bar{2}10]$	(120)	0.45
20	i	v	v	v	v	[101]			
21	v	v	i	v	i	[001]	[010]	(100)	0.33
22	i	v	v	i	i	[010]	[111]	$(\bar{1}01)$	0
23	i	v	v	i	i	[010]			
24	i	v	v	i	i	[010]			
25	i	v	v	i	i	[010]			
26	v	i	v	i	v	[100]			
27	i	v	v	i	i	[010]	[221]	$(\bar{1}02)$	0.15
28	i	v	v	i	i	[010]	[111]	$(\bar{1}01)$	0
30	v	i	v	i	v	[100]			
31	i	v	v	i	i	[010]			
32	v	v	i	i	v	[110]			

Appendix X continued

29	v	i	v	i	v	[100]	[1 $\bar{1}$ 1]	(011)	0.47
33	v	i	v	i	v	[100]			
34	i	v	v	i	i	[010]	[111]	($\bar{1}$01)	0
35	i	v	v	i	i	[010]	[111]	($\bar{1}$01)	0
36	i	v	v	i	i	[010]	[111]	($\bar{1}$01)	0
37	i	v	v	i	i	[010]	[111]	(101)	0
38	v	i	v	i	v	[100]	[001]	(010)	0.33
39	v	i	v	i	v	[100]	[001]	(010)	0.33
40	i	v	v	i	i	[010]	[001]	(100)	0.33
41	i	v	v	i	i	[010]	[001]	(100)	0.33
42	v	i	v	i	v	[100]	[$\bar{1}$20]	(001)	0.33
43	v	i	v	i	v	[100]	[010]	(001)	0.33
44	i	v	v	i	i	[010]	[001]	(100)	0.33
45	v	i	v	i	v	[100]			
46	v	i	v	v	i	[011]	[010]	(100)	0.33
47	v	i	v	v	i	[011]	[$\bar{1}$20]	(2 $\bar{1}$ 1)	0.38
48	v	i	v	v	i	[011]	[$\bar{1}$20]	(2 $\bar{1}$ 1)	0.38
49	v	i	v	v	i	[011]	[$\bar{1}$20]	(21 $\bar{1}$)	0.38
50	i	v	v	i	i	[010]			
51	i	v	v	i	i	[010]	[0 $\bar{1}$ 3]	(100)	0.33
52	i	v	v	i	i	[010]	[0 $\bar{1}$ 3]	(100)	0.33
53	v	v	i	i	v	[110]	[23 $\bar{1}$]	($\bar{1}$12)	0.38
54	v	i	v	v	v	[$\bar{1}$ 11]	[$\bar{1}$10]	(110)	0.27
55	v	i	v	i	v	[100]	[1 $\bar{1}$ 1]	(011)	0.47
56	v	v	i	v	i	[001]	[100]	(010)	0.33
57	v	i	v	i	v	[100]			
58	i	v	v	i	i	[010]	[$\bar{1}$11]	(101)	0.47
59	i	v	v	i	i	[010]			

Appendix XI Summary of dislocation analysis on four thin foils of the material forged at 800°C

1	proportion of <100>:<110>:<111>		47 : 6 : 0	48 : 4 : 7	45 : 3 : 5	24 : 4 : 2	14 : 3 : 0	1 : 10 : 1	30 : 11 : 4	37 : 11 : 0	30 : 9 : 2	38 : 3 : 10	39 : 3 : 19
2	percentage of [100]		36%	34%	19%	23%	35%	8%	44%	21%	20%	38%	29%
3	percentage of [010]		30%	20%	48%	30%	18%	0%	6%	31%	48%	23%	23%
4	percentage of [001]		21%	40%	31%	37%	29%	0%	6%	25%	15%	25%	28%
5	percentage of <110>		11%	8%	6%	13%	18%	83%	12%	23%	15%	3%	3%
6	percentage of [111]		0%	0%	0%	3%	0%	0%	3%	0%	0%	1%	3%
7	percentage of [11]		0%	0%	0%	0%	0%	8%	2%	0%	2%	0%	1%
8	percentage of [111]		0%	2%	0%	0%	0%	0%	0%	0%	0%	3%	11%
9	percentage of [111]		0%	0%	0%	0%	0%	0%	0%	0%	2%	0%	0%
10	analysed thin foil		1st thin foil	1st thin foil	1st thin foil	2nd thin foil	2nd thin foil	2nd thin foil	2nd thin foil	3rd thin foil	3rd thin foil	4th thin foil	4th thin foil
11	field		field one	field two	field three	field one	field two	field three	field one	field two	field three	field one	field two
12	orientation of analysed grain		[111]	[111]	[111]	[111]	[111]	[001]	[001]	[111]	[331]	[553]	[101]
13	characteristic of analysed grain		non-recrystallized	non-recrystallized	non-recrystallized	non-recrystallized	non-recrystallized	recrystallized	recrystallized	non-recrystallized	non-recrystallized	recrystallized	recrystallized
14	number of total dislocations		53	53	48	50	87	13	61	48	61	211	117
15	[100]	percentage with high m	55%	31%	29%	30%	83%	0%	0%	20%	50%	7%	36%
16		percentage with low m	15%	34%	11%	15%	12%	100%	50%	0%	0%	93%	13%
17	[010]	percentage with high m	44%	20%	61%	50%	66%	0%	0%	20%	47%	0%	0%
18		percentage with low m	6%	0%	0%	0%	33%	0%	100%	27%	10%	100%	100%
19	[001]	percentage with high m	64%	43%	70%	50%	80%	0%	0%	50%	66%	11%	63%
20		percentage with low m	18%	0%	0%	0%	0%	0%	100%	25%	0%	82%	22%
21	[111]	percentage with high m	0%	0%	0%	0%	0%	0%	0%	0%	0%	0%	67%
22		percentage with low m	0%	0%	0%	100%	0%	0%	0%	0%	0%	100%	0%
23	[11]	percentage with high m	0%	0%	0%	0%	0%	0%	0%	0%	0%	0%	0%
24		percentage with low m	0%	0%	100%	0%	0%	100%	0%	0%	100%	0%	0%
25	[111]	percentage with high m	0%	0%	0%	0%	0%	0%	0%	0%	0%	75%	82%
26		percentage with low m	0%	100%	0%	0%	0%	0%	0%	0%	50%	32%	18%
27	[111]	percentage with high m	0%	0%	0%	0%	0%	0%	0%	0%	0%	0%	0%
28		percentage with low m	0%	0%	0%	0%	0%	0%	0%	0%	0%	0%	0%
29	<100>	percentage with high m	53%	53%	67%	82%	74%	0%	0%	30%	53%	0%	36%
30		percentage with low m	13%	9%	2%	4%	14%	100%	50%	19%	12%	92%	40%
31	<110>	percentage with high m	83%	40%	0%	50%	33%	0%	25%	0%	36%	0%	66%
32		percentage with low m	17%	20%	66%	50%	33%	100%	0%	100%	0%	63%	0%
33	<111>	percentage with high m	0%	100%	0%	0%	0%	0%	50%	0%	0%	70%	68%
34		percentage with low m	0%	0%	100%	100%	0%	100%	0%	0%	50%	20%	10%
35	proportion of [100]:[010]:[001]												
36	with high Schmid factor, m		11 : 9 : 5	6 : 2 : 10	3 : 14 : 7	2 : 3 : 5	5 : 8 : 4	0 : 0 : 0	0 : 0 : 0	2 : 3 : 6	6 : 10 : 6	3 : 9 : 3	12 : 0 : 20
37	comments		<100> dominate	<100> dominate	<100> dominate	<100> dominate	<100> dominate		<100> dominate	<100> dominate	<100> dominate	<100> dominate	<100> dominate

Note: **Line 1** shows the proportion of three types of dislocations <100>, <110> and <111>.
Lines 2-4, line 5 and lines 6-9 indicate the percentages of three variants of <100> dislocations of the total dislocations analysed, the percentage of <110> dislocations of the total dislocations and the percentages of four variants of <111> dislocations of the total dislocations, respectively.
Line 15 and line 16 show the percentages of [100] dislocations with high and with low Schmid factor of the total [100] dislocations analysed. **Lines 17-20** have the similar meaning.
Line 21 and line 22 show the percentages of [111] variant with high and with low Schmid factor of the total [111] dislocations. **Lines 23-28** have the similar meaning.
Lines 29-34 show the percentages of three types of dislocations <100>, <110> and <111> with high and with low Schmid factor of the total dislocations of each type.
Lines 35-36 show the proportion of three <100> variants with high Schmid factor.

Appendix XII Dislocation analysis of the area shown in fig. 4-42 (forging at 1000°C. Orientation of analysed subgrain: near [111]

d	g 0$\bar{1}$1	$\bar{1}$01	1$\bar{1}$0	020	002	b	u	p	m
1	i	v	v	i	i	[100]	[1$\bar{1}$0]	(001)	0.33
2	i	v	v	i	i	[100]	[101]	(010)	0.33
3	v	i	v	v	i	[010]	[$\bar{2}$10]	(001)	0.33
4	i	v	v	i	i	[100]	[101]	(010)	0.33
5	i	v	v	i	i	[100]	[101]	(010)	0.33
6	v	v	i	i	v	[001]	[010]	(100)	0.33
7	v	v	i	i	v	[001]	[010]	(100)	0.33
8	v	v	i	i	v	[001]	[010]	(100)	0.33
9	i	i	i	v	v	[111]	[$\bar{2}$11]	(011)	0
10	i	i	i	v	v	[111]			
11	i	i	i	v	v	[111]	[100]	(0$\bar{1}$1)	0
12	v	i	v	i	i	[101]			
13	i	v	v	i	i	[100]			
14	v	i	v	v	i	[010]	[1$\bar{2}$0]	(001)	0.33
15	v	v	i	v	i	[110]	[11$\bar{1}$]	(1$\bar{1}$0)	0
16	v	v	i	i	v	[001]			
17	v	v	i	v	v	[11$\bar{1}$]			
18	v	v	i	i	v	[001]	[100]	(010)	0.33
19	i	v	v	i	i	[100]	[$\bar{1}$11]	(0$\bar{1}$1)	0
20	v	i	v	v	i	[010]	[$\bar{2}$01]	(102)	0.26
21	v	i	v	v	i	[010]	[$\bar{1}$01]	(101)	0.47
22	v	v	i	i	v	[001]	[010]	(100)	0.33
23	v	v	i	i	v	[001]	[011]	(100)	0.33
24	v	i	v	i	i	[101]			
25	v	i	v	v	i	[010]	[123]	(100)	0.33
26	v	i	v	v	i	*[010]*			
27	v	i	v	v	i	[010]			
28	v	i	v	v	i	[010]	[11$\bar{2}$]	(201)	0.47
29	v	v	i	i	v	[001]			
30	v	i	v	v	v	[1$\bar{1}$1]	[$\bar{1}$13]	(110)	0.27
31	v	v	v	v	v	[0$\bar{1}$1]			
32	v	v	i	i	v	[001]			

Appendix XII continued

33	v	i	v	v	i	[010]	[210]	(001)	0.33
34	v	v	i	i	v	[001]	[1 $\bar{1}$ 2]	(110)	0.47
35	v	v	i	i	v	[001]			
36	v	v	i	i	v	[001]			
37	v	v	i	i	v	[001]			
38	i	v	v	i	i	[100]			
39	i	v	v	i	i	[100]			
40	v	i	v	v	v	[1 $\bar{1}$ 1]			
41	i	v	v	i	i	[100]			
42	v	v	i	i	v	[001]			
43	v	v	i	i	v	[001]			
44	v	v	i	i	v	[001]			
45	i	v	v	i	i	[100]	[010]	(001)	0.33
46	v	i	v	v	i	[010]	[100]	(001)	0.33
47	v	v	i	i	v	[001]	[010]	(100)	0.33
48	v	v	i	i	v	[001]	[100]	(010)	0.33

Appendix XIII Summary of dislocation analysis on three thin foils of the material forged at 1000°C

1	proportion of <100>:<110>:<111>		64 : 2 : 4	50 : 11 : 5	38 : 4 : 6	44 : 10 : 10
2	percentage of [100]		7%	21%	21%	27%
3	percentage of [010]		49%	10%	21%	5%
4	percentage of [001]		36%	43%	38%	38%
5	percentage of <110>		3%	16%	8%	16
6	percentage of [110]		4%	0%	6%	6%
7	percentage of [11$\bar{1}$]		0%	4%	0%	2%
8	percentage of [1$\bar{1}$1]		1%	1%	4%	6%
9	percentage of [$\bar{1}$11]		1%	1%	2%	2%
10	analysed thin foil		1st thin foil	2nd thin foil	2nd thin foil	3rd thin foil
11	field			field one	field two	
12	orientation of analysed grain		[$\bar{1}$33]	[111]	[133]	[001]
13	characteristic of analysed grian		non-recrystallised	non-recrystallised	non-recrystallised	non-recrystallised
14	number of total dislocations		70	67	48	64
15	[100]	percentage with high m	100%	100%	50%	0%
16		percentage with low m	0%	0%	50	100%
17	[010]	percentage with high m	100%	100%	100%	0%
18		percentage with low m	0%	0%	0%	100%
19	[001]	percentage with high m	100%	100%	83%	0%
20		percentage with low m	5%	0%	0%	100%
21	[111]	percentage with high m	0%	0%	0%	0%
22		percentage with low m	100%	0%	66%	0%
23	[$\bar{1}$11]	percentage with high m	0%	33%	0%	0%
24		percentage with low m	0%	33%	0%	0%
25	[1$\bar{1}$1]	percentage with high m	100%	0%	0%	50%
26		percentage with low m	0%	0%	50%	50%
27	[11$\bar{1}$]	percentage with high m	100%	100%	0%	0%
28		percentage with low m	0%	0%	0%	0%
29	<100>	percentage with high m	100%	100%	79%	0%
30		percentage with low m	0%	0%	3%	100%
31	<110>	percentage with high m	0%	91%	0%	100%
32		percentage with low m	67%	0%	50%	0%
33	<111>	percentage with high m	50%	40%	0%	20%
34		percentage with low m	50%	20%	50%	20%
35	proportion of [100]:[010]:[001]					
36	with high Schmid factor, m		5 : 34 : 25	14 : 7 : 29	5 : 10 : 15	0 : 0 : 0
37	comments		<100> dominate	<100> dominate	<100> dominate	

Note: **Line 1** shows the proportion of three types of dislocations <100>, <110> and <111>.
Lines 2-4, line 5 and lines 6-9 indicate the percentages of three variants of <100> dislocations of the total dislocations analysed, the percentage of <110> dislocations of the total dislocations and the percentages of four variants of <111> dislocations of the total dislocations, respectively.
Line 15 and line 16 show the percentages of [100] dislocations with high and with low Schmid factor of the total [100] dislocations analysed. **Lines 17-20** have the similar meaning.
Line 21 and line 22 show the percentages of [111] variant with high and with low Schmid factor of the total [111] dislocations. **Lines 23-28** have the similar meaning.
Lines 29-34 show the percentages of three types of dislocations <100>, <110> and <111> with high and with low Schmid factor of the total dislocations of each type.
Lines 35-36 show the proportion of three <100> variants with high Schmid factor.

Bibliography

Bibliography:

1. R.W.Cahn, P.Haasen, Physical Metallurgy, North-Holland Physics Publishing, Elsevier Science Publishing B.V., The Netherlands (1983)
2. G.Sauthoff, Zeitshrift für Metallkunde, Band 80, Heft 5, 337 (1989)
3. G.Sauthoff, Intermetallics, VCH Verlagsgesellschaft mbH, D-69451 Weinheim (1995)
4. C.G.McKamey, J.H.DeVan, P.F.Tortorelli, and V.K.Sikka, J.Mater.Res., Vol.6, 1779 (1991)
5. N.S.Stoloff, Mat.Res.Soc.Symp.Proc., Vol.39, 1 (1985)
6. D.J.Gaydosh, S.L.Draper, and M.V.Nathal, Metall. Trans. A, Vol. 20A, 1701 (1989)
7. D.G.Morris, Acta Metall.Sin.(English letters), Vol. 8, 393 (1995)
8. D.L.Joslin, D.S.Easton, C.T.Liu, S.S.Babr and S.A.David, Intermetallics, Vol.3, 467 (1995)
9. S.C.Deevi and V.K.Sikka, Intermetallics, Vol.4, 357 (1996)
10. Thadders B.Massalski, Binary Alloy Diagrams, Vol.1, American Society for Metals, Metals Park, Ohio 44073, U.S.A., 112 (1986)
11. Metal Handbook, 10th edition, Vol.3, ASM International, Handbook Commitee, U.S.A. (1990)
12. G.Thomas and J.Washburn, Interscience Publishing, New York, 333 (1963)
13. Metal Handbook, 10th edition, Vol.2, ASM International, Handbook Commitee, U.S.A. (1990)
14. J.H.Westbrook and R.L.Fleischer, Intermetallic Compounds, Principles and Practice, Vol.2, JOHN WILEY & SONS, 203 (1995)
15. N.V.Nathal and C.T.Liu, Intermetallics, Vol.3, 77 (1995)
16. O.Klein and I.Baker, Scripta Metall., Vol.30, No.11, 1413 (1994)
17. C.G.McKamey and J.A.Horton, Metall. Trans. A, Vol.20, 751 (1989)
18. I.Baker, H.Xiao, O.Klein, C.Nelson and J.D.Whittenberger, Acta Metall. Mater., Vol.43, No.4, 1723 (1995)
19. J.D.Whittenberger, M.V.Nathal and D.J.Gaydosh, Intermetallics, Vol.2, 193 (1994)

20. R.Carleton, E.P.George and R.H.Zee, Intermetallics, Vol.3, 433 (1995)

21. C.G.McKamey, J.A.Horton and C.T.Liu, J.Mater.Res., Vol.4, No.5, 1156 (1989)

22. C.G.McKamey, P.J.Masiasz, J.W.Jones, J.Mater.Res., Vol.7, No.8, 2098 (1992)

23. C.G.McKamey, P.J.Masiasz, G.M.Goodwin and T.Zacharia, Mater.Sci.Eng., A174, 59 (1994)

24. Y.Nishino, S.Asano, T.Ogawa, Mater.Sci.Eng., A234-236, 271 (1994)

25. P.G.Sanders, V.K.Sikka, C.R.Howell and R.H.Baldwin, Scrpta Metall., Vol.25, 2365 (1991)

26. S.Viswanathan, B.R.Shelton, J.K.Wright and V.K.Sikka, Scripta Metall., Vol.29, 589 (1993)

27. C.G.McKamey and K.H.Pierce, Scripta Metall., Vol.28, 1173 (1993)

28. C.H.Kong and P.R.Munroe, Scripta Metall., Vol.28, 1241 (1993)

29. D.G.Morris, S.Gunther and C.Briguet, Scripta Metall., Vol.37, 71 (1997)

30. P.Nagpal and I.Baker, Metall. Trans., Vol.21A, 2281 (1990)

31. A.Agarwal, R.Balasubramaniam and S.Bhargava, Metall. Trans., Vol.27A, 2985 (1996)

32. D.G.Morris and M.LeBoeuf, Acta Metall.Mater., Vol.42, No.6, 1817 (1994)

33. P.J.Masiasz, D.J.Alexander and J.L.Wright, Intermetallics, Vol.5, 547 (1997)

34. K.-M Chang, Metall.Trans., Vol.21A, 3027 (1990)

35. M.Jain and T.Christman, NanoStructured Mater., Vol.7, No.7, 719 (1996)

36. B.H.Rabin, J.K.Wright, R.N.Wright and C.H.Sellers, J.Mater.Res., Vol.9, No.6, 1384 (1994)

37. K.Wolski, F.Thévenot and J.Le Coze, Intermetallics, Vol.4, 299 (1996)

38. C.T.Liu, E.H.Lee and C.G.McKamey, Scripta Metall., Vol.23, 875 (1989)

39. C.T.Liu, C.G.McKamey and E.H.Lee, Scripta Metall., Vol.24, 385 (1990)

40. J.C.M.Li and C.T.Liu, Scripta Metall., Vol.27, 1701 (1992)

41. N.S.Stoloff and C.T.Liu, Intermetallics, Vol.2, 75 (1994)

42. A.Kimura, H.Izumi, H.Saitoh and T.Misawa, Intermetallics, Vol.3, 115 (1995)

43. P.Specht and P.Neumann, Intermetallics, Vol.3, 365 (1995)

44. C.L.Fu and G.S.Painter, J.Mater.Res., Vol.6, 719 (1991)

45. Y.Makino, Intermetallics, Vol.4, S11 (1996)

46. J.H.Schneibel, E.P.George and I.M.Anderson, Intermetallics, Vol.5, 185 (1997)

47. I.M.Anderson, Acta Mater., Vol.45, No.9, 3897 (1997)

48. D.S.Xu, Y.Song, D.Li and Z.W.Hu, Mater.Sci.Eng., A234-236, 230 (1997)

49. Jian-Hua Xu and A.J.Freeman, J.Mater.Res., Vol.9, No.7 1755 (1994)

50. Tao Hong and A.J.Freeman, Mat.Res.Soc.Symp.Proc., Vol.133, 75 (1989)

51. I.Baker, Mater.Sci.Eng., A192/193, 1 (1995)

52. S.Hanada, S.Watanabe, T.Sato and O.Izumi, Scripta Metall., Vol.15, 1345 (1981)

53. H.Inouye, Mater.Res.Soc.Symp.Proc., Vol.39, 255 (1985)

54. W.Schröer, H.Mecking and C.Hartig, Proc.*Inter.Symp., Intermetallics* Compound-Structure and Mechanical Properties, JIMIS-69, O.Izumi (ed), The Japan Institure of Metals, Sendai, 567 (1991)

55. W.Schröer, C.Hartig and H.Mecking, Z.Metallkunde, Band 84, Heft 5, 294 (1993)

56. D.G.Morris and D.Peguiron, Phil.Mag.A, Vol.71, No.2, 441 (1995)

57. U.Prakash, R.A.Buckley, H.Jones and C.M.Sellars, ISIJ International, Vol.31, 1112 (1991)

58. J.T.Guo, O.Jin, W.M.Yin and T.M.Wang, Scripta Metall., Vol.29, 783 (1993)

59. H.Xiao and I.Baker, Scripta Metall., Vol.28, 1411 (1993)

60. T.Takasugi, S.Hanada, M.Yoshida and D.Shindo, Phil. Mag.A, Vol.71, No.2, 347 (1995)

61. K.Yoshimi, S.Hanada and M.H.Yoo, Acta Metall.Mater., Vol.43, No.11, 4141 (1995)

62. K.Yoshimi, S.Hanada and M.H.Yoo, Intermetallics, Vol.4, S159 (1996)

63. K.Yoshimi, S.Hanada and M.H.Yoo, Intermetallics, Vol.4, 159 (1996)

64. D.G.Morris and M.A.Morris, Intermetallics, Vol.5, 245 (1997)

65. D.G.Morris and M.A.Morris, Mater.Sci.Eng., A239-240, 23 (1997)

66. I.Baker and Y.Yang, Mater.Sci.Eng., A239-240, 109 (1997)

67. X.Li and I.Baker, Scripta Metall., Vol.36, No.12, 1387 (1997)

68. Y.M.Zhu and H.Saka, Phil.Mag.A, Vol.59, No.3, 661 (1989)

69. M.J.Mills, N.Baluc and H.P.Karnthaler, Mater.Res.Soc.Symp.Proc., Vol.33, 203 (1989)

70. N.S.Stoloff and R.G.Davies, Acta Metall., Vol.12, 473 (1964)

71. M.J.Marcinkowski and H.Chessin, Phil.Mag.A, Vol.10, 837 (1964)

72. Y.Umakoshi, M.Yamaguchi, Y.Namba, M.Murakami, Acta Metall., Vol.24, 89 (1976)

73. A.Nohara, T.Imura, Phys.Stat. Sol.(a), Vol.84, 501 (1984)

74. A.Brinck, C.Engelke and H.Neuhäuser, Mater.Sci.Eng., A234-236, 418 (1997)

75. D.Raabe, J.Deichel and G.Gottstein, Acta Mater., Vol.45, No.7, 2839 (1997)

76. D.Raabe and W.Mao, Phil.Mag.A, Vol.71, No.4, 805 (1995)

77. B.K.Kad, S.E.Schoenfeld, R.J.Asaro, C.G.McKamey and V.K.Sikka, Acta Metall., Vol.45, No.4, 1333 (1997)

78. H.J.Leamy, F.X.Kayser and M.J.Marcinkowski, Phil.Mag.A, Vol.20, 779 (1969)

79. R.C.Crawford, I.L.F.Ray and D.J.H.Cockayne, Phil.Mag.A, Vol.27, 1 (1973)

80. B.K.Kad and J.A.Horton, Mater.Sci.Eng., A239-240, 118 (1997)

81. D.G.Morris, Phil.Mag.A, Vol.71, No.6, 1281 (1995)

82. I.L.F.Ray, R.C.Crawford and D.J.H.Cockayne, Phil.Mag.A, Vol.21, 1027 (1970)

83. T.Yamagata and H.Yoshida, Mater.Sci.Eng., Vol.12, 95 (1973)

84. Y.Umakoshi and M.Yamaguchi, Phil.Mag.A, Vol.41, No.4, 573 (1980)

85. M.G.Mendiratta, H.M.Kim and H.A.Lipsitt, Metall. Trans., Vol.15 A, 395 (1984)

86. Y.Umakoshi and M.Yamaguchi, Phil.Mag.A, Vol.44, 711 (1981)

87. P.Zhao, D.G.Morris, M.A.Morris, Paper submitted to J.Mater.Res.

88. C.R.Feng and K.Sadananda, Scripta Metall., Vol.24, 2107 (1990)

89. C.L.Fu and M.H.Yoo, Acta Metall.Mater., Vol.40, No.4, 703 (1992)

90. M.H.Yoo, J.A.Horton and C.T.Liu, Acta Metall., Vol.36, 2935 (1988)

91. D.G.Morris and S.Gunther, Mater.Sci.Eng., A211, 23 (1996)

92. E.P.George and I.Baker, Phil.Mag.A, Vol.77, No.3 737 (1998)

93. N.S.Stoloff and R.G.Davies, Prog.Mater.Sci., Vol.13, 1 (1996)

94. H.Saka, Phil.Mag.A, Vol.49, 327 (1984)

95. H.Saka and M.Kawase, Phil.Mag.A, Vol.49, 525 (1984)

96. H.Saka, M.Kawase, A.Nohara and T.Imura, Phil.Mag.A, Vol.51, 629 (1985)

97. H.Saka and Y.M.Zhu, Phil.Mag.A, Vol.51, 365 (1985)

98. J.T.Kim and R.Gibala, MRS Conf. Proc., Vol.213, 261 (1991)

99. D.G.Morris and S.Gunther, Intermetallics, Vol.3, 483 (1995)

100. D.G.Morris and S.Gunther, Scripta Metall., Vol.35, No.10, 1211 (1996)

101. B.G.Cullity, Elements of X-ray Diffraction, 2nd edition, Addison-Wesley Publishing Company Inc. (1978)

102. Powder Diffraction File, JCPOS, International Centre for Diffraction Data, 1601 Park Lane, Swarthmore, Pennsylvania, 19081, U.S.A. (1985)

103. P.Hirsch, A.Howie, R.Nicholson, D.W.Pashley, M.J.Whelan, Electron Microscopy of Thin Crystal, Robert E.Krieger Publishing Co., Inc. Krieger Drive, Malabar, Florida 32950, U.S.A. (1977)

104. G.E.Dieter, Mechanical Metallurgy, McGraw-Hill, Inc., U.S.A. (1985)

105. Peter Haasen, Physical Metallurgy, second edition, English translation, Cambridge University Press (1986)

106. R.W.Cahn, Materials Science and Technology, Vol. 15, Processing of Metals and Alloys, VCH *verlagsgesellschaft mbH, D.6940 Weinheim, F.R.Germany, 389 (1991)*

107. D.J.Gaydosh, S.L.Draper, R.D.Noebe and M.V.Nathal, Mater.Sci.Eng., A150, 7 (1992)

108. D.Raabe, J.Deichel, Mater.Sci.Eng., A203, 208 (1995)

109. S.A.Scheff, J.J.Stout and M.A.Crimp, Scr.Metall., Vol.32, No.7, 975 (1995)

110. M.A.Crimp and K.Vedula, Phil.Mag.A, Vol.63, No.3, 559 (1991)

111. T.Yamagata, Trans.JIM, Vol.18, 715 (1977)

112. I.Baker and J.A.Horton, Phil.Mag.A, Vol.67, 479 (1993)

113. H.Rösner, G.Molénat, M.Kolbe and E.Nembach, Mater.Sci.Eng., A192/193, 793 (1995)

114. K.Yoshimi, N.Matsumoto, S.Hanada and M.H.Yoo, Processing, Properties and Application of Iron Aluminides, eds J.H.Schneibel and M.A.Crimp, TMS, Warrendale, PA, 205 (1994)

115. M.G.Mendiratta and C.C.Law, J.Mater.Sci., Vol.22, 607 (1987)

116. I.Baker and D.J.Gaydosh, Mater.Sci.Eng., Vol.96, 147 (1987)

117. D.Hill, Introduction to dislocation, 2nd editon, Pergamon Press, 71 (1975)

118. Y.Yang and I.Baker, Intermetallics, Vol.6, 167 (1998)

119. D.G.Morris, I.C.Joye and M.Leboeuf, Phil.Mag.A, Vol.69, No.5, 961 (1994)

120. R.D.Davies and N.S.Stoloff, Phil.Mag.A, Vol.12, No.116, 297 (1965)

121. M.Victoria and A.E.Vidoz, Phys.Stat.Sol., Vol.28, 131 (1968)

122. J.Czernichow and M.J.Marcinkowski, Metall.Trans., Vol.2, 3217 (1971)

Acknowledgements

I would like to express my thanks to Prof. D.G.Morris for his enthusiasm and encouragement as the director of my thesis and for the selection of such a attractive and challenging subject that inspired me to work with great motivation. I am grateful to his constructive suggestions and advice as well as the fruitful discussions which benefit considerably from his great competency.

I would like to acknowledge Prof. M.A.Morris, the director of my TEM works, for her encouragement, suggestions and fruitful discussions during which I learnt very much from her great experience as well as for her accepting to be the member of jury.

I acknowledge Professor B.Ilschner of the "Ecole Polytechnique Fédérale de Lausanne" in Switzerland and Professor G.Sauthoff of the "Max-Planck-Institut für Eisenforschung" in Germany for kindly accepting to be members of the jury.

I am thankful to the members of " Insitut de Métallurgie Structurale" for their enthusiasm, for the favourable conditions they have created for my study, and for their direct and indirect help and contribution to my thesis.

I shall, finally, wish to thank the "Commission fédérale des Bourses pour des Etudiants Etrangers" and the " Suisse National Science Foundation" for financial support during my study period in Switzerland.